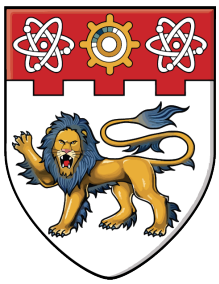

NANYANG
TECHNOLOGICAL
UNIVERSITY

DIRECT TORQUE CONTROL OF THREE-LEVEL INVERTER FED IPMSM DRIVE

DEEPU MOHAN

SCHOOL OF ELECTRICAL AND ELECTRONIC ENGINEERING

2017

DIRECT TORQUE CONTROL OF THREE-LEVEL INVERTER FED IPMSM DRIVE

DEEPU MOHAN

SCHOOL OF ELECTRICAL AND ELECTRONIC ENGINEERING

A thesis submitted to the Nanyang Technological University in partial fulfilment of the requirement for the degree of Doctor of Philosophy

2017

Acknowledgements

First and foremost, I would like to extend my sincere gratitude to my former supervisor, Asst. Prof. Gilbert Foo Hock Beng, for affording me the privilege of working with him on this research. His guidance, extensive knowledge and continuous encouragement and support have been instrumental in completing this thesis.

I am also very grateful to my current supervisor, Assoc. Prof. Chan Chok You, for his guidance, understanding, constructive suggestions and prompt support over the last two years.

I would also like to express my deepest gratitude to Dr. Zhang Xinan, whom I had the pleasure to spend a large part of my graduate life with. His untiring support and passionate involvement in every step of this study have been invaluable.

My appreciation is also extended to all technicians in the Electric Power Research Laboratory (EPRL) and the former Power Electronics and Drives Laboratory (PERL), in particular to Mrs. Lee-Loh Chin Khim and Mrs. Jennifer Ng-Tan Siew Hong, for giving me prompt technical support in my research work.

Last but not least, I would like to acknowledge my family for their sincere love and endless support. My deepest appreciation and respect goes to my late father Mohan who always encouraged me to pursue my dreams. I wish to acknowledge my mother Sathya for her boundless love and encouragement. My late brother Duke's enthusiasm and quest for life will always be an inspiration for me.

My wife Xiaona has been a priceless pillar of support throughout the last four years with her unwavering understanding, patience, and support. Tejas and Eesha, my two beautiful children, have provided me with perspective and unconditional love. Thank you for cheering *Acha* up every day with your smiles and naughtiness!

Abstract

Classical direct torque control (DTC) suffers from problems such as high torque ripples, variable inverter switching frequency and flux drooping at low speeds. Traditionally, two-level inverters are employed in direct torque controlled motor drives. The torque and flux regulation in DTC drives can be improved if three-level inverters are used instead of two-level inverters; the increase in the degree of freedom for voltage vector selection means that the rotational speed of stator flux can be more precisely controlled to attain a superior regulation of torque and flux.

At the same time, the broad review presented on the existing three-level inverter fed DTC (3L-DTC) methods at the beginning of this thesis reveal that the integration of three-level inverters into switching table based DTC drives is complicated and does not readily alleviate the shortcomings of classical DTC. Firstly, 3L-DTC drives are typically intended for use in higher power motors and therefore, the average inverter switching frequency has to be kept as low as possible to maximize the drive efficiency. However, if low switching frequencies are used, torque and flux ripples in 3L-DTC schemes can still be excessive and detrimental. Secondly, the inverter inherent switching constraints due to smooth voltage vector switching and neutral point voltage fluctuations, which are essential to reduce low order THD and ensure safe operation, must be respected.

This study focuses on the incorporation of three-level inverters into DTC drives. A number of 3L-DTC strategies incorporating a three-level neutral point clamped (3L-NPC) inverter, one of the most frequently used multilevel inverter in variable speed drives, are proposed and experimentally verified for the control of an interior permanent magnet synchronous motor (IPMSM). The torque variation rates or slopes of permanent magnet synchronous motors are considerably larger than

the minimum rate required for the proper regulation of torque during steady state. Consequently, the application of a single voltage vector within one switching period in classical DTC leads to large ripples of torque. Duty cycle based DTC (DDTC) method, in which more than one voltage vectors is applied within each switching cycle, is an effective way to reduce the torque ripples. With the DDTC method, the biggest challenge is to determine the appropriate voltage vectors and their respective duty ratios. The handful of DDTC methods in literature for 3L-DTC drives uses parameter dependent and complicated techniques for duty ratio determination. Furthermore, no consideration is given to the aforementioned inverter switching constraints in selecting the voltage vectors.

In this thesis, a comprehensive analysis is carried out to investigate the typical variation rates of torque and flux in a 3L-DTC IPMSM. Based on this analysis, a novel DDTC method using two voltage vectors, one active and one passive within one switching cycle is proposed. For duty ratio calculation, torque ripple root mean square minimization (TR-RMSM) with minimal parameter dependency is developed, taking into account the dynamics of torque and flux characteristics in an IPMSM. In addition, proper switching techniques are introduced to overcome the problem of smooth voltage vector switching and large neutral point voltage fluctuations.

Ideally for optimal torque ripple reduction, the active and passive voltage vectors applied within each switching cycle in DDTC methods should have opposing variation rates of torque. For instance, the inclusion of a zero voltage vector as a passive vector is necessary for 3L-DTC drives to optimize the torque ripple reduction during medium to low speeds. However, this is not always possible considering the smooth voltage vector switching criteria, which limits the switching transitions to be between adjacent voltage vectors. Therefore, a new DDTC method employing three voltage vectors (one active and two passive) in one switching cycle is proposed in this thesis. The application of three vectors, however, complicates the direct application of TR-RMS method for duty ratio calculations. Consequently,

a simplified duty ratio calculation technique which regulates the duty ratio of the non-zero passive vector according to the angular velocity of the motor is developed. Regulating the duty ratio of one passive vector means that aforementioned TR-RMSM method with minimal parameter dependency can be applied.

The low speed performance of 3L-DTC drives is typically affected by poor flux regulation, otherwise known as flux drooping. Flux drooping will increase the lower order harmonics in the output, and thus, affect the efficiency of the drive system. The back emf of the motor is low at low speeds and therefore, voltage vectors with smaller magnitudes are used more frequently. During heavy loads, the significant voltage drop across the stator resistance will cause the stator flux to droop. In order to alleviate the flux drooping issue during low speed, the use of virtual voltage vectors, which are synthesized from two adjacent vectors with smaller magnitudes, are proposed. The proposed method is evaluated through experiments carried out at 3% of the test IPMSMs rated speed. Results confirm that the effects of flux drooping at low speed are mitigated through the use virtual short voltage vectors.

Although the regulation of torque and flux is improved significantly by the proposed DDTC methods, they do not solve the issue of variable inverter switching frequency. The inconsistent variation of torque slope and the usage of fixed torque hysteresis bandwidth are the main causes for variable switching frequency in DTC drives. To attain a constant inverter switching frequency with improved torque and flux regulation, a simple torque regulator, consisting of a PI controller and triangular carriers, is proposed in place of the conventional torque hysteresis controller. The PI controller is used to negate the large variations in torque slope, which is desirable for reducing torque ripples. Then, the output of the PI controller is compared against triangular carriers to attain a constant switching frequency. Detailed analysis and design guidelines for the proposed torque regulator using small signal modeling are presented. In addition, the parametric robustness of the proposed method is experimentally verified.

Almost all of the existing DTC strategies used in multilevel inverter fed DTC (MLI-DTC) drives including the DDTC and constant switching frequency based methods proposed in this thesis are inverter specific. i.e., the level of hysteresis controllers and the proposed switching tables are designed specifically for inverters with a certain number of voltage levels. Therefore, these methods are not readily applicable to generic n-level multilevel inverters. In order to overcome this inconvenience, the proposed CSF strategy is extended to be generalized for inverters possessing any number of voltage levels by using a simple voltage vector decomposition technique. A comparative study with a prior art and parametric sensitivity analysis are presented to verify the effectiveness and robustness of the proposed MLI-DTC method.

Contents

List of Figures

List of Tables

List of Abbreviations

2L-DTC . . . . Two-level inverter fed direct torque control.

2LI . . . . . Two-level inverter.

3L-DTC . . . . Three-level inverter fed direct torque control.

3L-NPC . . . . Three-level neutral point clamped inverter.

AC, ac . . . . . Alternating current.

CHB . . . . . Cascaded H-bridge.

CMLI-DTC . . Classical multilevel inverter fed direct torque control.

CSVM-DTC . . Continuous space vector modulated direct torque control.

DC, dc . . . . . Direct current.

DDTC . . . . . Duty cycle based direct torque control.

DSP . . . . . digital signal processor.

DSVM-DTC . Discrete space vector modulated direct torque control.

DTC . . . . . Direct torque control.

EMF . . . . . Electromotive force.

FCC . . . . . Flying capacitor clamped.

FOC . . . . . Field orientated control.

FPGA . . . . . Field programmable gate array.

FS-PTC . . . . Finite state predictive torque control.

IPMSM . . . . Interior permanent magnet synchronous motor.

LVV . . . . . Large voltage vector of three-level inverter.

MLI . . . . . Multilevel inverter.

MLI-DTC . . . Multilevel inverter fed direct torque control.

MPC . . . . . Model predictive control.

MPC-DTC . . Model predictive control based direct torque control.

MVV . . . . . Medium voltage vector of three-level inverter.

NPC . . . . . Neutral point clamped.

PI . . . . . Proportional integral.

PMSM . . . . . Permanent magnet synchronous motor.

PWM . . . . . Pulse Width modulation.

SLT . . . . . Switching lookup table.

S3LI . . . . . Sparse three-level inverter.

SSA . . . . . Switching sequence acceleration.

SVM . . . . . Space vector modulation.

SVV . . . . . Short voltage vector of three-level inverter.

THD . . . . . Total harmonic distortion.

TR-RMSM . . Torque ripple root mean square minimization.

ZVV . . . . . Zero voltage vector.

List of Symbols

D_{act} . . . . . Duty ratio of the active vector.

$d-q$ . . . . . Rotor reference frame.

F_s . . . . . Sampling frequency.

$F_{regulator}$ . . . . . Operating frequency of the torque regulator.

i_{sd}, i_{sq} . . . . . Stator currents in the rotary $d-q$ reference frame.

i_{sx}, i_{sy} . . . . . Stator currents in the rotary $x-y$ reference frame.

$i_{s\alpha}$, $i_{s\beta}$ . . . . . Stator currents in the stationary $\alpha-\beta$ reference frame.

k . . . . . Torque slope ratio of LVV at zero speed to rated speed.

k_a, K_b . . . . . Design parameters in the proposed DDTC methods.

K_p, K_i . . . . . Proportional and Integral gains of the torque PI controller.

L_d . . . . . Direct axis inductance.

L_q . . . . . Quadrature axis inductance.

n . . . . . Number of voltage levels in a MLI.

$OS\%$ . . . . . Percentage overshoot.

P . . . . . No of pole pairs.

R_s . . . . . Stator resistance.

$\mathbf{S}_{xa}$, $\mathbf{S}_{xb}$ . . . . . Sector division in the proposed 3L-DTC; $x \subset \{1-6\}$.

s . . . . . Torque slope or variation rate.

T_e . . . . . Electromagnetic torque.

T_e^{err} . . . . . Torque error.

T_e^* . . . . . Torque reference.

T_e^0 . . . . . Initial Torque value.

T_p . . . . . Peak to peak value of triangular carriers.

T_s . . . . . Sampling interval.

v_a, v_b, v_c . . . . . Stator phase voltages.

v_{active} . . . . . Active voltage vectors.

v_{dc} . . . . . dc-link voltage.

v_{Lx} . . . . . Large voltage vectors of a 3L-NPC inverter; $x \subset \{1-6\}$.

v_{Mx} . . . . . Medium voltage vectors of a 3L-NPC inverter; $x \subset \{1-6\}$.

$v_{passive}$ . . . . . Passive voltage vectors.

v_{Sx} . . . . . Small voltage vectors of a 3L-NPC inverter; $x \subset \{1-6\}$.

v_{sd}, v_{sq} . . . . . Stator voltages in the rotary $d-q$ reference frame.

$v_{sh,x}$ . . . . . Voltage vectors in the active sub-hexagon; $x \subset \{1-6\}$.

v_{sx}, v_{sy} . . . . . Stator voltages in the rotary $x-y$ reference frame.

$v_{s\alpha}$, $v_{s\beta}$ . . . . . Stator voltages in the stationary $\alpha-\beta$ reference frame.

v_Z . . . . . Zero voltage vectors of a 3L-NPC inverter.

$x-y$ . . . . . Stator flux reference frame.

X_{ripple} . . . . . Ripple content; $X \subset \{T_e, \psi_s\}$.

$\alpha-\beta$ . . . . . Stationary reference frame.

ΔT_{err} . . . . . Torque hysteresis ± 2 band.

$\Delta\psi_{err}$ . . . . . Flux hysteresis ± 1 band.

δ . . . . . Angle between the rotor and stator flux linkage vector.

ϵ_T . . . . . Discrete output of torque hysteresis controller.

ϵ_ψ . . . . . Discrete output of flux hysteresis controller.

θ_s . . . . . Stator flux angle with reference to α-axis

ρ . . . . . Differential operator.

$|\psi_s|^{err}$ . . . . . Stator flux error.

ψ_f . . . . . Permanent magnet flux linkage.

ψ_r . . . . . Rotor flux linkage.

ψ_s . . . . . Stator flux linkage.

ψ_{rx}, ψ_{ry} . . . . . Rotor flux linkages in the rotary $x-y$ reference frame.

ψ_{sd}, ψ_{sq} . . . . . Stator flux linkages in the rotary $d-q$ reference frame.

ψ_{sx}, ψ_{sy} . . . . . Stator flux linkages in the rotary $x-y$ reference frame.

$\psi_{s\alpha}$, $\psi_{s\beta}$ . . . . . Stator flux linkages in the stationary $\alpha-\beta$ reference frame.

ω_{rated}, ω_n . . . . Rated angular velocity of the motor.

ω_{re} . . . . . Angular velocity of the motor.

$\omega_{n(act)}$ . . . . . Actual natural frequency.

ω_{nd} . . . . . Designed natural frequency.

$\widehat{\nabla} T_e$ . . . . . Peak torque slope.

ζ_{act} . . . . . Actual damping ratio.

ζ_d . . . . . Designed damping ratio.

Chapter 1

Introduction

1.1 Motor Drive

Nearly two-thirds of all electrical energy produced today is used to drive electrical motors for industrial and domestic applications. The conversion of energy, from electrical to the mechanical output of the motor, is facilitated by closed-loop drive systems that integrate the concepts of electric motors, control theory and the two basic divisions of industrial electronics, digital signal processing and power electronics [1].The basic operating structure of a modern drive system is shown in Fig. 1.1, where the controller processes and compares the low-power input references and feedback signals to regulate the flow of electrical energy to the input terminals of the motor through a power converter to attain precise control of mechanical load quantities such as speed, torque, and positioning. Such drive systems are commonly known as variable speed drives or electric servo motor drives.

1.1.1 Prime mover

Motors can be broadly classified according to the nature of electric current flow from the power converter into the motor; as direct current (DC) or alternating current (AC) motors. Previously, up to about four decades before, DC motors were the preferred choice in variable speed drives in spite of their many drawbacks such as lower efficiency, reduced reliability, higher rotor inertia and steeper cost [2], [3].

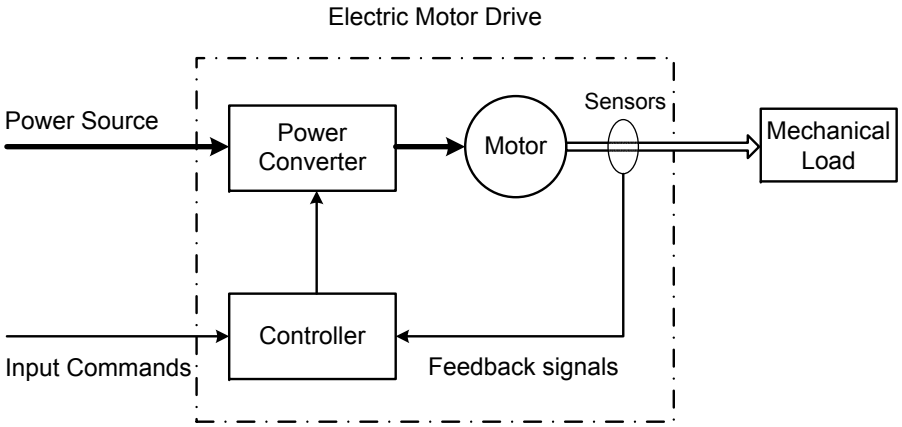

Figure 1.1: Block diagram of an electric motor drive.

For AC motors, vector control methods are necessary to ensure that the dynamic performance matches up at least equal to those of DC motors. However, vector control was complex and computationally exhaustive considering the existing industrial electronics. Therefore, the use of AC motors was limited to fixed speed applications and special application where cost was not a major factor.

The developments in industrial electronics since the beginning of 1980s have resulted in a paradigm shift towards AC motors. DC motors in high-performance variable speed drives are progressively being replaced by AC motors; examples of which include, motors for ship propulsion [4], traction drives in railways, electric vehicles, elevators and conveyors and a vast majority of industrial applications such as mining, milling and marine industry [5], [6].

The first AC motors used for variable speed applications were mainly asynchronous motors or more commonly known as induction motors. Induction motors are characterized by simple design, rugged structure and low manufacturing cost. The biggest drawback of the induction motor is that a magnetizing current from the stator is required to maintain a rotating field and hence, the motor always operates with a lagging power factor [7]. In other words, the efficiency of the induction motors is always inferior to synchronous motors.

In synchronous motors, the rotor magnetic field can be setup by an electrically

excited wound rotor or permanent magnets that are mounted on or embedded in the rotor. Compared to wound rotor design, permanent magnets guarantee a fixed rotor magnetic field with simpler design and less maintenance. Furthermore, there are no copper losses and the temperatures in the rotor are much lower. All these make permanent magnet synchronous motors (PMSM) very efficient and toque-dense [8], [9]; in fact, PMSMs operate at higher power density and higher efficiency than other AC motors. At the same time, the use of permanent magnet means that the cost of manufacturing these motors is high and very much dependent on the supply of rare-earth permanent magnets.

Nonetheless, due to the advancements and availability of modern permanent magnet materials such as NdFeB and SmCo in the recent years, the application of PMSMs for a wide variety of high-performance industrial drives systems have grown extensively [10]. Earlier PMSMs had permanent magnets mounted on the rotor surface which severely restricted the motors maximum operating speed due to the mechanical instability brought about by its architecture. To overcome this limitation, interior permanent magnet synchronous motors (IPMSM) were developed. In IPMSMs, the permanent magnets are embedded in the steel rotor core. Having permanent magnets in rotor not only make IPMSMs mechanically robust but it also alters the motors magnetic properties [11]; the effective air-gap is reduced while the saliency in the machine is increased due to the slots used for the embedment of magnets. As a result, IPMSMs produce reluctance torque in addition to the normal torque produced by the permanent magnet flux. Hence, IPMSMs are capable of delivering even larger torque-to-ampere ratio than surface mounted permanent magnet motors.

All PMSMs are capable of operating above their rated speed by adopting a technique called field or flux weakening whereby the electromagnetic flux created by stator current is used to counteract the air-gap flux generated by the permanent magnets [12]–[15]. Below the rated speed, motors are capable of operating constantly at the maximum torque (current) limit while above the rated speed torque

has to be reduced so that the motor operates with a constant power output. Since the back electromagnetic force (EMF) is proportional to the motor speed, flux weakening has to be adopted to control the output voltage to be maintained at or near the rated value for operations above rated speed. Due to the increased saliency and reduced air-gap, IPMSMs are more conducive to field weakening than surface mounted motor [14].

Today, PMSMs machines are used extensively in traction and spindle applications where the requirement are for wide range constant power and high torque and power density [10]. In particular, IPMSMs are seen as increasingly attractive choice for use in variable speed high-performance automobile, marine and railway drive system because of their ability to operate over a wide range of speed.

1.1.2 Control strategies

For high performance variable-speed PMSMs, vector control methods have to be used due to the inherent coupling effects of torque and flux to the applied voltage, current and frequency. Vector control enables PMSMs to be controlled in a similar fashion as separately excited DC motors. The two main vector controls methods are field orientated control (FOC) and direct torque control (DTC) [16].

FOC was developed in 1971 by F. Blaschke for the control of induction machine. The inner torque and flux control loop of the FOC is depicted in Fig. 1.2. A decoupled but indirect control of torque and flux respectively, is achieved through the separate regulation of q-axis (I_{sq}) and d-axis (I_{sd}) components of the stator current [11]. High performance is achieved from FOC drives with very small ripple contents in torque and flux, and a constant inverter switching frequency. Nonetheless, the implementation of FOC as seen in Fig. 1.2 is complex and computationally exhaustive. Proportional integral (PI) current controllers and multiple coordinate transformations are required. Accurate knowledge of continuous rotor position is essential for coordinate transformations and this adds to the cost of the drive [17].

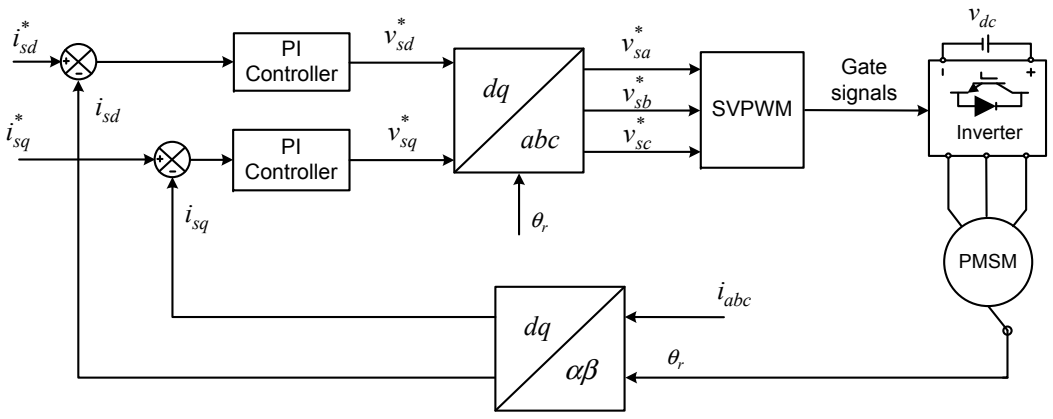

Figure 1.2: Basic structure of field orientated control.

Furthermore, space vector pulse width modulators (SVPWM) are usually required, which can be challenging if inverters with more than two voltage levels are used.

The term indirect control is generally used for FOC because it does not control torque and flux explicitly. In contrast, torque and flux are directly controlled by DTC, which was first proposed in the 1980s by Depenbrock [18] and Takahashi [19], [20]. ABB Corporation has been conducting research into DTC since 1988, and the first commercial DTC drive, ACS600 was launched in 1995. Initially designed for the control of induction motors, DTC drives have since been adopted for the control of PMSM and synchronous reluctance motors in the industry. ABB drives such as ACS800 and ACS880 are now commonly used for marine propulsion, wind turbine generators, machine tools and industrial pumps and fans [21].

The basic structure of DTC is shown in Fig. 1-3, where it can be noted that there are no current regulators, coordinate transformations and SVPWM generators involved. Torque and flux are estimated in the stationary reference frame using the knowledge of the stator resistance, initial rotor position and the stator voltages and currents. Therefore, DTC is much simpler to implement and more parametrically robust than FOC [22], [23].

Fast dynamics responses are achieved in DTC by the manipulation of stator flux vector through the use of torque and flux hysteresis controllers. Appropriate voltage vectors from a switching lookup table (SLT) are applied to stator termi-

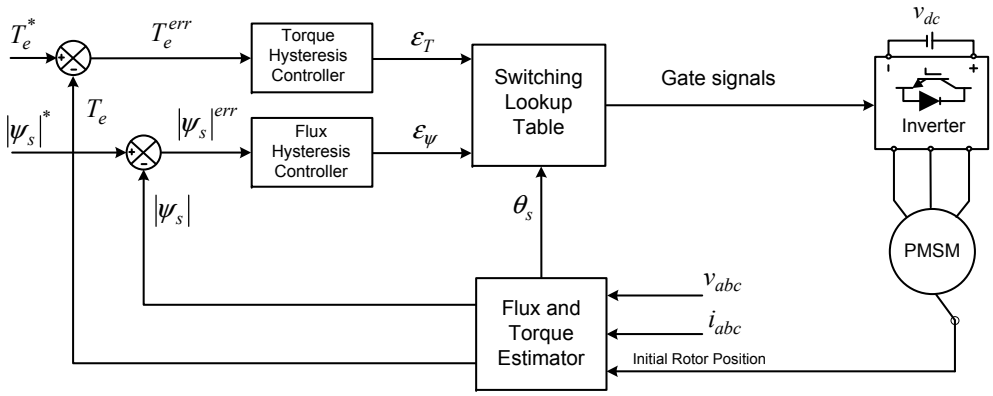

Figure 1.3: Basic structure of direct torque control.

nals based on the hysteresis controller outputs ($\epsilon_T, \epsilon_\psi$) and the estimated angular position of stator flux (θ_s) to keep the error of toque and flux to be within the predefined hysteresis bands [22].

The number of voltage vectors available in a classical DTC drive such as shown in Fig. 1.3, is determined by the type and voltage levels of the inverter used, while the instantaneous variation rate or slope of torque (Nm/s) and flux (Wb/s) corresponding to each of these voltage vectors is dependent on the operating condition of the machine and the dc-link voltage. Consequently, the use of discrete hysteresis controllers with fixed bands and the direct application of one voltage vector within each switching cycle, lead to the well-known drawbacks such as high ripples in torque and flux, drooping of flux at low speeds and variable inverter switching frequency. Alleviating these drawbacks of DTC, while maintaining its intrinsic merits, has been the subject of great research interest in recent years.

1.1.3 Power converters

Traditionally, two-level inverters (2LI) are used in DTC drives. A n-level inverter is capable of producing n^3 voltage vectors. For instance, a 2LI is capable of producing eight voltage vectors, which means that there are eight different voltages available for selection in a 2LI fed DTC drive. Now, if a multilevel inverter (MLI) is used instead of a 2LI, the number of voltage vectors is immediately increased.

The increase in degree of freedom for voltage vector selection means that the rotational speed of stator flux in a DTC drive can be more precisely controlled to achieve a superior regulation of torque and flux.

MLIs in general have received a great deal of research attention since its inception in the 1960s and are nowadays, widely employed in high to medium power AC drives [24]. Thorough review of recent developments in MLIs can be found in [24]–[30]. MLIs are capable of synthesizing output voltages at more than two levels through the use of an array of semiconductor switches, which can have lower power and voltage ratings than the nominal output power and voltage. As the number of voltage levels in the output is increased, the total harmonic distortion and dv/dt stresses in the drives systems are decreased. Besides, the switching commutations are spread over more semiconductor switches. Consequently, the average switching frequencies of the MLIs are much lower than those of the conventional two-level inverters, leading to smaller switching losses. MLIs also generate lower common-mode voltages and therefore, the bearing stresses in the motor bearing are reduced.

Among the numerous MLI topologies, structures such as the neutral point clamped (NPC) [31], flying capacitor clamped (FCC) [32] and cascaded H-bridge inverters (CHB) [33] (see Fig. 1.4), are considered as the classical or traditional topologies, and these are widely commercialized today. Many variant of the three classical topologies and other advanced topologies such as hybrid-multilevel converters and modular multilevel converters have also been developed in the recent years, and some of these have found limited industrial acceptance [24].

The in-depth analysis of multilevel inverter review presented in [24] shows that the three-level neutral point clamped (3L-NPC) and CHB are the most commonly used MLIs. FCCs have found limited industrial usage because high switching frequencies are often required to balance the voltage of the flying capacitors. For high power applications, CHB are more popular because of their modular structure and the possibility to use low-voltage semiconductor devices.

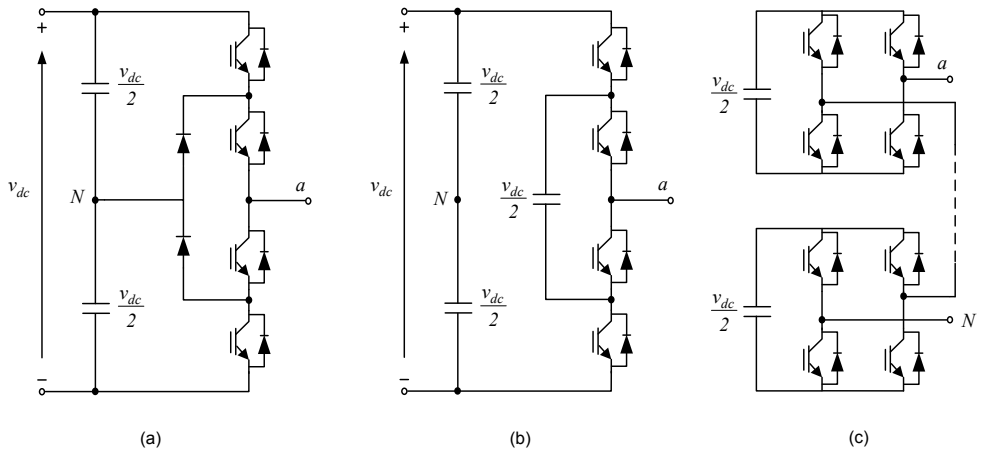

Figure 1.4: Classic multilevel inverter topologies with one phase shown. (a) Three-level neutral point clamped. (b) Three-level flying capacitor clamped. (c) Five-level cascaded H-bridge.

On the other hand, the 3L-NPC inverters are most suitable for medium power applications. NPC inverters higher than three levels are generally not used mainly because of the difficulties in maintaining the voltage balance between the dc-link capacitors, high conduction losses of the clamped diodes and the uneven distribution of losses in the semiconductor switches, which worsens as the level of the inverter is increased.

In general, the obvious drawbacks of using MLIs in motor drives are the increased circuit complexity and cost as the number of semiconductor switches and computational requirements are increased. Nevertheless, MLIs remain an attractive choice for medium to high power industrial drives, as evidenced by the increasing use of MLIs in industrial drive application in the recent years [29].

1.2 Scope of the Thesis

From the discussions in the previous section, it is clear that the integration of classical DTC and an MLI is an interesting prospect for the control of medium to high power PMSMs. In comparison to a 2L-DTC drive, MLI-DTC drives should be able to operate with fewer ripples in torque, flux and current while operating

with a much lower average inverter switching frequency. Nonetheless, there exist many hurdles, emanating from both conventional DTC and MLIs, which need to be addressed for the effective implementation of an MLI-DTC.

DTC using MLIs have not been thoroughly investigated in literature so far, as compared to the numerous advanced control strategies that have been proposed to improve the performance of 2L-DTC drives. Naturally, these advancements in 2L-DTC are not immediately applicable to MLI-DTC drives due to the increase in availability of voltage vectors and the inherent switching limitations in MLI-DTC.

In the literature, some studies have investigated the integration of MLIs into DTC drives, with majority focusing on three-level inverter fed DTC (3L-DTC) drives. Often, the intrinsic merits of classical DTC are sacrificed to improve the performance in MLI-DTC drives; for instance, complicated algorithms based on analytical solutions, co-ordinate transformations and SVM are commonly used. Thus, there exists a research gap that this thesis seeks to address, so that the capabilities of MLI-DTC drives can be maximized while retaining the advantages of conventional DTC.

This thesis focuses on the incorporation of MLIs into switching table based DTC drive for the control of an IPMSM. A three-level neutral point clamped (3L-NPC) inverter, the most commonly used MLI topology for medium voltage variable-speed AC drives [24] is used in this study.

The main objective of this thesis is to develop novel switching algorithms to improve on the performance of switching table based MLI-DTC, with major focus on 3L-DTC algorithms. Specifically, the following guidelines are established for developing MLI-DTC algorithms in this thesis:

- Attain appreciable reduction in torque, flux and current ripples while operating with low average inverter switching frequencies.
- Retain the fast dynamic response of classical DTC.

- Parametrically robust so that the performances of the proposed algorithms are not dependent on the accuracy of known machine parameter values.
- Simple structure so that the proposed algorithms can be implemented in low demand hardware.
- Lastly, all improvements listed above should be attained by adhering to the switching constraints of the MLI used for experiment, i.e., 3L-NPC inverter.

1.3 Major Contributions of the Thesis

A comprehensive analysis is first carried out to investigate the typical variation rates of torque and flux and the complexities introduced by a 3L-NPC inverter in a 3L-DTC IPMSM drive. Based on this analysis, a number of 3L-DTC algorithms are proposed to alleviate the drawbacks of classical switching table based 3L-DTC.

- A novel duty cycle based DTC (DDTC) method using two voltage vectors, one active and one passive within one switching cycle is proposed. Duty ratio calculation method using torque ripple root mean square minimization (TR-RMSM) with minimal parameter dependency is developed, taking into account the dynamics of torque and flux characteristics in an IPMSM. In addition, proper switching techniques are developed to overcome the inverter inherent problems of smooth voltage vector switching and large neutral point voltage fluctuations.
- Ideally, the active and passive voltage vectors applied within each switching cycle in DDTC methods should have opposing variation rates of torque. However, this is not always possible considering the smooth voltage vector switching criteria, which limits the switching transitions in a three-level inverter to be between adjacent voltage vectors. During medium to low speeds, the inclusion of a zero voltage vector as a passive vector is necessary to optimize the torque ripple reduction in a 3L-DTC drive. However, the direct

transition from the largest voltage vectors to a zero voltage vector is prohibited by the smooth vector switching criteria. Therefore, a new DDTC method employing three voltage vectors (one active and two passive) in one switching cycle is proposed. The application of three vectors however, complicates the direct application of TR-RMS method for duty ratio calculations. Consequently, a simplified duty ratio calculation technique which regulates the duty ratio of the non-zero passive vector according to the angular velocity of the motor is introduced. Regulating the duty ratio of one passive vector means that aforementioned TR-RMSM method with minimal parameter dependency can applied.

- The low speed performance of a DTC drives is affected by poor flux regulation, which increases the lower order harmonics in the output. At low speeds, the back e.m.f of the motor is low. Hence, voltage vectors with smaller magnitudes are used more frequently in a 3L-DTC drive. When the machine is heavily loaded, the voltage drop across the stator resistance will be significant and this will cause the stator flux to droop. A new switching strategy involving synthesized virtual small voltage vectors is proposed to mitigate the problem of flux drooping at low speeds.

- Torque and flux regulation are improved significantly by the aforementioned DDTC methods. Nonetheless, they do not solve the issue of variable inverter switching frequency. The main causes for the variable inverter frequency in DTC drives are the dependency of torque and flux slopes on the operating point of the motor and the use of hysteresis controllers with fixed bands. A novel 3L-DTC method that operates with a low and constant switching frequency is proposed. Constant inverter switching frequency is attained through the use of a simple torque regulator, consisting of a PI controller and triangular carriers, which replaces the conventional torque hysteresis controller. Detailed analysis and design guidelines for the proposed torque

regulator using small signal modelling is presented. In addition, the parametric robustness of the proposed method is experimentally verified.

- Almost all of the existing DTC strategies used in MLI-DTC drives including the proposed constant switching frequency based DTC and DDTC methods in this Thesis are inverter specific. i.e., the level of hysteresis controllers and the proposed switching tables are designed specifically for inverters with a certain number of voltage levels. To overcome this inconvenience, the proposed constant switching frequency based DTC strategy is extended to be generalized for inverters possessing any number of voltage levels by using a simple voltage vector decomposition technique. Comparative study with a prior art and parametric sensitivity analysis are presented to verify the effectiveness and robustness of the proposed MLI-DTC method.

1.4 Organization of the Thesis

This thesis is organized into seven chapters. The first chapter gives a brief introduction to motor drives, and describes the scope, contributions and the organization of the thesis.

In Chapter 2, the basic principles of DTC are explored in detail. The mathematical model of IPMSM and three-level inverters are introduced to study the variation rates of torque and flux and their dependency on the operating speed and load in a 3L-DTC drive. Then, a comprehensive review of latest advancements in DTC methods including the state-of- the-art 3L-DTC methods is presented.

The proposed DDTC strategy based on the application of two voltage vectors within each sampling cycle is presented in Chapter. 3. Detailed explanation of switching table development and duty ratio optimization for the proposed torque ripple reduction strategy is presented. Experimental results and comparative analyses are provided to verify the effectiveness of the proposed method.

Chapter 4 presents an improved DDTC strategy for 3L-DTC drives, which also improves the flux regulation during low speeds. The criteria used for voltage vector selection and the approximations used for simplifying the duty ratio calculations are explained. Procedures for practical implementation of the proposed method are highlighted. In order to analyze the efficacy of the proposed strategy, experimental results are presented and comparative studied against three existing DDTC based 3L-DTC methods.

In Chapter 5, the proposed constant inverter switching frequency based 3L-DTC algorithm is introduced. Detailed stability analysis and design criteria of the proposed torque regulator using small signal modeling are included. Experimental results investigating the parametric robustness and the steady state and transient responses are provided.

Chapter 6 presents the extension of the proposed constant inverter switching frequency based 3L-DTC method into a generalized form for application to n-level inverters. The techniques used for voltage vector decomposition and switching frequency imposition are explained in detail using a five-level MLI. The proposed MLI-DTC is verified experimentally and comparative analysis against a prior art is presented to verify the feasibility and effectiveness of the proposed algorithm

Chapter 7 concludes this thesis by highlighting the major contributions of this study. Recommendations for future research into MLI fed DTC drives are also included.

Chapter 2

Three-Level Inverter Fed DTC of IPMSM

This chapter presents a comprehensive analysis of 3L-DTC schemes for IPMSM motors. Firstly, the mathematical model of the IPMSM is introduced to study the varying nature of torque and flux characteristics in the IPMSMs. The attuning of these unique features to the principles of classical DTC and consequently, the problems commonly encountered in discretely implemented DTC are then discussed. Next, a detailed literature review of the advanced DTC algorithms that are developed to alleviate the shortcomings of classical DTC is presented. The physical model of 3L-NPC inverter is studied to clarify the extra degree of freedom in voltage vector selection that has the potential to improve the performance in DTC drives, as long as the inverter inherent complexities and switching constraints are addressed. Lastly, a thorough analysis of the latest advancements in multilevel inverter fed DTC (MLI-DTC) methods is presented, with the main focus on the state-of- the-art 3L-DTC methods.

2.1 Mathematical Model of PMSM

A generic PMSM has three-phase stator windings and permanent magnets mounted either on the surface or in the rotor. The mathematical model of a generic PMSM can be formulated from the vector quantities illustrated in the dif-

ferent coordinate axes in Fig 2.1, where the $\alpha - \beta$ axis represents the stationary reference frame. The rotating reference frames are depicted as $d - q$ and $x - y$ reference frames, with the rotor flux linkages ψ_r and stator flux linkages ψ_s synchronized respectively, to the d-axis and the x-axis. By using the rotor reference frame, the electrical dynamics of a PMSM can be described by [22]

$$\begin{cases} v_{sd} = R_s i_{sd} + \rho\psi_{sd} - \omega_{re}\psi_{sq} \\ v_{sq} = R_s i_{sq} + \rho\psi_{sq} + \omega_{re}\psi_{sd} \end{cases} \tag{2.1}$$

$$\begin{cases} \psi_{sd} = L_d i_{sd} + \psi_f \\ \psi_{sq} = L_q i_{sq} \end{cases} \tag{2.2}$$

where:

v_{sd}, v_{sq}	stator voltages in the $d - q$ reference frame
i_{sd}, i_{sq}	stator currents in the $d - q$ reference frame
ψ_{sd}, ψ_{sq}	stator flux linkages in the $d - q$ reference frame
L_d, L_q	stator inductances in the $d - q$ reference frame
R_s	stator resistance
ψ_f	permanent magnet flux linkage
ω_{re}	angular velocity of the motor
ρ	differential operator $\frac{d}{dt}$

The generated electromagnetic torque T_e in the PMSM can be derived in terms of stator flux and current as

$$T_e = \frac{3P}{2}(\psi_{sd} i_{sq} - \psi_{sq} i_{sd}) \tag{2.3}$$

where P represents the number of pole pairs in the machine. Stator flux is aligned with the x-axis ($\psi_{sx} = \psi_s, \psi_{sy} = 0$). The angular difference between the rotating stator flux and rotor flux linkage is denoted by the angle δ, which is commonly referred to as the load or torque angle. Consequently, the stator flux linkage in the

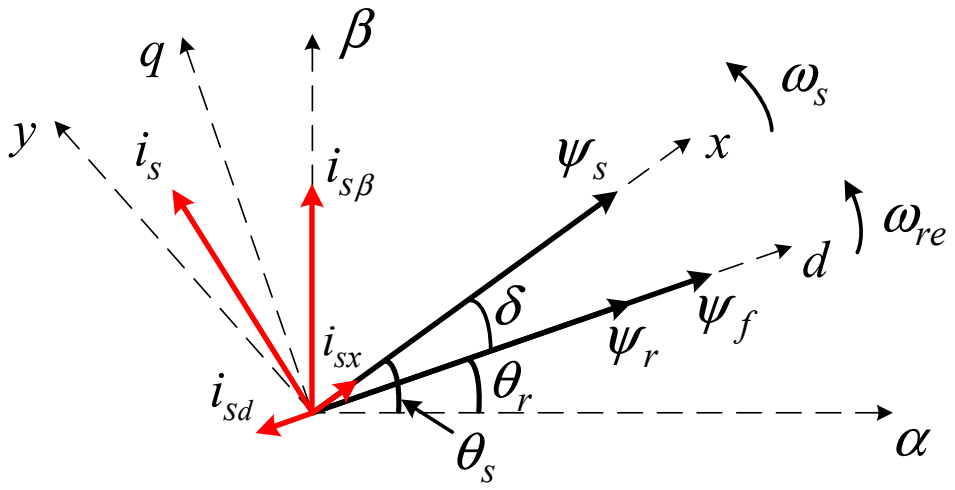

Figure 2.1: Phasor diagram of an IPMSM in stationary $(\alpha - \beta)$, rotor $(d - q)$ and stator $(x - y)$ reference frames.

$d - q$ reference can also be expressed as

$$\begin{cases} \psi_{sd} = \psi_s \cos\delta \\ \psi_{sq} = \psi_s \sin\delta \end{cases} \tag{2.4}$$

By substituting the relations in (2.2) and (2.4) into (2.3), the electromagnetic torque equation can be rewritten as [22]

$$T_e = \frac{3P}{4L_dL_q}\psi_s(2\psi_f L_q \sin\delta - (L_q - L_d)\psi_s \sin 2\delta) \tag{2.5}$$

The first term of the torque equation in (2.5) defines the excitation torque produced by the permanent magnet flux while the second term refers to the reluctance torque. In a surface mounted PMSM, the direct and quadrature axis inductances are the same. i.e., $L_d = L_q$. Therefore, no reluctance torque is generated in the surface mounted PMSM. Conversely, in IPMSM, the flux paths are asymmetrical and consequently, $L_q > L_d$. The addition of reluctance torque means that IPMSMs are inherently more power dense than the surface mounted PMSMs.

2.2 Principles of DTC PMSM

Vector control methods were briefly introduced in Section 1.1.2, where it was discussed how DTC achieves direct and decoupled control of electromagnetic torque and flux through the use of separate hysteresis controllers and the subsequent application of appropriate voltage vectors from a switching lookup table. In this section, the classical DTC technique is further examined to explicate its working principles to identify its merits as well as the shortcomings.

The detailed block diagram of the classical DTC in Fig. 2.2 shows two control loops. At this point, it needs to be pointed out that the outer speed loop uses an encoder for the rotor speed measurements in this study. It is true that by using advanced DTC methods, the angular speed of the machine can be estimated without the need for encoders [34]; i.e., DTC can be operated in a truly sensorless way. However, this study is not based on sensorless control; it specifically focuses on the performance improvement of the inner control loop.

As shown in Fig. 2.2, the inner loop of the DTC scheme is made up of three main components; namely, the stator flux and torque hysteresis controllers, the switching lookup table and an estimator that calculates the actual torque and flux generated in the motor. By referring to Fig. 2.1, the stator flux linkage ψ_s and electromagnetic torque T_e in a PMSM can be estimated in the stationary frame $(\alpha - \beta)$ as [35]

$$\begin{cases} \psi_{s\alpha} = \int (v_{s\alpha} - R_s i_{s\alpha})\ dt \\ \psi_{s\beta} = \int (v_{s\beta} - R_s i_{s\beta})\ dt \end{cases} \tag{2.6}$$

$$\begin{cases} |\psi_s| = \sqrt{\psi_{s\alpha}^2 + \psi_{s\beta}^2} \\ \theta_s = \arctan \frac{\psi_{s\beta}}{\psi_{s\alpha}} \end{cases} \tag{2.7}$$

$$T_e = \frac{3P}{2}(\psi_{sd} i_{sq} - \psi_{sq} i_{sd}) \tag{2.8}$$

where:

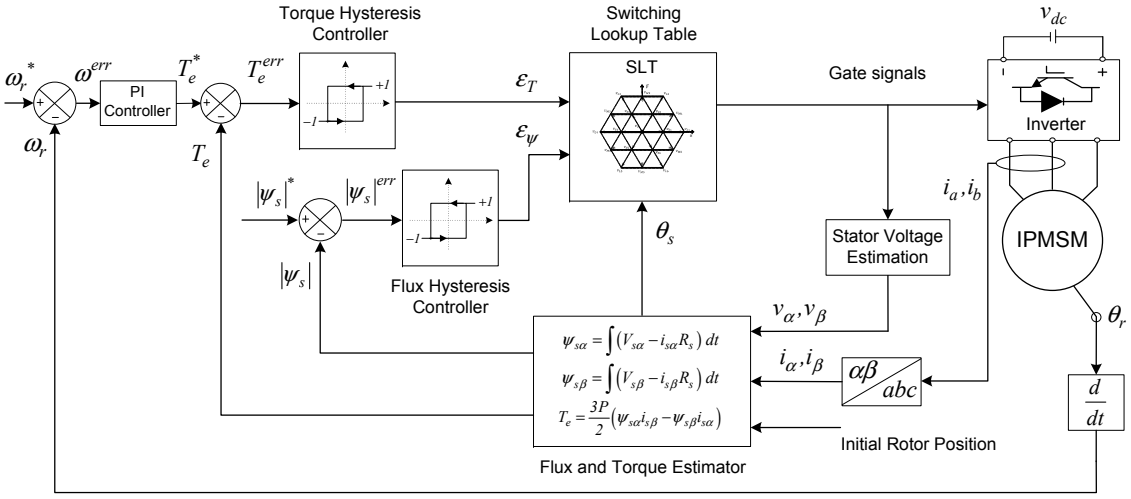

Figure 2.2: Detailed block diagram of the classical DTC drive.

$v_{s\alpha}, v_{s\alpha}$	stator voltages in the $\alpha - \beta$ reference frame
$i_{s\alpha}, i_{s\alpha}$	stator currents in the $\alpha - \beta$ reference frame
$\psi_{s\beta}, \psi_{s\beta}$	stator flux linkages in the $\alpha - \beta$ reference frame
θ_s	stator flux angle with reference to α-axis

The estimated torque and stator flux are compared to their respective reference values and subsequently, the generated torque (T_e^{err}) and flux ($|\psi_s|^{err}$) errors are quantized into digitized outputs ($\epsilon_T, \epsilon_\psi$) through the use of hysteresis controllers with fixed bands. Hysteresis bands are usually set considering the torque and flux variation rates or slopes, which are in turn dependent on the machine parameters and the dc-link voltage V_{dc} [36], [37].

From 2.6, the stator flux linkage (ψ_s) of an IPMSM can be expressed as [22]

$$\psi_s = v_s t - R_s \int i_s dt + \psi_{s,t=0} \tag{2.9}$$

where $\psi_{s,t=0}$ denotes the initial value of the stator flux vector. If the effect of stator resistance in (2.9) is assumed to be negligible (since R_s is usually small), it can be realized that the stator flux linkage will move exactly in the same direction of the voltage vector applied [38]. From (2.5), it can be recognized that the movement of stator flux vector determines the amount of torque generated in a PMSM, and this explains the fundamental principle of classical DTC.

The number of voltage vectors available for selection in a switching lookup table depends on the voltage level of the inverter used. In general, an n-level inverter will generate $3n(n-1)+1$ distinct voltage vectors. For instance, a two-level inverter will generate seven distinct voltage vectors ($v_0 - v_6$) in the $\alpha - \beta$ plane as shown Fig. 2.3. The space vector plane in Fig. 2.3 is also used here for explaining the voltage vector selection process used by the switching lookup table in classical DTC drives.

For the selection of optimal voltage vector, the knowledge of the initial value of stator flux vector in amplitude and angle is necessary, and this is estimated by (2.7). For the phase identification of stator flux vector, the $\alpha - \beta$ plane is usually divided into discrete number of regions called sectors, which also helps to ensure that the stator flux trajectory is kept almost circular. In classical two-level inverter fed DTC (2L-DTC) drives, the $\alpha - \beta$ space vector plane is divided typically into six sectors (S_1−S_6) of 60°, as illustrated in Fig. 2.3. With the identification of sector number, the optimal voltage vector can be selected based on the digitized outputs of the torque and flux hysteresis controllers. For instance, if the stator flux vector is in sector $S_1(-30° < \theta_s < 30°)$ at $t = 0$ as shown in Fig. 2.3, the effects of applying four non-zero voltage vectors, v_2, v_3, v_5 and v_6, for a switching period T_s, are illustrated in Fig. 2.3 as $\psi_{s,v_{x\epsilon(2,3,5,6)}}$.

From Fig. 2.3, it can be observed that the application of v_2 or v_3 would make the stator flux vector rotate in the anti-clockwise direction, i.e., a positive increment in torque angle, $+\Delta\delta$. Therefore, either voltage vector v_2 or v_3 has to be used for an increase in torque. Then, the choice of selection between vectors v_2 and v_3 would depend on the stator flux demand; v_2 would provide an increase in the magnitude of ψ_s while v_3 would have the opposite effect.

With regards to the voltage vector selection process in sector S_1, it is also important to discuss the non-usage of other voltage vectors, namely, v_0, v_1 and v_4. Vectors v_2, v_3, v_5 and v_6 are used typically in sector S_1 because they always produce

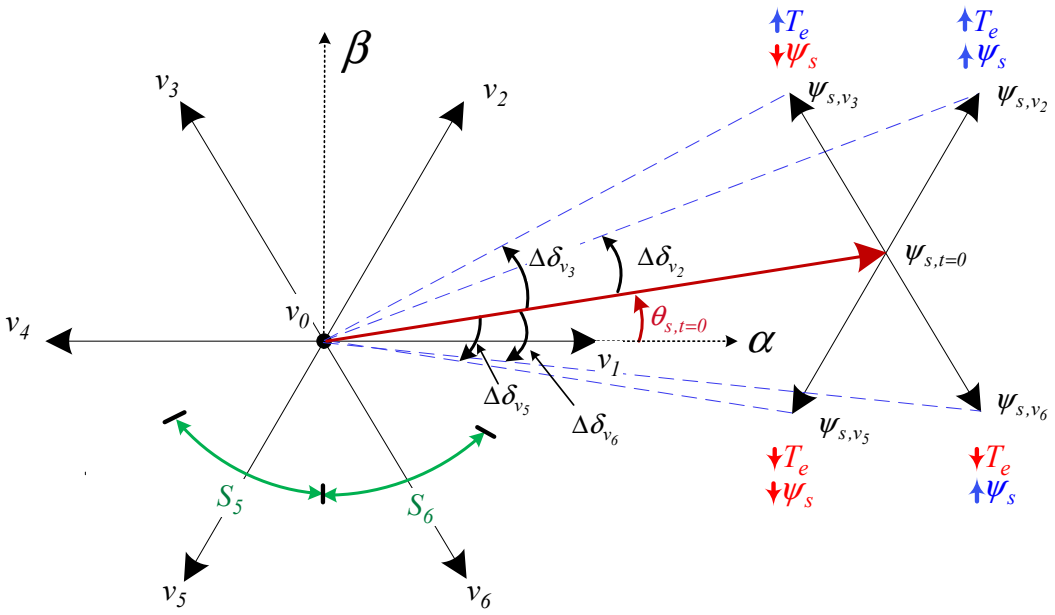

Figure 2.3: Voltage vector selection principle of a classical DTC drive.

higher rate of change in the load angle ($\frac{\Delta\delta}{\Delta t}$) and therefore, more electromagnetic torque than the vectors v_0, v_1 and v_3.

Nonetheless, the zero vector v_0 is used commonly in the DTC of induction motors. The torque hysteresis controller used in DTC induction motor drive typically has three output levels ($\epsilon_T = \pm 1, 0$) as shown in Fig. 2.4(a), with $+1$ and -1, respectively, indicating that an increase and a decrease in torque is needed. The state 0 indicates that the calculated torque error is within the hysteresis bands and no sudden change of torque angle is needed. Consequently, when $\epsilon_T = 0$, a zero vector is applied in the DTC of induction motors, which ensures that the stator flux vector stays at its initial position (2.9). In contrast, when a zero vector is applied in a PMSM drive, the stator flux will not stay at its initial position. This is due to the flux provided by the permanent magnet in the rotor. Therefore, the hysteresis controller output level $\epsilon_T = 0$ and zero voltage vectors are not commonly used in DTC of PMSMs [39]. For flux regulation, the two-level hysteresis controller shown in Fig. 2.4(c) is generally used for DTC of all motor types.

Based on the discussion above, it can be summarized that radial component

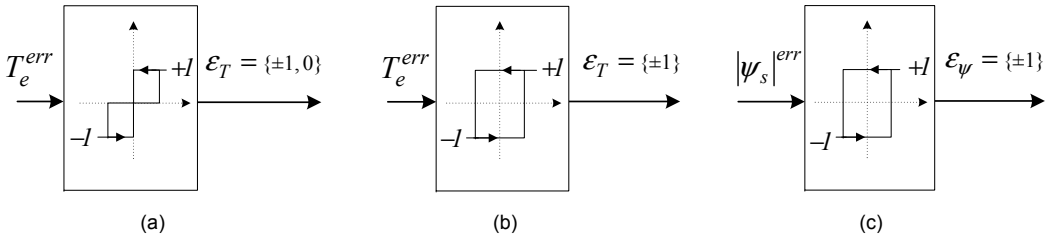

Figure 2.4: Implementation of hysteresis controllers used typically in DTC. (a) Torque control in induction motor drives. (b) Torque control in PMSM drives. (c) Flux control.

of the applied voltage vector will alter the amplitude of stator flux linkage. Conversely, the tangential component will influence the load angle, which will in turn influence the electromagnetic torque produced by the PMSM. The direct and rapid application of appropriate voltage vector in a sampling cycle leads to excellent torque and flux dynamics in DTC drives. At the same time, large ripple content in torque and flux are produced, and the inverter switching frequency is variable due to the nonlinear behavior of the motors. The torque and flux ripples generated in DTC drives are determined by the respective variation rates or slopes, the sampling frequency and the width of the hysteresis bands used.

2.3 Torque and Flux Variation Rates

To understand the aforementioned shortcomings of classical DTC, the torque and flux variation rates of the PMSM has to be studied. By referring to the phasor diagram in Fig. 2.1, the permanent magnet flux linkage ψ_f is aligned with the d-axis, whereas the stator flux ψ_s is aligned with the x-axis($\psi_{sx} = \psi_s$). Therefore, the x-axis (v_{sx}) and y-axis (v_{sy}) components of the stator voltage and the electromagnetic torque T_e can be expressed as [35]

$$\begin{cases} v_{sx} = R_s i_{sx} + \rho|\psi_s| \\ v_{sy} = R_s i_{sy} + \omega_s|\psi_s| \end{cases} \tag{2.10}$$

$$T_e = \frac{3P}{2}|\psi_s|i_{sy} \tag{2.11}$$

where, ω_s represents the angular velocity of the stator flux; i_{sx} and i_{sy} are the stator currents in $x-y$ frame. The active rotor flux ψ_r in an IPMSM is dependent on the d-axis component of the stator current i_{sd} and the direct (L_d) and quadrature (L_q) axis inductances (2.12). By differentiating both sides of (2.11), the torque variation rate with respect to time can be found as shown in (2.13).

$$\psi_r = \psi_f + (L_d - L_q)i_{sd} \tag{2.12}$$

$$\rho T_e = \frac{3P}{2}\Big(i_{sy}\rho|\psi_s| + |\psi_s|\rho i_{sy}\Big) \tag{2.13}$$

The x-axis and y-axis components of the stator flux can be expressed as

$$\begin{cases} \psi_{sx} = L_q i_{sx} + \psi_{rx} \\ \psi_{sy} = L_q i_{sy} + \psi_{ry} \end{cases} \tag{2.14}$$

where ψ_{rx} and ψ_{ry} are the x-axis and y-axis components of the rotor flux. Since the y-component of the stator flux is zero ($\psi_{sy} = 0$), the following relations for the rate of change of stator flux (2.15) and x-axis component of the stator current (2.16) can be established as

$$\rho|\psi_s| = \rho|\psi_{sx}| = v_{sx} - R_s i_{sx} \tag{2.15}$$

$$\rho i_{sy} = \frac{\psi_{rx}}{L_q}\rho\delta \tag{2.16}$$

where δ represents the angular difference between rotor and stator flux vectors. Substituting the relations in (2.10) to (2.11) and (2.15) to (2.16) into (2.13) yields

$$\begin{aligned} \rho T_e &= \frac{3P}{2L_q}\Big[- v_{sx}\psi_{ry} - R_s i_{sy}(\psi_s - \psi_{rx}) + |\psi_s|\psi_{rx}\rho\delta\Big] \\ &= \frac{R_s}{L_q}T_e + \frac{3P}{2L_q}\Big[- v_{sx}\psi_{ry} + \psi_{rx}(v_{sy} - \omega_s|\psi_s|) + |\psi_s|\psi_{rx}\rho\delta\Big] \end{aligned} \tag{2.17}$$

Rearranging the terms in (2.17) and since the rotor speed ω_{re} is the difference between stator speed ω_s and the derivative of δ with respect to time, the torque variation rate of a PMSM can be expressed as

$$\rho T_e = -\frac{R_s}{L_q} T_e - \frac{3P}{2L_q} |\psi_s| \psi_{rx} \omega_{re} + \frac{3P}{2L_q} v_s \otimes \psi_r \tag{2.18}$$

where $v_s \otimes \psi_r$ denotes the cross multiplication of stator voltage and the active flux.

Equation (2.18) validates that the torque can be regulated by the voltage vector applied to the stator terminals. At the same time, it is evident that the torque variation rate of the PMSM would vary according to the operation point of the machine as the instantaneous torque and the rotor speed influence the torque variation rate in a counteracting manner. This also means that the average decreasing torque variation is always larger than the increasing torque variation in PMSM. In order to have a numerical appreciation of the extent of torque variation rate in a PMSM motor, the peak variation rate of the IPMSM used in this study can found easily by substituting in the motor parameters tabulated in Appendix. A. Assuming a dc-link voltage of 150V and maximum torque per ampere (MTPA) [23] conditions, the peak variation rate of torque is approximately $6250 Nm/s$ for the IPMSM used in study.

The stator flux is aligned with the x-axis ($\psi_{sx} = \psi_s$). From (2-15), it follows that the variation rate of stator flux depends only on the stator resistance, and the x-components of stator voltage and current. By neglecting the voltage drop across the stator resistance in (2-15), it is seen that the variation in stator flux is approximately proportional to the x-component of stator voltage. This implies that the amplitude of the flux variation rate is much smaller compared to that of torque.

The above discussion on the characteristics of torque and stator flux variation rates helps to explain the shortcoming of DTC for PMSM drives; the large ripple content, especially of torque, and the variable inverter switching frequency. Inconsistent inverter switching frequency is mainly caused by the use of hysteresis

controllers with fixed bands to control the torque and flux, both of which vary nonlinearly in the motor. When compared to torque, the regulation of flux has negligible influence on the switching frequency variations as the flux variation rates are: 1) much smaller than that of torque; 2) not heavily influenced by the operating conditions of the motor (2.15) [36]. On the contrary, the inverter switching frequency is heavily influenced by the torque variation rate. For instance, the inverter switching frequency in a classical DTC drive is usually at its highest during low speed operations, as demonstrated by the experimental results in [40]. This is not unexpected as the torque variation rate would be highest during low speed operations (2.18).

In classical DTC, the large torque slopes of the PMSM drives are often far greater than the minimum rate required to regulate the torque effectively during steady state [7], [8]. For instance, the 5 Nm rated IPMSM used in the study has an approximate peak torque variation rate of 6250 Nm/s; at a sampling frequency of 5 kHz, the peak variation in torque would be about 25% of the rated torque. Consequently, the application of a single voltage vector in an entire sampling period results in significant ripples of torque.

Torque ripples can be reduced by using high sampling frequencies (40 kHz). However, this will reduce the drive efficiency as inverter switching losses are increased. Furthermore, the cost of the drive system will increase as a powerful DSP or an FPGA will be required to satisfy the increased computational burden.

The torque ripples can also be reduced by using small bands for torque hysteresis controller. However, this will also lead to increased inverter switching frequency [36], [37]. At the same time, it has to be noted that the torque ripple reduction attained due to the decrement in torque hysteresis bands, will only be effective up to a certain minimal band width. Below this minimal value, which is governed by the torque variation rate of a motor, the impact of hysteresis band on the torque ripples becomes negligible, but the switching frequency will keep increasing [36]. Therefore, it can rationalized that the torque hysteresis bands

should be set as low as possible so that an acceptable torque ripple minimization is possible considering the torque variation of the machine and also the desired switching frequency. In other words, it should not be set lower than a minimum point whereby the band will have no impact on the torque ripples produced.

It is well established in the literature that the total harmonic distortion (THD) in the stator current is heavily influenced by the ripples in the stator flux [36], [37]. Of course, THD deterioration can also be caused by poor torque regulation, but this aspect is usually small compared to flux regulation. Hence, it is important to regulate the flux as tightly as possible to its reference. Flux is commonly regulated in DTC drives using small flux hysteresis controller bands. Since the slope of flux is small and its impact on switching frequency variation is negligible, as previously explained, flux can be the regulated more efficiently than torque in classical DTC drives [36].

At the same time, it should be highlighted that the low speed performance of DTC drives is typically affected by poor flux regulation, also known as flux drooping [41]. Flux drooping will increase the lower order harmonics in the output, and thus, affect the efficiency of the drive system. The effects of flux drooping are usually noticeable at sector transitions, especially when the motor is heavily loaded; the significant voltage drop across the stator resistance will cause the stator flux to droop. In classical DTC, a fixed number of sectors are used to identify the stator flux location. Therefore, torque and flux are not evenly applied in a sector. Usually, the voltage vector with the highest potential to change the desired torque dynamics is selected to attain fast dynamic torque response. As a result, flux regulation quality is occasionally compromised. It follows from (2.15) that flux drooping in an IPMSM drive occurs when

$$|v_{sx}| < |R_s i_{sx}| \tag{2.19}$$

An example of the flux drooping problem is illustrated in Fig. 2.5(a) when the stator flux vector $\psi_{s,t}$ has just crossed over into the sector S_k. The voltage vector

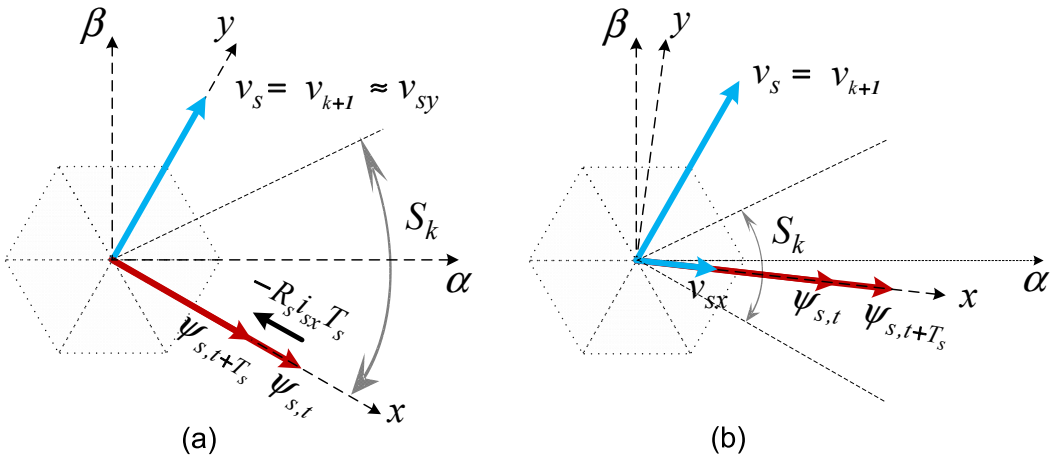

Figure 2.5: Stator flux regulation in the IPMSM drive. (a) Flux drooping near sector boundary. (b) Normal operation.

v_{k+1} is typically used in conventional DTC drives for an increment in both torque and flux (see Fig. 2.3). From Fig. 2.5(a), it can be noted that the x-axis component of the stator voltage v_{sx} is small at this point ($v_{sx} = 0$, at the sector boundary). Consequently, the application of v_{k+1} will cause the stator flux to droop as shown in Fig. 2.5(a); i.e., $\psi_{s,t+T_s} < \psi_{s,t}$. In contrast, when the same voltage vectors are applied in the region away from the sector boundary, as shown in Fig. 2.5(b), the stator flux will increase. The effects of flux drooping are clearly detectable during low speeds operations as the stator flux vector spends more time in the sector transitioning regions, i.e., the condition in (2.19) will hold true for a longer period, especially when the machine is heavily loaded (as $R_s i_{sx}$ will increase).

Another important aspect that deteriorates the regulation of torque and flux is the effects of one cycle delay which is caused by discrete implementation of DTC algorithms. In other words, a finite time is needed during each sampling cycle $T_{s,k}$ to process the feedback signals to determine the voltage vector v_s to be applied to the stator terminals. The selected voltage vector will only be applied at the start of next sampling period $T_{s,k+1}$, meaning that there is a delay of one sampling period before the flux or torque excursions from the hysteresis bands can be addressed [42].

In digitally implemented classical DTC drives, one cycle delay is inevitable, and plays an important role in determining the regulation of torque and flux. In brief, the main effects of one cycle delay are: 1) the actual torque and flux in the machine will excurse far beyond the set hysteresis bands and this means that the torque and flux errors will be larger than the hysteresis bands; 2) as torque and flux ripples are much larger than the fixed bands, it will take more sampling cycle to correct the respective errors. Therefore, the average switching frequency of the inverter will decrease as explained in [40].

In order to alleviate the effects of one cycle delay in classical DTC drives, high sampling frequencies can be used to reduce the delay between feedback measurements and the actual correction. Nevertheless, the usage of short sampling time leads to increased inverter switching frequency and therefore, switching losses.

2.4 Advanced DTC Methods

Numerous advanced algorithms have been proposed in the literature to address the aforementioned shortcomings of the classical DTC. In this section, these advanced methods are reviewed, covering developments in DTC strategies applicable not only for PMSMs but for all generic AC motors.

In classical DTC drives, the number of voltage vectors available for selection from a switching lookup table is limited, with fixed magnitude and direction. For instance, there are seven distinct voltage vectors available for selection in a classical 2L-DTC drive, as illustrated in Fig 2.3. By increasing the number of voltage vectors available for selection, the speed of stator flux vector in DTC drives can be better controlled to attain an improved regulation of torque and flux. Therefore, it is not surprising that the adoption of space vector modulation (SVM) into DTC drives has been on the rise in the recent years. Two types of SVM are used commonly used with DTC drives; continuous SVM (CSVM-DTC) and discrete SVM (DSVM-DTC).

With CSVM-DTC, an arbitrary voltage vector with adjustable amplitude and phase can be generated within the linear range of the inverter by applying two adjacent non-zero voltage vectors and if necessary, a zero voltage vector, sequentially during a switching period [43]. For instance, an arbitrary voltage vector within the triangular space enclosed by the voltage vectors v_1, v_2 and v_3 in Fig. 2.3 can be produced by regulating the duration that each of these three vectors are applied during a switching period.

The major difference in existing CSVM-DTC strategies is the method used for determining the appropriate reference voltage vector. Methods for determining the reference voltage vector include direct torque and flux control (DTFC) using synchronous rotating frame-oriented control [44]–[47], sliding mode control [48], [49], indirect torque control [50] and dead-beat control [51]–[53].

With the ability to produce an arbitrary voltage vector within the linear range of the inverter during each switching period, stator flux vector can be more accurately controlled and the ripple in torque and flux are reduced. Furthermore, a fixed inverter switching frequency can be attained as a three voltage vectors are always applied during each switching period. As torque and flux regulation are improved, the sampling frequency used in CSVM-DTC can be much lower than that of classical DTC.

The advantages of CSVM-DTC are clearly demonstrated in [50], where the performance of the proposed SVM-based 2L-DTC algorithm is compared to classical 2L-DTC method for an IPMSM drive. Even though it's sampling frequency is set to half the sampling frequency of classical 2L-DTC, the constant switching frequency based CSVM-DTC method attains approximately 58% and 92% reductions in torque and flux ripples respectively, as the fully loaded IPMSM is operating at 75% of the rated speed.

Although CSVM-DTC significantly improves torque and flux regulation while operating with a constant switching frequency, the simplicity and robustness of classical DTC are often compromised. Most of the CSVM-DTC strategies require

some sort of coordinate transformations [44]–[49], which increases the computational burden, while the effectiveness of some methods are dependent on the stability of the PI controllers used [44]–[47], [50], and the accurate knowledge of the motor parameters [51]–[53].

Additionally, as multiple voltage vectors are sequentially applied in one sampling period, the switching frequency and the complexity are increased with SVM. For instance, the switching frequency of the proposed CSVM-DTC in [50] is 6.66 kHz while the classical 2L-DTC, under the same conditions, operates with a variable switching frequency ranging from 1.5 kHz to 2.4 kHz.

The switching complexities in CSVM-DTC drives will significantly increase if inverters with higher than two levels, i.e., multilevel inverters (MLIs), are used. It is true that the state-of-the-art DSPs are equipped with PWM modules that can easily generate SVM pulses for two level inverters. However, if MLIs are to be used in DTC drives then implementing CSVM-DTC can easily become complicated.

Another effective way to increase the number of voltage vector available for selection in DTC drives is through DSVM-DTC [54], [55] where new voltage vectors are synthesized by applying multiple voltage vectors in one sampling period for predefined time intervals. In [54], it is shown that, with a division of three intervals in one switching cycle, the number of voltage vectors corresponding to a two-level inverter can be increased from seven to thirty seven. With the increase in voltage vectors, the degree of freedom in sector division is also increased. In addition, torque hysteresis controllers with multiple discrete levels are used to meet the torque demand during different operating speed. Torque ripples are reduced but at the cost of increased switching losses and complexity, as multiple switching tables are used.

In the past decade, model predictive control (MPC) based algorithms are being used increasingly in DTC drives. The fundamentals of MPC and its practicality in motor drives are thoroughly studied in [56]–[59]. The basic principle of the model predictive DTC (MPC-DTC) is to predict the future states of the machine, known

as the predictive horizon N, in discrete time using a system model to determine the optimal voltage vector/s to be applied in each sampling period.

A wide variety of MPC-DTC algorithms exists in literature, differing in the predictive horizon, the optimization techniques and the number of voltage vector used. For instance, one step MP-DTC algorithms are presented in [60], [61], while the MP-DTC algorithm developed in [62] uses a two-step prediction. In some other instances, several future switching transitions ($N > 1$) are predicted as exemplified in [63], [64] to determine the optimal switching sequence to keep the torque and flux within their respective hysteresis bands. By using a prediction model that has two or more step prediction, the effects of one cycle delay due to digital implementation can be negated [65].

The increase in longer prediction horizon also improves the performance and stability of the drive system; nevertheless, at the cost of significant increase in computational requirements [58]. MPC-DTC algorithms applying more than one voltage vectors in one sampling cycle are also common; the proposed methods in [66], [67] use two voltage vectors while up to three voltage vectors, two active and one zero vector, are used in [68], [69] to minimize the ripples in torque and flux. The duty cycles of the voltage vectors are calculated using various optimization methods. Nonetheless, all of these MPC-DTC methods use machine models and pulse width modulation (PWM) or SVM techniques are often required to implement the switching sequence.

Finite state predictive torque control (FS-PTC) is a recent variation of MPC-DTC that reduces the computational load and complexity of MPC-DTC by taking advantage of the discrete nature of power converters [70]. As the name implies, only the finite switching states of the inverter are considered for solving the optimization problem. The switching state that minimizes a predefined cost function is selected and the control action is directly applied to the inverter in the next switching cycle. By avoiding the use of a switching modulator, the optimization problem is simplified and it is relatively simpler to add targets, variables and constraints to

the cost function [71]. Used in 2L-DTC drives, the FS-PTC is relatively simple and the computational load can be inexpensive if the horizon length is set to $N = 1$ and the control objectives in the cost function are set to a minimum [56].

Conversely, if multilevel inverters are to be used in FS-PTC based DTC, the computational load would still be high due to the increased number of switching states. A solution to this problem is suggested in [72] by using a modified lookup table that takes into account the torque error. Another important drawback of FS-DTC is the selection of weighting factors used for the cost of different targets in the final cost function [73]. Often, these factors are determined by solving machine parameter dependent equations [74]. In some other instances, time consuming trial and error methods using computer simulations are used [75].

It is true that the MPC-DTC contributes to significant improvements in torque and flux regulation in DTC drives. Nevertheless, MPC-DTC is inherently machine parameter dependent, and high complexity and computational requirements are a prerequisite, especially if multilevel inverters are to be incorporated into DTC drives.

Another popular approach to improving the torque and flux regulation in DTC drives is to use a duty cycle control method with the conventional DTC (DDTC). The ripples in torque and flux are reduced in DDTC algorithms by the application of two [42], [51], [76]–[81] or more [40], [82] voltage vector during each sampling period. The non-zero vectors used in DDTC are usually called active vectors. DDTC can be considered as an extension of classical DTC since it usually does not need the modification of classical switching lookup table. Instead, the voltage vector length is manipulated according to the torque error and therefore, only the calculation of duty ratios of the active voltage vector/s is/are required. In the literature, the analytical approaches used for determining the duty ratios include deadbeat control [51], fuzzy-logic adaptation [76], direct mean torque control [42], [77] and torque ripple root mean square minimization (TR-RMSM) [78], all of

which are complicated and reliant on the machine model to solve for duty ratios. Improvements to the TR-RMSM approach in [78], [81] are reported in [79] and [80].

The effectiveness of the state-of-the-art DDTC methods in [78]–[80], for improving the performance of 2L-DTC drives, can be appreciated by examining the comparative analysis that was carried out in [80]. Table. 2.1 summarizes the responses of the experimental IPMSM drive in [80], operating at the rated speed and load, as different DTC algorithms are applied using the same sampling frequency of 10 kHz.

In general, the efficacy of the DDTC methods in reducing ripples in torque and flux is clear. At the same time, it can be noticed that the torque ripple reduction capability of the TR-RMSM approach in [78] is slightly inferior to other DDTC methods. This is because the duty cycle determination in [78] is machine parameter dependent and therefore, suffers significantly from the effects of one cycle delay [79], [80]. Conversely, the simple duty determination method proposed in [79], uses two constant gains, attained through trial and error method, to minimize the parameter dependence of the TR-RMSM method. Torque and flux ripples are reduced appreciably. However, due to the use of constant gains when coupled with the varying nature of torque slope in the motor (2-18), results in significant steady state torque errors [80]. To overcome this problem, the DDTC method proposed in [80] takes both the torque error and operating speed into consideration for calculating the duty ratio. Experimental results presented prove the effectiveness of this method in reducing the ripples in torque and flux while maintaining acceptable steady state torque error for all operating speed ranges.

Some DDTC methods use two active and one zero voltage vector in one switching cycle to improve both torque and flux ripples, for instance in [40], [82]. However, the slight improvements noted in the flux regulation are attained at the cost of increased complexity and increased inverter switching frequency, i.e., higher switching losses. Furthermore, the proposed method in [40] is an extension of [79] which produces large steady state torque errors. On the other hand, the approach

Table 2.1: Steady State Comparison of Different DDTC Algorithms in [80]

400 rpm, 5 Nm	Classical 2L-DTC	DDTC [78]	DDTC [79]	DDTC [80]
Torque ripple (Nm)	0.3504	0.2362	0.1376	0.1851
Flux ripple (mWb)	0.01978	0.01773	0.01621	0.01715
Stator current THD (%)	4.44	3.93	4.09	4.11
Steady state torque error (%)*	7.98	4.3654	40.0712	3.5538
Steady state flux error (%)*	0.127	0.2254	0.1614	-0.0307
Ave switching freq. (kHz)	1.898	3.647	5.431	3.252

Rated speed = 400 rpm, Rated torque = 5 Nm. * Steady state errors expressed as % of rated values

in [82] uses parameter dependent analytical TR-RMSM approach to balance the ripple reduction in torque and flux.

In order to improve the performance of classical DTC, all the previously mentioned advancements in this section have tried to increase the number of voltage vector available in each sampling period through digital synthesization. Clearly, another way to increase the number of voltage vectors is to integrate multilevel inverters (MLIs) into classical DTC drives. Traditionally, two-level inverters are employed in direct torque controlled motor drives. In recent years, however, multilevel inverters have become increasingly popular in (DTC) drives as the power levels of the industrial drives have increased [24], [55], [83].

In MLI fed DTC (MLI-DTC) drives, the overall drive performance is improved with better torque and flux control, but at the same time, the cost and complexities are increased. Besides, MLI-DTCs are typically intended for use in medium to high power drives, as explained previously. Therefore, they should be operated with much lower switching frequencies than the 2L-DTC drives. If low sampling frequencies are adopted to minimize the switching losses, the variation of torque and flux according to (2.18) and (2.15), respectively, would still be substantial. Therefore, high torque and flux ripples will be produced.

As discussed previously in this section, many advanced control strategies have been proposed in the literature to improve the performance of classical DTC drives. However, most of these approaches focus on two-level inverter fed DTC (2L-DTC) drives and therefore, are not readily applicable to 3L-DTC drives due to two important aspects.

Firstly, with the increase in voltage vectors, the control approach in MLI-DTCs has to be extended to fully exploit the additional degree of freedom (voltage vectors, sector division, etc.) provided by the inverter [24], [55]. For example, the switching table can be expanded to include more sector division and the discrete levels of the hysteresis controller can be increased so that the rotating stator flux vector can be better controlled. Secondly, there are inherent switching constraints and other requirements such as the neutral point capacitor voltage balancing that needs to be considered in MLI-DTCs.

2.5 Three-level Neutral Point Clamped (3L-NPC) Inverter

This thesis focuses on the DTC of 3L-NPC inverter fed IPMSM. In this section, the physical model of the 3L-NPC inverter is studied to understand the working principles and recognize the possible difficulties and constraints when incorporated into DTC drives.

The equivalent representation of a 3L-NPC inverter with half the dc-link voltage on each of the capacitors is shown in Fig. 2.6. In general, an n-level inverter will generate $3n(n-1)+1$ distinct voltage vectors while the total number of switching states will be n^3. The twenty-seven switching states generate the output voltage vectors in the stationary $\alpha-\beta$ plane as shown in Fig. 2.7 by [84]

$$\overrightarrow{v_s} = \frac{2}{3}\left(v_a N + A v_b N + A^2 v_c N\right) \tag{2.20}$$

where $A = e^{j\frac{2\pi}{3}}$. The states 1, 0 and -1 in Figs. 2.6 and 2.7 represent the switching state of each phase, that denotes a connection to the inverters positive

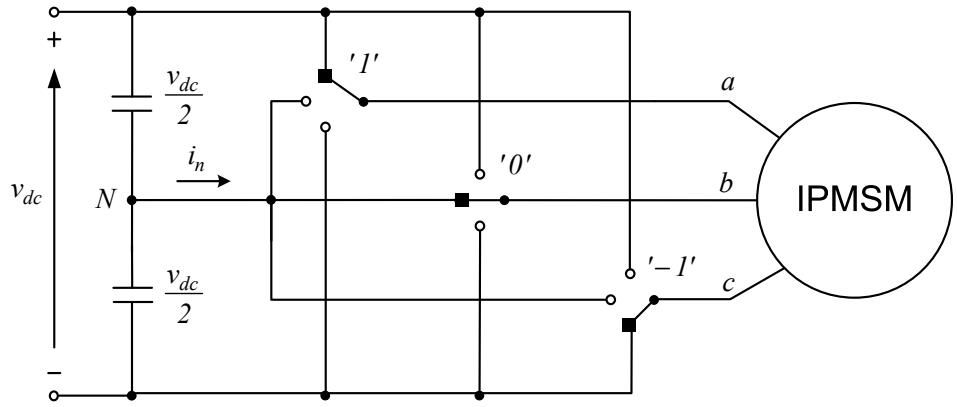

Figure 2.6: Equivalent circuit representation of the 3L-NPC inverter showing the switching state, v_{M1} $(10-1)$.

dc rail $(+0.5V_{dc})$, neutral point $(0V)$ and negative dc rail $(-0.5V_{dc})$, respectively.

The voltage vectors can be categorized into large (LVV, $v_{L,1-6}$), medium (MVV, $v_{M,1-6}$), small (SVV, $v_{S,1-6}$) and zero (ZVV, v_Z) voltage vectors. Both SVVs and ZVVs have redundant switching states. The redundant switching states of SVVs generate the same AC side voltages but produce neutral point current i_n with opposite polarities. The three ZVVs represent the switching states whereby all the three phases of the motor are connected to the same dc terminals.

One of the inherent drawbacks of the 3L-NPC inverter is the neutral point voltage balancing issue. Neutral point voltage balancing is essential to ensure a constant voltage stress on the dc-link capacitors and the semiconductor switches. Moreover, an unbalanced dc-link will increase the lower order harmonics in the outputs [85]. The imbalance in dc-link capacitor voltages occurs due to the uneven charging and discharging of the capacitors whenever either MVVs or SVVs are used, i.e., the use of MVVs or ZVVs will cause the flow of i_n as these switching states have switch positions connected to the neutral point.

Ideally, the average neutral point current should zero in a switching cycle to keep the voltage oscillations minimal at the neutral point. This, however, is clearly not plausible for a switching table based conventional 3L-DTC drive, where a single voltage vector is applied for the entire switching period. The issue of voltage

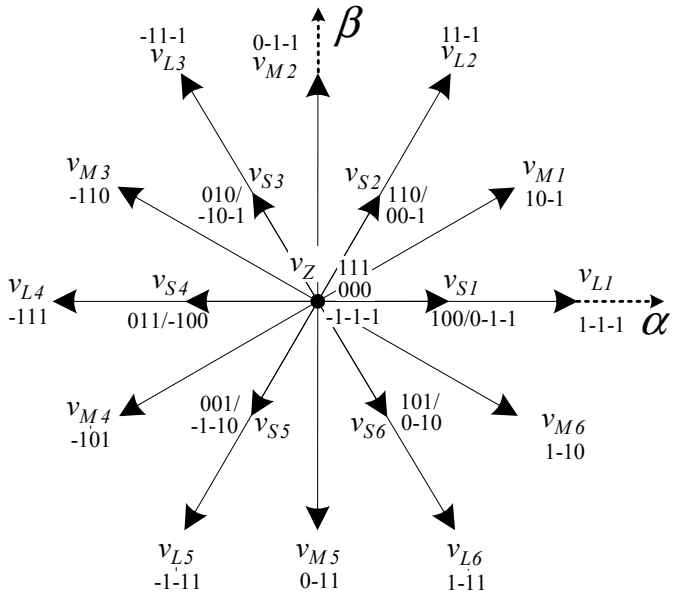

Figure 2.7: Output voltage vectors of a 3L-NPC inverter on the $\alpha - \beta$ plane.

imbalance is well researched in literature and generally, the redundancy of SVVs is utilized to minimize the voltage imbalance [85], [86].

Another important issue that needs to be addressed when incorporating a 3L-NPC inverter into DTC is the smooth voltage vector switching [55]. The rapid nature of vector selection in DTC based on torque and flux errors, if uncontrolled, can result in harmonic distortions and undesirable switch stresses in the 3L-NPC inverter. The smooth voltage vector switching criteria established for 3L-DTC drives in [63], [87] limits the switching transitions in both phase and line voltages to jumps between adjacent voltage levels, i.e., the jump in either phase or line-line voltage should not be in excess of half the dc-link voltage when switching between states. Line voltage jumps increase the harmonic content in the output voltage [87] whereas phase voltage jumps may endanger the safe operation of the inverter during commutations [63], [87].

In order to adhere to smooth voltage vector switching criteria, the switching transitions in 3L-DTC should be limited to be between adjacent voltage vectors. In other words, the following smooth vector switching strategies must be followed: 1) LVVs are only allowed to switch directly to either SVVs in the same spatial

orientation or MVVs which are adjacent. 2) MVVs are only allowed to switch to adjacent LVVs or SVVs. 3) SVVs are allowed to switch to any of the adjacent LVV/MVV/ZVVs.

2.6 Review of MLI-DTC Strategies

The majority of the literature dedicated to MLI-DTC drives study 3L-NPC inverter driven 3L-DTC drives. And most of these 3L-DTC methods focus purely on the performance enhancement of classical switching table based DTC; the simplicity and robustness are often sacrificed to employ complicated and machine parameter dependent control methods such as SVM-DTC [87] and MPC-DTC [63], [64], [88].

In [87], two 3L-DTC schemes, a DSVM-DTC and a switching table based classical 3L-DTC, using a 3L-NPC inverter are proposed for the control of an induction motor. In the proposed DSVM-DTC, a number of synthesized voltage vectors are proposed to address the issue of neutral point voltage control and smooth voltage vector switching. Though a constant inverter switching frequency is attained, up to nine switching transition occur within each sampling cycle. As a result, the average switching frequency is more than three times the classical 3L-DTC method presented in the same paper. Furthermore, experimental results under external disturbances show that the transient response of the DSVM-DTC is relatively poor due to the modulation technique used for DSVM. In other words, when a sudden change in torque is demanded, the synthesized voltage vectors are not large enough to provide the required torque.

The issues of smooth voltage vector switching and capacitor voltage balancing is also addressed in the classical 3L-DTC method in [87], which uses three-level hysteresis controller levels $(\pm 1, 0)$ for both torque and flux control. To achieve comparable results to the DSVM-DTC, a sampling frequency of 30 kHz is used and this results in an average switching frequency of more than 2 kHz. Even then, the low speed performance of the DSVM-DTC method is clearly superior at low

speeds. This is not surprising, considering the torque slope characteristics of the motor which increases as the motor speed decreases.

The model predictive 3L-NPC inverter based 3L-DTC proposed in [63], [64] predict future switching transitions to attain low torque and flux ripples with low switching frequencies while strictly following the criteria for smooth voltage vector switching and neutral point voltage control. Nevertheless, increasing the horizon ($N > 1$), means that the computational burden is high.

A FS-PTC scheme for induction motor supplied from a 3L-NPC inverter is proposed in [88]. Experimental comparisons to classical DTC and FOC schemes in terms of torque and flux ripples, stator current THD, neutral point voltage, average switching frequency and transient responses, while operating at a similar switching frequency, show that the steady state and transient performance of the proposed FS-PTC are clearly superior. However, the increase in computational time compared to classical DTC and FOC is almost six and three times, respectively. Also, the issue of smooth voltage vector switching is not mentioned; although excellent THD in the stator current is reported. Nonetheless, the lack of smooth vector switching control could endanger the safe operation of the inverter [87]. Similar to the MPC-DTC in [63], [64], the need for model-based nature of predictive control inevitably makes the proposed method [88] machine parameter dependent.

In [89], a 3L-NPC inverter fed 3L-DTC method that uses a modified DTFC method is proposed. Instead of using conventional SVM after the reference voltage is determined, a single voltage vector that is nearest to reference voltage is applied to the stator. When compared to classical 2L-DTC, the proposed method achieves an appreciable reduction in torque and flux ripples during steady state while operating at approximately half the average switching frequency. Nevertheless, poor transient response and increased complexity can be expected in [89] due to the use of multiple PI controllers, coordinate transformation and the complicated method used to find the nearest vector. Again, the issue of smooth voltage vector switching is ignored.

DDTC methods for 3L-NPC inverter driven Induction motor are proposed in [90]–[92] in which different approaches are used for the selection of voltage vectors and the subsequent determination of duty ratios. Nonetheless, both approaches are complicated, machine parameter dependent and do not address the inverter switching limitations.

In [90], a two-level flux and a modified four-level torque hysteresis controllers are used. The voltage vector space in the $\alpha - \beta$ plane is divided into twelve sectors. A switching table is developed off-line by calculating the average torque slopes of voltage vectors and the subsequent ranking of these vectors in each sector based on their torque slope magnitude. Then, considering the maximum torque slope possible in the machine, the desired torque slope that is required from the voltage vector to be applied during the next sampling cycle is predicted. Subsequently, the average toque slopes of all applicable voltage vectors are compared to the desired torque slope and the voltage vector that produces the minimum torque overshoot, i.e., the voltage vector which produces the minimum absolute difference, is used as the first vector. A second voltage vector may then be applied if the predicted actual torque reaches either the reference torque or the upper/lower bounds of torque hysteresis control.

Although effective reduction of torque ripples is confirmed by the results presented in [90], the accuracy of this method is dependent on machine parameter variations; the off-line calculation of average torque slopes and the on-line prediction of desired torque slopes and the determination of duty cycle during each sampling cycle use the theoretical torque slope equation of an induction motor, analogous to the torque variation rate defined in (2.18) for a PMSM. Furthermore, as the focus of the proposed algorithm is purely torque ripple control, smooth voltage vector switching is not considered. Consequently, poor stator flux regulation ensues and high THD in the outputs are clearly noticeable in the results presented; in fact, the THD reported for the stator current is even higher than the classical DTC under certain operating conditions.

The DDTC method in [91], [92] uses the TR-RMSM for the determination of duty ratios. Depending on the speed of the machine, two or more voltage vectors are applied within one switching cycle during normal operating conditions to reduce the torque ripple. The proposed method is capable of significant reduction in torque ripples while maintaining low inverter switching frequencies. However, the TR-RMSM method used for determining the duty ratio of voltage vectors requires the knowledge of torque variation rates, which are determined using theoretical torque slope equation of an induction motor. This makes the veracity of [91], [92] susceptible to variations in machine parameters.

The TR-RMSM approach adopted in [91], [92] is similar to the method used in [78] for a 2L-DTC drive; the only difference is that more than two voltage vectors are frequently used in [91], [92] during a switching period. The comparative analysis presented in [80] for 2L-DTC drives show that machine parameter dependent TR-RMSM based DTC algorithms such as [78] exhibit inferior torque regulation capability when compared to other DDTC methods that has minimal machine parameter dependence (see Table 2.1).

As two or more voltage vectors are applied during each switching cycle, the duty ratio solutions obtained through TR-RMSM in [91], [92] are much more complicated and tedious than [78]. Moreover, similar to the classical 3L-DTC scheme proposed in [93], MVVs are not utilized in [91], [92] during normal conditions and this will increase the occurrence of flux drooping at the sector boundaries when the motor is heavily loaded, even during medium to high speeds.

To alleviate the flux drooping problem, a modified switching table is proposed in [91]–[93] for low speed operations, in case the stator flux droops below a set value. However, in the modified switching table MVVs are used. From (2-18) it follows that MVVs have large torque slopes at lower speeds. Consequently, to improve the torque regulation in [91]–[93], switching transitions to a second MVV are allowed in the same sampling cycle. This clearly violates the smooth vector switching criteria established in [63], [87].

Some studies are reported in the literature for DTC drives integrating inverters with more than three-levels [94]–[99]. In [94], a five-level FCC inverter fed DTC drive is proposed for the control of an induction motor. Voltage vectors are selected based not only on three-level torque and two-level flux hysteresis control but also the operating speed. In other words, voltage vectors with low amplitude are used for low speed while higher amplitude vectors are used for high speeds. Consequently, four separate switching lookup tables are required which increases the complexity.

The MLI-DTC methods that have been reviewed in this section up to this point [63], [64], [88]–[94], are all inverter specific, i.e., the level of hysteresis controllers used and the proposed switching tables are designed purely for one specific inverter topology. Hence, these methods are not readily applicable to generic n-level inverter fed MLI-DTC drives. Only a handful of generalized MLI-DTC algorithms exist in literature that can be applied to inverters with any number of levels [95]–[99]. Among these, the DTC of an induction motor drive fed by a seven-level hybrid CHB MLI is proposed in [95], [96] in which the results presented clearly demonstrate the ability of MLIs in improving the torque regulation. However, the proposed method is essentially an extension of the classical DTC to MLI-DTC using the vector decomposition method proposed in [97]. Therefore, no additional torque ripple reduction measures are used, and the inverter switching frequency is inevitably variable.

In contrast, the approaches in [97]–[99] use a frequency imposition technique based on predictive control to minimize the variations in switching frequency. The method in [97], [98] is experimentally verified using three-level and four-level inverters, while an eleven-level CHB inverter is used in [99] to drive an induction motor. In all three methods [97]–[99], Voltage vectors are commuted once within each sampling period to achieve zero torque error at the end of each sampling period. Consequently, a constant switching frequency is imposed and torque ripples are reduced. Nonetheless, the prediction of torque dynamics one step in advance

is required for determining the duty ratios of the applied voltage vectors. The predictive model used is inevitably machine parameter dependent, and thus, the accuracy of the proposed methods is susceptible to possible variations in the machine parameters.

2.7 Conclusion

In this chapter, an overview of the DTC strategy for an IPMSM has been presented. The principle of torque production in an IPMSM is described mathematically to recognize and discuss the advantages and shortcomings of a direct torque controlled IPMSM drive. Subsequently, advanced DTC methods in the literature are studied to have an understanding of the current trends and developments that have improved the performance of classical DTC. It is seen that the integration of MLIs into DTC drive has been acknowledged as a solution for mitigating the shortcoming of classical DTC. In the recent years, with the availability of powerful and cost-effective microprocessors, the use of MLIs in high- performance motor drives has been on the rise, especially in the medium to high power drives.

The physical model of a 3L-NPC inverter, one of the most commonly used inverter for variable speed drives, is introduced to explain the increase in the degree of freedom for voltage vector selection in MLI-DTCs and how this can be used to achieve a better torque and flux control in IPMSMs. At the same, the complexities and switching constraints involved in the 3L-NPC driven DTC drive are discussed. Lastly, a comprehensive review of the MLI-DTC algorithms in the literature is presented to identify the problems associated with these methods; the finding can be briefly summarized:

- In classical 3L-DTC, even with the increase in the number of voltage vectors, high sampling frequencies (20 kHz) are often required to ensure acceptable torque and flux responses. Even with high frequency sampling, the switching frequency remains variable.

- In some advanced 3L-DTC methods, the simplicity and robustness of classical DTC are often sacrificed to employ effective but complicated control methods such as space vector modulation (SVM-DTC) and predictive control (P-DTC).

- The DDTC algorithms, which have demonstrated markedly improved performance with slight increment in complexity in 2L-DTC drives, are also employed in 3L-DTC drives. Nonetheless, the DDTC methods employed in 3L-DTC are often parameter dependent and found to be more complicated than in 2L-DTC, mainly due to the increase in the number of voltage vectors.

- Due to the same reason above, the inverter inherent switching constraints that degrade the performance and safe operation of the drive system are completely ignored in the existing DDTC algorithms for 3L-DTC.

- Lastly, it has been identified that very few of the MLI-DTC algorithms proposed in the literature are readily applicable to MLI-DTCs driven by inverters possessing any number of voltage levels.

- And out of the handful of MLI-DTC that is readily applicable to a generic n-level inverter, it is found that model predictive control is applied to achieve acceptable torque regulation and to minimize the variations in the switching frequency.

Chapter 3

Two-Vector Based DDTC Strategy for 3L-DTC of IPMSM

3.1 Motivation and Objectives

This chapter focuses on the development of a novel DTC method for a 3L-NPC inverter fed IPMSM drive. Theoretically, in comparison to a two-level inverter, a 3L-NPC inverter is advantageous for reducing the torque and flux ripples in DTC drives. Nonetheless, the ripples can still be excessive and detrimental if low inverter switching frequencies are desired. To reduce the torque and flux ripples while maintaining a low average switching frequency in 3L-DTC drives, a switching table based DDTC scheme is proposed in this chapter.

The review of advanced DTC algorithms in chapter 2 shows that DDTC methods are an effective way to improve the torque and flux regulation in classical DTC, albeit with small increment in complexity. At the same time, it is clear that the existing DDTC algorithms for 3L-DTC drives employ machine parameter dependent analytical solutions for determining the duty cycle/ratio of multiple voltage vectors applied within each sampling cycle. Besides, the necessary restrictions on switching commutations are never considered in the implementation of these DDTC methods.

To alleviate the aforementioned drawbacks, a duty ratio calculation method with minimal parameter dependency is developed in this chapter, taking into ac-

count the dynamic torque and flux characteristics of an IPMSM. In addition, the proposed method respects the switching constraints of the 3L-NPC inverter in developing the switching table and the voltage vector selection criteria used for the DDTC strategy. Experimental results during transient and steady state conditions, parametric robustness analysis and comparative study against classical 3L-DTC and the DDTC method in [90] are presented to prove the effectiveness of the proposed method.

This rest of the chapter is structured as follows. In Section 3.2, the extent of dependency that the operating speed and load torque has on torque variation rate is studied in detail to develop the switching table. The duty ratio calculation method is introduced in Section 3.3. The optimization of design parameters and the voltage vector switching sequencing in the proposed method are presented respectively in Sections 3.4 and 3.5. Experimental results and discussions are provided in Section 3.6.

3.2 Switching Lookup Table

The proposed torque ripple reduction strategy is based on the TR-RMSM approach and utilizes two voltage vectors in each sampling/switching cycle. From here onwards in this chapter, the main vector to be applied in a switching cycle will be termed "active", whereas the non-active vector will be termed "passive".

To take advantage of the higher degree of freedom offered by the 3L-NPC inverter, the $\alpha - \beta$ plane containing the output voltage vectors in Fig. 3.1 is divided into twelve equal sectors of 30° (S_{1a}, S_{1b}, S_{2a}, ..., S_{6b}), with the first sector S_{1a} ranging from $-\pi/6$ to 0. Subsequently, a switching logic is developed based on a four-level torque ($\epsilon_T = \pm 2, \pm 1$) and a two-level flux ($\epsilon_\psi = \pm 1$) hysteresis control as shown in Fig. 3.2. The proposed torque hysteresis controller is similar to the five-level torque hysteresis controller found in the literature for MLI-DTC of induction motor drives, for instance in [90] and [91], except that the zero level, ($\epsilon_T = 0$) is not used. This is because the use of zero level (i.e., the use of ZVVs) is

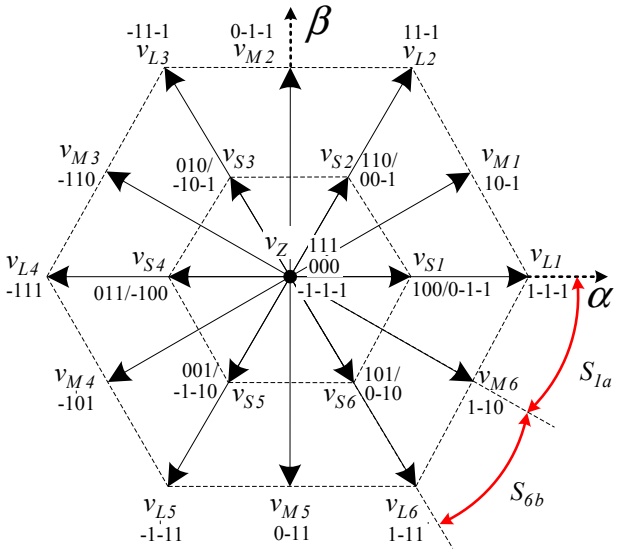

Figure 3.1: 3L-NPC inverter voltage vectors and the sector division of the $\alpha - \beta$ plane.

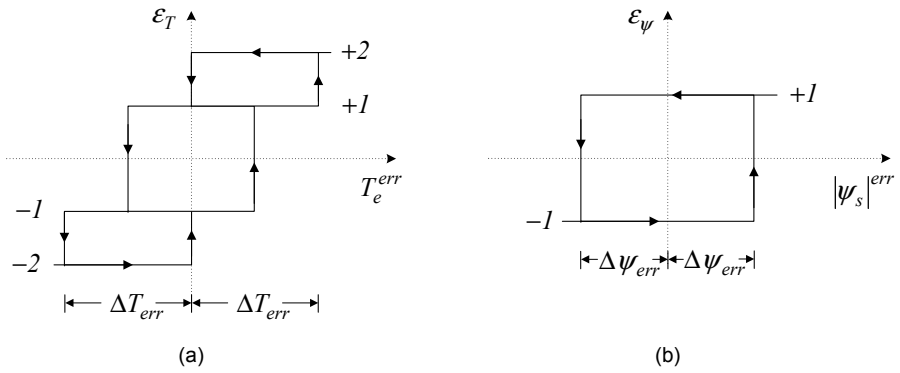

Figure 3.2: Hysteresis controllers used in the proposed 3L-DTC drive. (a) Torque hysteresis controller. (b) Flux hysteresis controller.

usually not recommended for fast torque control in PMSM drives [39], as previously discussed in Chapter 2.

The resultant switching table which utilizes all the voltage vectors of the 3L-NPC inverter is presented in Table 3.1. The active voltage vectors in Table 3.1 are selected based on their instantaneous potential to change torque and flux dynamics, similar to the methodology adopted generally in conventional DTC. When there is a large difference between the reference torque and the estimated actual torque, i.e., for high torque demand ($\epsilon_T = \pm 2$), the voltage vectors that lie on the outer

Table 3.1: Switching Table For The Proposed 3L-DTC Drive

	Flux	+1				-1			
	Torque	-2	-1	+1	+2	-2	-1	+1	+2
Sector Ska	v_{active}	$v_{M\,k-2}$	$v_{S\,k-1}$	$v_{S\,k+1}$	$v_{L\,k+1}$	$v_{L\,k-2}$	$v_{S\,k-2}$	$v_{S\,k+2}$	$v_{M\,k+1}$
	$v_{passive}$	$v_{S\,k-1}$	v_z	v_z	$v_{S\,k+1}$	$v_{S\,k-2}$	v_z	v_z	$v_{S\,k+2}$
Skb	v_{active}	$v_{L\,k-1}$	$v_{S\,k-1}$	$v_{S\,k+1}$	$v_{M\,k+1}$	$v_{M\,k-2}$	$v_{S\,k-2}$	$v_{S\,k+2}$	$v_{L\,k+2}$
	$v_{passive}$	$v_{S\,k-1}$	v_z	v_z	$v_{S\,k+1}$	$v_{S\,k-2}$	v_z	v_z	$v_{S\,k+2}$

perimeter of the voltage vector space, the LVVs or the MVVs are chosen as active vectors to maximize the use of dc-link voltage. For the low ($\epsilon_T = \pm 1$) levels of torque demand, SVVs are used as active vectors.

Ideally, to maximize the reduction in torque ripples produced, the passive or the second voltage vector to be applied in a switching cycle should have a torque slope that counteracts the slope of the active voltage vector. However, when selecting the passive vector, inverter switching constraints must be given precedence, and this limits the selection of passive vector to vectors that are adjacent to the active voltage vector. Therefore, further analysis of torque slope characteristics in the studied IPMSM drive is required for the appropriate selection of passive vectors and the subsequent duty ratio calculations.

By substituting in the parameters of the IPMSM drive (see Appendix A) into (2.18), the torque slope characteristics of the voltage vectors can be plotted. For instance, the torque slopes corresponding to vectors v_{L3}, v_{S3} and v_Z are normalized against the peak torque slope, $\widehat{\nabla} T_e$ in the stator flux angular region of $0° \leq \theta_s \leq 90°$ in Fig. 3.3. Note that for the approximation of the torque angle δ for the calculation of ψ_{rx} in (2-18), the maximum torque per ampere strategy proposed in [100] is used.

From Fig. 3.3, the following observations can be made when the operating speed of the machine is increased: 1) ZVVs have negative torque variation rates; 2) the torque variation rates of SVVs decrease as the motor speed is increased.

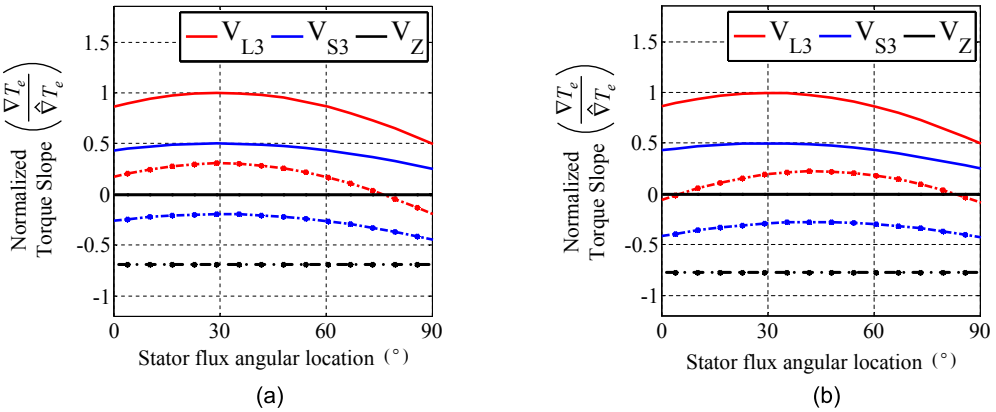

Figure 3.3: Approximate changes in torque variation rates of voltage vectors, v_{L3}, v_{S3} and v_Z in the region of ($0° \leq \theta_s \leq 90°$), during one sampling period. (Solid line: zero speed with no load, dashed line ($*-$): (a) Rated speed with no load. (b) Rated speed with a load of 5Nm).

In fact, it eventually becomes negative near the rated speed. Based on these rationales, a torque ripple reduction strategy is devised through the application of either SVVs or ZVVs as the passive vector.

When the torque demand is high ($\epsilon_T = \pm 2$), either a LVV or a MVV is selected as the active vector as shown in Table. 3.1. An adjacent SVV that is normally used as the active vector when the torque demand is low ($\epsilon_T = \pm 1$), is chosen as the passive vector. For instance, in sector S_{1a}, if the torque and flux demand are +2 and +1 respectively, then v_{L2} (v_{LK+1}) is selected as the active vector while v_{S2} (v_{sk+1}) is selected as the passive vector.

When the torque demand is low ($\epsilon_T = \pm 1$), a SVV is selected as the active vector, while a ZVV is chosen as the passive vector. For example, in sector S_{1a}, if the torque and flux demand are +1 and +1 respectively, then v_{S2} (v_{SK+1}) is selected as the active vector while one of the v_Z is selected as the passive vector. The selection of v_Z is determined by the minimum number of transitions between switching states so that the average switching frequency can be reduced. e.g., 110 $\rightarrow$ 111, 00-1 $\rightarrow$ 000.

3.3 Duty Ratio Calculation

The determination of appropriate time intervals for the active and passive vectors is crucial. An expected torque response in a sampling/switching period T_s when LVVs/MVVs (active) are used in conjunction with SVVs (passive) is shown in Fig. 3.4(a). Similarly, in Fig. 3.4(b), one likely scenario when a SVV (active) is used in combination with a ZVV (passive) is shown. In both instances, torque variation rates s_1 and s_2 can be considered to be constants within a sampling period. This is reasonable since T_s is usually very small [79], [80].

Subsequently, TR-RMSM approach which aims to minimize the root mean square of the torque ripple in a switching period is applied to determine the duty ratio of the active vector, D_{act}. The square of root mean square torque ripple can be expressed as

$$T_{e_{ripple}}^2 = \frac{1}{T_s} \int_{kT_s}^{(k+1)T_s} (T_e^* - T_e)^2 dt \tag{3.1}$$

where T_e^* is the torque reference. By taking the derivative of (3.1) with respect to the time duration of the active vector, the duty ratio of the active voltage vector to minimize the torque ripple can be obtained as [78]

$$D_{act} = \frac{2(T_e^* - T_e^0) - s_2 T_s}{T_s(2s_1 - s_2)} \tag{3.2}$$

where T_e^0 is the initial value of torque. An accurate solution for the optimal duty ratio is attained through (3.2). Nevertheless, the slopes of s_1 and s_2 which are usually determined analytically by using (2.18), make (3.2) complicated and dependent on the accuracy of machine parameters. Furthermore, (3.2) is greatly affected by the inevitable one-cycle delay introduced in practical discrete systems, as proved in [79].

To alleviate these drawbacks, a simplified duty ratio calculation method that is robust to changes in machine parameters is developed for the proposed 3L-DTC drive, by building onto the theoretical background established in [80].

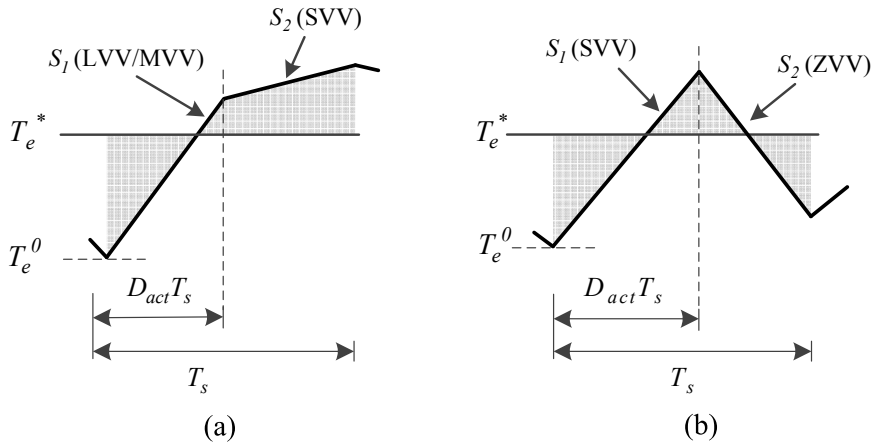

Figure 3.4: Typical steady state torque ripple when (a) LVV/MVV is used in conjunction with SVV as the passive vector (b) SVV is used in conjunction with ZVV as the passive vector.

The results in Fig. 3.3 also illustrates that the torque slopes of the voltage vectors are significantly influenced by the machine operating speed and to a smaller extent, the load torque. The influence of load torque originates from the first term in (2.8) and the change in load angle δ. Nevertheless, the reduction in torque variations noted in Fig. 3.3(b) due to the increment in load torque, are small and negligible when compared to that of the operating speed. This aspect is further substantiated by the data presented in Fig. 3.5.

In Fig. 3.5(a), the normalized torque slopes of a LVV v_{L3} in the region $0° \leq \theta_s \leq 90°$, under different operating conditions, are shown while Fig. 3.5(b) depicts the normalized peak slope of v_{L3} as the load torque and operating speeds are varied. Note that the IPMSM used in this study has a rated speed and torque of 500rpm and 5Nm, respectively. From, Figs. 3.3 and 3.5, the following observations can be made:

- When the motor is unloaded ($T_e = 0$), the torque slope at zero speed (marked as x_1 in Fig. 3.5) reduces to about one-third of its value at the rated speed (x_3).

- In comparison, the torque slope variation caused by the change in electro-

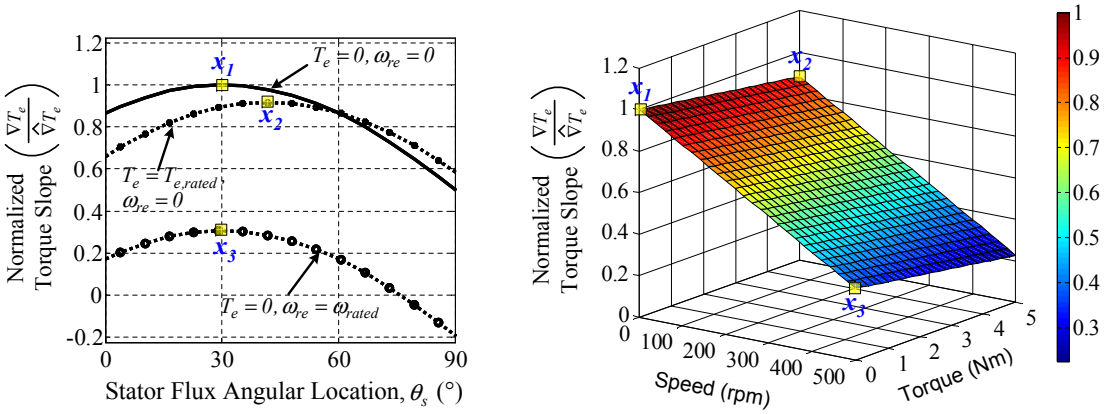

Figure 3.5: Approximate torque slope characteristics of the LVV, v_{L3}. (a) Torque slope in the stator flux angular region of ($0° \leq \theta_s \leq 90°$). (b) Peak torque slope.

magnetic torque is small. Quantitatively, the decrement observed in torque slope at standstill ($\omega_{re} = 0$) when the machine is fully loaded (x_2) is approximately less than one-tenth of its value at no load (x_1).

- The torque slope decreases proportionally as the machine speed increases at constant load torque. In other words, the reduction seen in torque slope is proportional to the operating speed when the load torque is kept constant.

Consequently, for simplifying the duty ratio calculations, the effects of instantaneous changes in load torque are not considered in the proposed method. Only the instantaneous torque error and the changes in operating speed are taken into account for determining the duty ratios of the three vector combinations that are possible with the proposed 3L-DTC method, namely LVV-SVV, MVV-SVV and SVV-ZVV. The duty ratios of the active vector in these vector combinations are derived in the following subsections and subsequently, tabulated in Table 3.2.

3.3.1 LVV-SVV

For increasing torque demand ($\epsilon_T = +2$), the torque slope of the active vector LVV at zero speed (s_L^0) and the rated speed (s_L^n) is approximated in (3.3), where

k is the factor by which torque slope of LVV differs at the rated speed ω_n with respect to the slope at zero speed (s_0). By the same token, the torque slope for the passive SVV is shown in (3.4).

$$s_L^0 = s_0 \qquad\qquad s_L^n = ks_0 \tag{3.3}$$

$$s_{SL}^0 = 0.5s_0 \qquad\qquad s_{SL}^n = (k-1)s_0 + 0.5s_0 \tag{3.4}$$

From (3.3) and (3.4), the general expressions for the slope of active LVV (s_L^+) and passive SVV (s_{SL}^+) for a positive torque demand (indicated by the "+") are derived as

$$s_L^+ = \frac{(k-1)s_0}{\omega_n}\omega_r + s_0 \tag{3.5}$$

$$s_{SL}^+ = \frac{(k-1)s_0}{\omega_n}\omega_r + 0.5s_0 \tag{3.6}$$

Substituting (3.5) and (3.6) into (3.2) as s_1 and s_2, respectively, the duty cycle for LVV when torque demand is high and positive, can be expressed as

$$D_L^+ = \frac{2(T_e^* - T_e^0) - 0.5C_1 - C_2\omega_r}{1.5C_1 + C_2\omega_r} \tag{3.7}$$

where, C_1 and C_2 are design parameters that are introduced to minimize the parametric dependence of the proposed method. The design guidelines used for the selection and fine-tuning of C_1 and C_2 are explained in Section 3.4.

By following the same rationales used in (3.5)-(3.7), the duty cycle of the active vector for decreasing high torque demand (-2) can be expressed as

$$D_L^- = \frac{2(T_e^* - T_e^0) - 0.5C_1 - C_2\omega_r}{-1.5C_1 + C_2\omega_r} \tag{3.8}$$

3.3.2 MVV-SVV

Unlike the LVV-SVV combinations, the active and passive vectors in the MVV-SVV combinations do not lie in the same spatial orientation. For instance, Fig.

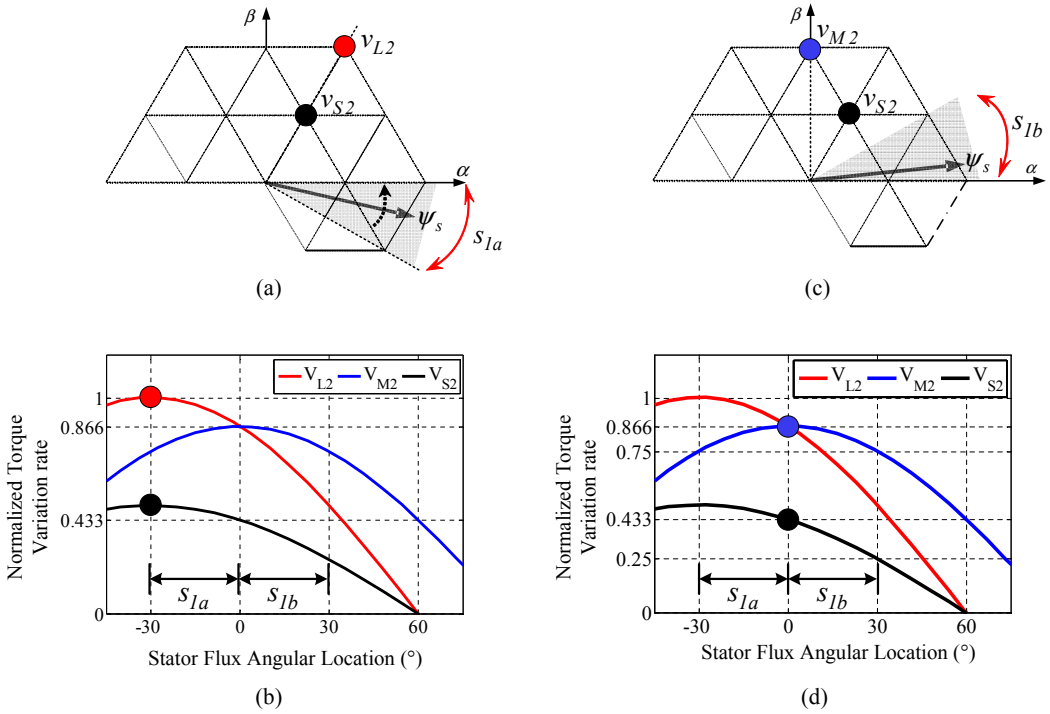

Figure 3.6: Voltage vector selection for high torque (+2) and flux (+1) demand in; (a) and (b) sector S_{1a}. (c) and (d) sector S_{1b}

3.6 shows the vectors combinations used in sectors S_{1a} and S_{1b} when torque and flux demands are +2 and +1, respectively.

In sector S_{1a}, the chosen non-zero vector combination $v_{L2} - v_{S2}$ is spatially aligned in the $\alpha - \beta$ plane, as shown in Fig. 3.6(a). The normalized torque slopes of the selected vectors and their peak values are shown in Fig. 3.6(b); the red dot represents s_0, the maximum torque slope of a LVV at zero speed (3.3).; the black dot indicates $0.5s_0$, the maximum torque slope of a SVV at zero speed (3.4). It can be noticed that a constant ratio of 0.5 is maintained between the torque variation rate/slope of LVV and SVV within the sector S_{1a}.

In contrast, when the vector combination of $v_{M2} - v_{S2}$ is used in sector S_{1b}, it is evident from Figs. 3-6(c) and 3-6(d) that the MVV and the SVV are not spatially aligned in the $\alpha - \beta$ plane. In fact, the torque slope ratio of a SVV to a MVV varies from 0.5 to 0.33 in a sector as shown in Fig. 3-6(d). Consequently, for increasing torque demand (+2), the torque slopes of the active vector MVV and

the passive vector SVV at zero speed and the rated speed can be approximated as

$$s_M^0 = \sqrt{3}/2 s_0 \qquad s_M^n = (k-1)s_0 + \sqrt{3}/2 s_0 \tag{3.9}$$

$$s_{SM}^0 \approx \sqrt{3}/4 s_0 \qquad s_{SM}^n \approx (k-1)s_0 + \sqrt{3}/4 s_0 \tag{3.10}$$

The selected values of $\sqrt{3}/2 s_0$ and $\sqrt{3}/4 s_0$, as indicated respectively by blue and black dots in Fig. 3-6(d), correspond to the highest ratio of 0.5 between the torque slope of a SVV and a MVV. These values are deliberately chosen as the duty ratio of the active vector (MVV) will always be the highest at this point within the sector. Though this may result in slightly increased torque ripples, torque demand can be satisfied in a better fashion at all times within a sector. Subsequently, the duty ratio of a MVV, as the active vector is derived for increasing (D_M^+) and decreasing (D_M^-) torque demands as

$$D_M^+ = \frac{2(T_e^* - T_e^0) - 0.433C_1 - C_2\omega_r}{1.299C_1 + C_2\omega_r} \tag{3.11}$$

$$D_M^- = \frac{2(T_e^* - T_e^0) - 0.433C_1 - C_2\omega_r}{-1.299C_1 + C_2\omega_r} \tag{3.12}$$

3.3.3 SVV-ZVV

For increasing torque demand (+1), the torque slopes of the active vector SVV and the passive vector ZVV at zero speed and the rated speed can be approximated as

$$s_S^0 = 0.5 s_0 \qquad s_S^n = (k-1)s_0 + 0.5 s_0 \tag{3.13}$$

$$s_{ZS}^0 = 0 \qquad s_{ZS}^n = (k-1)s_0 \tag{3.14}$$

Accordingly, the duty cycle for SVVs when torque demand is increasing (D_S^+)

Table 3.2: Duty Ratio of the Active Vector, D_{act}

Vector Combination	Increasing Torque Demand, $\varepsilon_T = \{+2,+1\}$	Decreasing Torque Demand, $\varepsilon_T = \{-2,-1\}$
LVV-SVV	$\frac{2\left(T_e^* - T_e^o\right) - 0.5C_1 - C_2\omega_r}{1.5C_1 + C_2\omega_r}$	$\frac{2\left(T_e^* - T_e^o\right) - 0.5C_1 - C_2\omega_r}{-1.5C_1 + C_2\omega_r}$
MVV-SVV	$\frac{2\left(T_e^* - T_e^o\right) - \sqrt{3}/4\,C_1 - C_2\omega_r}{1.299C_1 + C_2\omega_r}$	$\frac{2\left(T_e^* - T_e^o\right) - \sqrt{3}/4\,C_1 - C_2\omega_r}{-1.299C_1 + C_2\omega_r}$
SVV-ZVV	$\frac{2\left(T_e^* - T_e^o\right) - C_2\omega_r}{C_1 + C_2\omega_r}$	$\frac{2\left(T_e^* - T_e^o\right) - C_2\omega_r}{-C_1 + C_2\omega_r}$

where $C_1 = s_o T_s,\ C_2 = C_1\left(k-1\right)/\omega_n$

and decreasing (D_S^-) can be obtained as

$$D_S^+ = \frac{2(T_e^* - T_e^0) - C_2\omega_r}{C_1 + C_2\omega_r} \tag{3.15}$$

$$D_S^- = \frac{2(T_e^* - T_e^0) - C_2\omega_r}{-C_1 + C_2\omega_r} \tag{3.16}$$

3.4 Design Guidelines of Parameters C_1 and C_2

The design parameters C_1 and C_2 are related and can be expressed as

$$C_1 = s_0 T_s \qquad\qquad C_2 = \frac{(k-1)C_1}{\omega_n} \tag{3.17}$$

C_1 is proportional to the torque slope at zero speed s_0, i.e., the maximum positive torque slope available which corresponds to the torque slope of a LVV at zero speed. It can be observed in Figs. 3.3 and 3.5 that the torque variation of a LVV changes in a sinusoidal fashion. Hence, s_0 can be approximated as

$$s_0 \approx \widehat{\nabla} T_e \sin(\theta + 75^\circ) \qquad\qquad -15^\circ \leq \theta \leq 15^\circ \tag{3.18}$$

where $\widehat{\nabla} T_e$ denotes the peak torque slope of the IPMSM, which can be approximated by substituting the motor drive parameters into (2.18). For instance, the peak torque slope of the IPMSM used in this study is approximately 6250 Nm/s.

Conversely, C_2 is proportional to C_1. It is also dependent on the factor k, which signifies the maximum deterioration of torque slope in the machine. The range of values of k can be approximated by comparing the peak torque slope of a LVV at $T_e = 0$, $\omega_{re} = 0$ to its peak torque slope at $T_e = 0$, $\omega_{re} = \omega_{rated}$. From the torque variation characteristics shown in Figs. 3.3 and 3.5, the factor k for the IPMSM used in this study can be estimated as

$$0.25 \leq k \leq 0.45 \tag{3.19}$$

It is clear that both (3.18) and (3.19) are machine parameters dependent. Therefore, it needs to be pointed out that the range of values computed for C_1 and C_2 in (3.17) are to be used purely as a starting point for the subsequent fine-tuning which is necessary to: 1) optimize the torque ripples in the drive; 2) ensure that the proposed method is not affected by the unknown variations in the machine parameters. In other words, if the known machine parameters are inaccurate in the first place, the proposed method can still be tuned to optimize the torque ripple reduction.

From (3.17), by using the maximum torque slope (s_0 =6250 Nm/s) and the maximum deterioration of torque slope ($k = 0.25$), the values of C_1 and C_2 are respectively, 1.25 and -0.001875; for a sampling frequency of 5 kHz ($T_s = 200\mu s$), in accordance with the experiments. Subsequently, the duty ratio characteristics of the active vector for LVV-SVV and SVV-ZVV combinations are plotted in Fig. 3.7 using (3.7) and (3.15), respectively, for the entire range of operating speed, and a reasonable range of torque error.

Some important characteristics can be noticed from Fig. 3.7. Firstly, the increase in duty ratio is almost proportional to the torque error for both vector combinations. This shows that the proposed method regulates the duty ratio according to instantaneous torque error.

Secondly, it can be observed that the usage of LVV is limited at lower speeds when the torque error is low. Limiting the use of LVVs, which have high torque

slope at lower speeds, helps to reduce torque ripples. Thirdly, for the SVV-ZVV combination (see Fig 3.7(b)), the duty ratio of the active vector SVV is clamped to 1 at higher speeds, even when the torque error is very small. This inhibits the usage of ZVVs in the high speed regions and therefore, larger undershoots in torque can be avoided.

3.4.1 Tuning of C_1

The influence exerted by C_1 on the duty ratio calculation is demonstrated in Fig. 3-8, when C_1 is reduced by 20% to 1.0. The significant difference compared to Fig. 3-7 is that duty cycle regulation is more relaxed; the instances where the duty ratio of the active vector is clamped to the maximum ($D_{act} = 1$) are increased. This implies that the torque ripples produced could increase. At the same time, since active vectors are applied with a comparatively higher duty ratio, the dynamic torque response of the drive can be improved. Consequently, C_1 should always be designed to achieve a good compromise between the dynamic torque response and the steady state torque regulation.

3.4.2 Tuning of C_2

The effects of varying C_2 are shown Fig. 3.9 when C_2 is reduced by 20% while C_1 is maintained at 1.25. When compared to Fig. 3.7, it is seen that C_2 mainly influences the duty cycle characteristics during higher speed operations for low torque errors. Reducing C_2 will improve torque ripples as the duty ratio of the active vector is reduced. Nevertheless, attention should be given to the amount of reduction in C_2 to prevent large undershoots of torque that could occur due to the increased use of passive vectors, especially at very high speeds (i.e., near the rated speed).

Once adjusted, C_1 and C_2 can be considered constants to be used for duty cycle control under all operating conditions. The real-time machine parameter variations

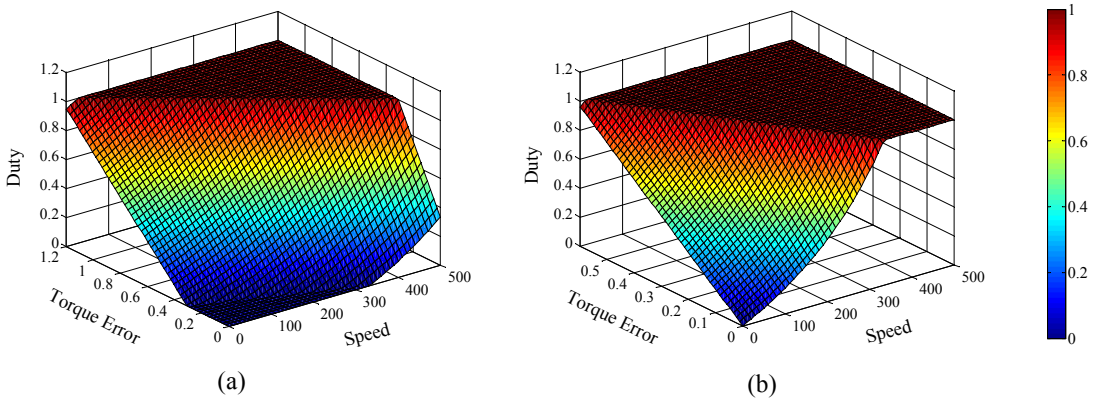

Figure 3.7: Duty ratio characteristics of voltage vector combinations with untuned design parameters, $C_1 = 1.25, C_2 = -0.001875$. (a) LVV-SVV. (b) SVV-ZVV.

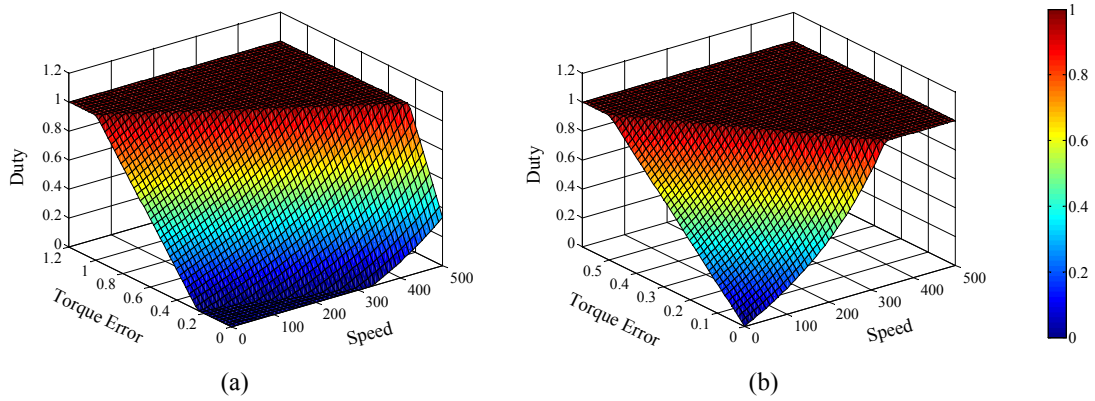

Figure 3.8: Duty ratio characteristics of voltage vector combinations as C_1 is reduced by 20%, $C_1 = 1.0, C_2 = -0.001875$. (a) LVV-SVV. (b) SVV-ZVV.

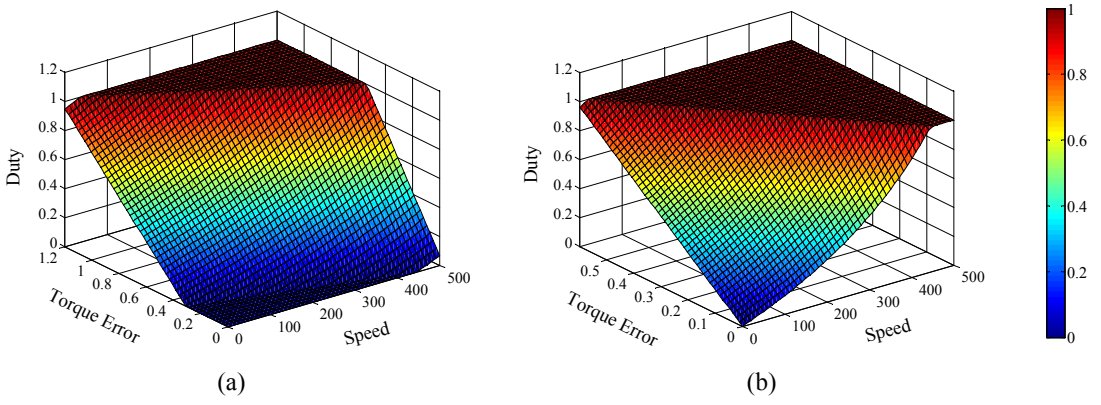

Figure 3.9: Duty ratio characteristics of voltage vector combinations as C_2 is reduced by 20%, $C_1 = 1.25, C_2 = -0.0015$. (a) LVV-SVV. (b) SVV-ZVV.

have limited impact on the control performance of the proposed method, which is substantiated by the experimental results presented in Section 3.6.

3.5 Voltage Vector Sequencing

The important aspects of smooth voltage vector switching and neutral point voltage balancing have to be considered when applying the voltage vectors to the stator terminals.

3.5.1 Smooth voltage vector switching

To begin with, the switching table developed for the proposed 3L-DTC is conducive to smooth voltage vector switching criteria established in [63] and [87]. As highlighted earlier, the flux hysteresis band width in DTC drives is usually kept small. Therefore, during steady state operation, the majority of the switching transitions in a sector occur between $+1$ and -1state of the flux hysteresis comparator. From Table 3.1 and the proposed torque ripple reduction strategy, it can be seen that the transitions that are caused purely by flux control, are simply between adjacent voltage vectors.

Additionally, the following smooth vector switching strategies are adopted to avoid the undesirable high voltage jumps: 1) LVVs are only allowed to switch directly to either SVVs in the same spatial orientation or MVVs which are adjacent. 2) MVVs are only allowed to switch to adjacent LVVs or SVVs. 3) SVVs are allowed to switch to any of the adjacent LVV/MVV/ZVVs.

In case, the aforementioned vector selection criteria cannot be satisfied when switching takes place from one switching combination to the next, an intermediate vector combination will be applied for one switching cycle. For instance, if the current combination is $v_{L2} - v_{S2}$ and the next chosen combination is v_{L3}-v_{S3}, then the applied voltage vector sequence would be $v_{L2} - v_{S2} - v_{M2} - v_{S3} - v_{L3} - v_{S3}$.

3.5.2 Neutral point voltage balancing

As explained previously, it is clearly not plausible to maintain the average neutral point current, i_n in each switching period to be zero in a switching table based 3L-DTC such as the proposed method. The onus is then to minimize the average i_n in a switching period by exploiting the redundant states of SVVs, which provide identical torque and flux responses with opposite polarity of i_n.

In the proposed 3L-DTC drive, whenever a SVV is selected, either as an active or a passive vector, an appropriate SVV that minimizes the average i_n in a switching cycle is chosen, based on the measured polarities of i_n and the neutral point voltage, v_n. The dc-link capacitor voltages are measured to determine v_n, whereas the current i_n is estimated from the knowledge of the applied voltage vectors.

Note that SVVs are frequently used in the proposed 3L-DTC method, either as passive vectors in the LVV/MVV-SVV combinations or as active vectors in the SVV-ZVV combinations. Therefore, the proposed method has the potential to maintain an acceptable level of voltage balance between the dc-link capacitors.

3.6 Experimental Results

A detailed block diagram of the proposed 3L-DTC method is illustrated in Fig. 3.10, based on which a laboratory prototype has been developed as shown in Fig. 3.11. The experimental setup consists of a digital signal processor (DSP) TMS320F28335, a DC power supply, 3L-NPC inverter and other peripheral signal conditioning circuits. The dc-link capacitors are 246μF (3 x 82μF) each, and a DC machine is coupled to the IPMSM as the load. All the experimental results are captured using the ControlDesk of DSpace DS1104 platform. The tuned design constants used for the proposed method in experiments are listed in Table 3.2.

To validate the effectiveness of the proposed duty cycle based 3L-DTC, the transient and steady state performances of the proposed 3L-DTC are compared

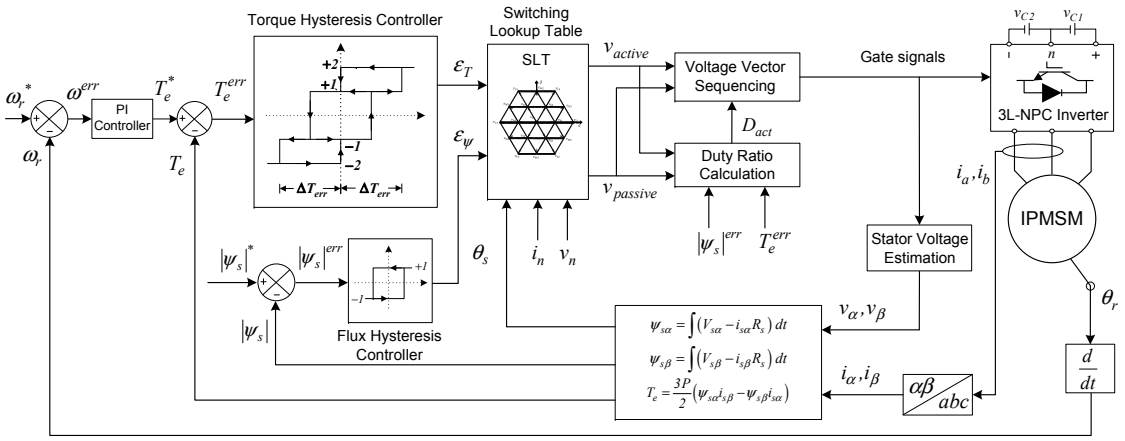

Figure 3.10: Block diagram of the proposed 3L-DTC method.

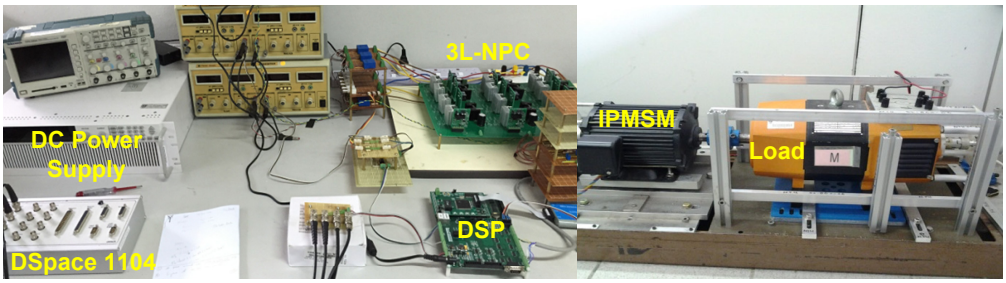

Figure 3.11: Experimental setup.

Table 3.3: Optimized design parameters

C_1	1.23	C_2	- 0.0015

with those of classical 3L-DTC and the duty cycle based 3L-DTC approach proposed in [90], which also uses two voltage vectors in a switching period to attenuate the torque ripples. For simplicity, the method in [90] is designated as DDTC-1, in the continuation of this chapter. For all three 3L-DTC algorithms, sampling frequency is set to 5 kHz. The hysteresis control used in the classical 3L-DTC setup is identical to that used in the proposed 3L-DTC setup. However, only the active vectors from the switching logic presented in Table. 3.1 are applied in the classical 3L-DTC setup during each switching cycle. DDTC-1 also employs four-level torque and two-level flux hysteresis control [90]. Consequently, in all three

3L-DTC setups, the hysteresis band for high torque level (+2) is fixed to 18% of the rated torque while the flux hysteresis band is fixed to 1% of the rated flux linkage to reduce the THD in the output current.

3.6.1 Transient performance

Firstly, the dynamic response of the torque controller (i.e., without speed controller) is investigated through reversed torque control from −4 Nm to 4 Nm. The real-time steady state and transient torque responses at a standstill are illustrated in Figs. 3.12 and 3.13, respectively. It can be observed that the torque ripples are significantly reduced by both the DDTC-1 and the proposed 3L-DTC. The zoomed-in torque responses in Fig. 3.13 confirm that the proposed 3L-DTC method does not deteriorate the excellent dynamics of the conventional DTC.

3.6.2 Steady state performance

To have a better understanding of the torque dynamics associated with a three-level inverter fed DTC, and how the proposed 3L-DTC method is efficient in controlling the torque ripples, experiments were carried out at different operating speeds. The motor was applied with a load torque of 3 Nm. The steady state responses corresponding to three different speeds (high, medium and low) are shown in Figs. 3.14-3.16 and subsequently, summarized quantitatively in Fig. 3.17.

For the estimation of average switching frequency, the total commutations of the upper six switches in the 3L-NPC inverter are counted and averaged during a fixed period (50 ms is used in this study). The maximum frequency used for THD calculation is 6.5 kHz. Torque and flux ripples are computed using

$$X_{ripple} = \sqrt{\frac{1}{n}\sum_{k=1}^{n}(X_k - X_{average})^2} \tag{3.20}$$

where $X = \{T_e, \psi_s\}$.

High Speed − The steady state responses of the IPMSM at an operating at a speed of 500 rpm is shown in Fig. 3.14. In this region, the LVVs/MVVs are

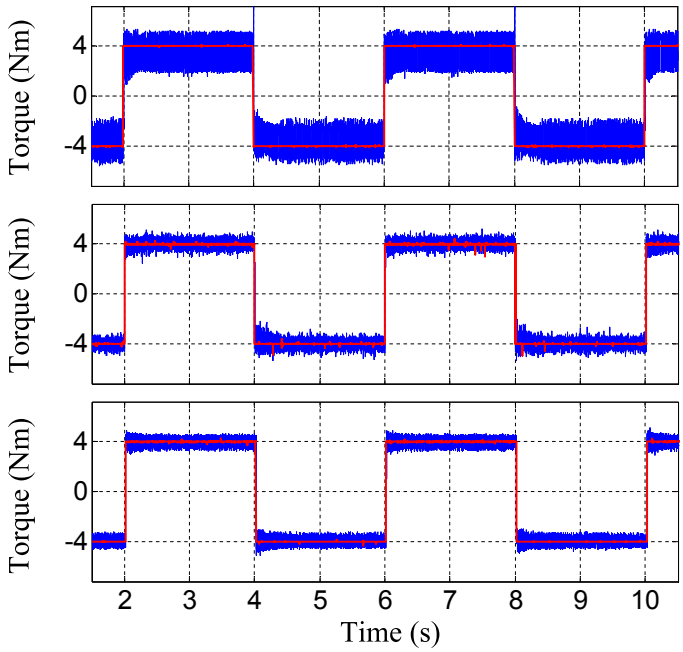

Figure 3.12: Torque reversal at standstill from -4 Nm to 4Nm; classical 3L-DTC (top), DDTC-1 (middle) and the proposed 3L-DTC (bottom).

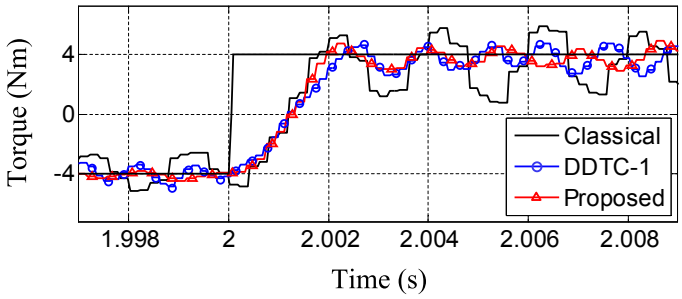

Figure 3.13: Zoomed in torque responses during torque reversal.

frequently used since they are required to overcome the back e.m.f of the motor. Nevertheless, SVVs will still be used. From Fig. 3.3, it can be observed that the torque variation rates of SVVs in this region are near zero or negative. In the proposed 3L-DTC algorithm, a LVV/MVV is applied along with a SVV during most switching cycles. This prevents large torque overshoots, and therefore, torque ripples are reduced as shown in Fig. 3.14(c).

An almost similar degree of torque ripples attenuation is attained by the DDTC-

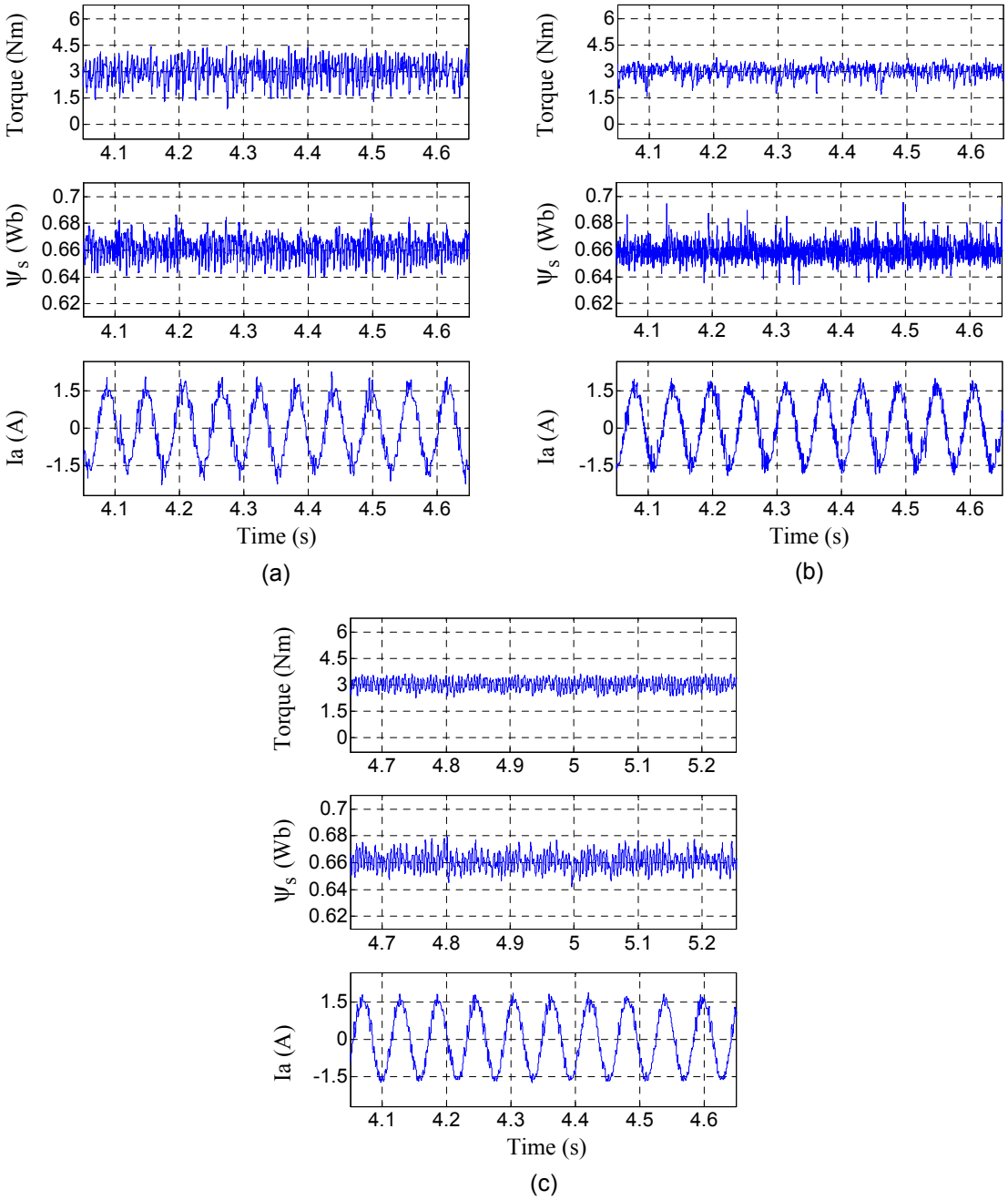

Figure 3.14: Steady state responses of the IPMSM drive at 500 rpm, 3 Nm; (a) Classical 3L-DTC. (b) DDTC-1. (c) Proposed 3L-DTC.

1 method. Nevertheless, it can be observed in Fig. 3.14(b) that the stator flux ripples in DDTC-1 are much higher than the proposed method, and this leads to the higher THD observed in the output current (see Fig. 3.17). Poor regulation of flux in DDTC-1 is not surprising as no consideration is given to smooth voltage

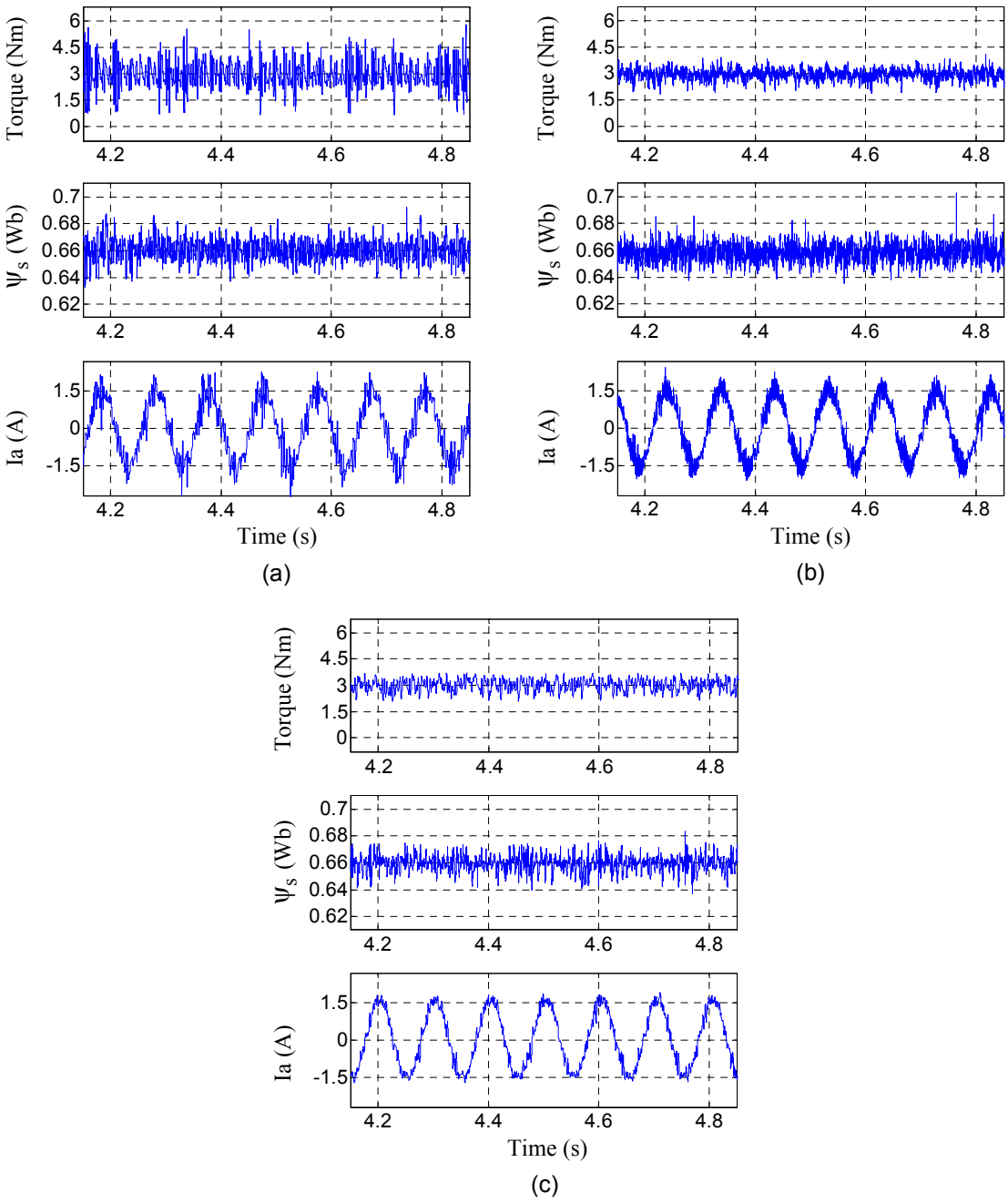

Figure 3.15: Steady state responses of the IPMSM drive at 300 rpm, 3 Nm; (a) Classical 3L-DTC. (b) DDTC-1. (c) Proposed 3L-DTC.

vector switching. Consequently, large voltage jumps will introduce higher low order harmonics in the output current [84].

Medium Speed – Fig. 3.15 shows the steady state responses of the IPMSM when it is operating at a speed of 300 rpm. In this region, both LVVs/MVVs and

SVVs are applied almost equally. The torque variation rates of SVVs are positive. Conversely, LVVs/MVVs have large torque variation rates which cause overshoots of torque in the classical 3L-DTC. These overshoots further prompt the torque hysteresis comparator to output negative hysteresis states, leading to the large torque ripples seen in Fig. 3.15(a).

In contrast, the proposed method controls the torque overshoots by regulating the duty ratios of the voltage vectors. Consequently, the hysteresis comparator output is mostly confined to +2 and +1 states. Torque ripples are also effectively reduced by the DDTC-1 method, as shown in Fig. 3.15(b). In fact, DDTC-1 achieves slightly better torque ripple reduction than the proposed method, which can be attributed to the strict voltage vector switching criteria imposed by the proposed method. By satisfying the switching constraints of the 3L-NPC inverter, improved flux regulation and lower THD is attained by the proposed 3L-DTC drive, as illustrated in Figs. 3.15 and 3.17.

Low Speed − The steady state responses of the IPMSM, operating at the speed of 150 rpm, are depicted in Fig. 3.16. The back e.m.f of the motor is small while the torque variation rates of the LVV/MVVs are approximately twice that of SVVs. Therefore during steady state operations, it is important to minimize the usage of LVV/MVVs to alleviate the torque ripples. With the classical 3L-DTC, this is not feasible, unless a large torque hysteresis band is used. Using a large torque hysteresis band could improve the torque ripples at slow speeds as torque hysteresis comparator output can be confined to +1 and −1 states. However, at higher speed regions, this will lead to steady state torque errors and sluggish drive response.

With the proposed 3L-DTC method, the application of a SVV-ZVV combination in a switching cycle confines the output of hysteresis torque comparator mostly to +1 state. This leads to the significant reduction in torque ripples seen in Fig. 3.16(c), which is even superior to the DDTC-1 method. Moreover, the

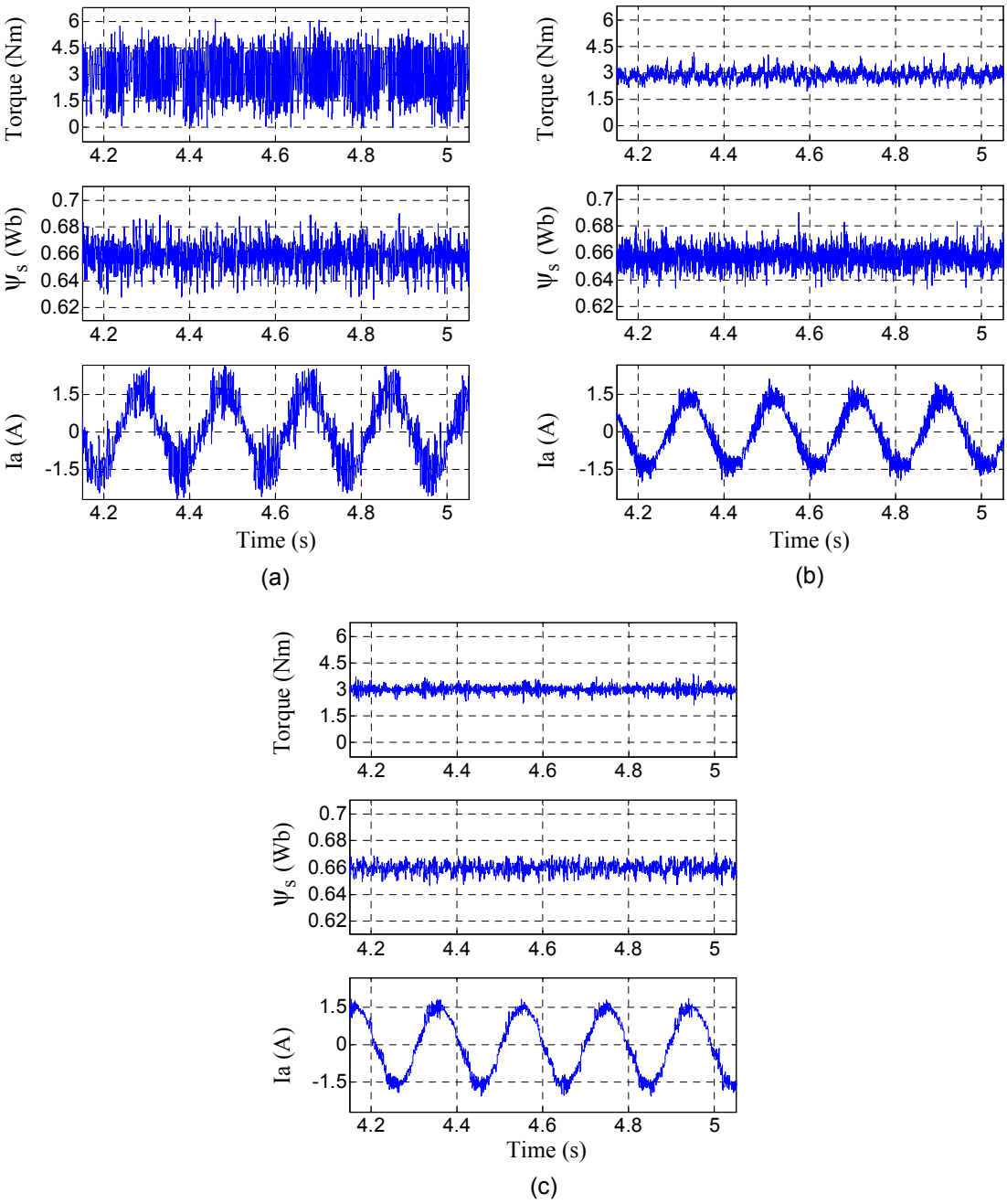

Figure 3.16: Steady state responses of the IPMSM drive at 150 rpm, 3 Nm; (a) Classical 3L-DTC. (b) DDTC-1. (c) Proposed 3L-DTC.

predominant usage of SVVs and ZVVs in the proposed method leads to vast improvements in stator flux regulation and subsequently, the THD of the output current, as shown in Figs. 3.16 and 3.17.

From the quantitative data presented in Fig. 3.17, the average reductions

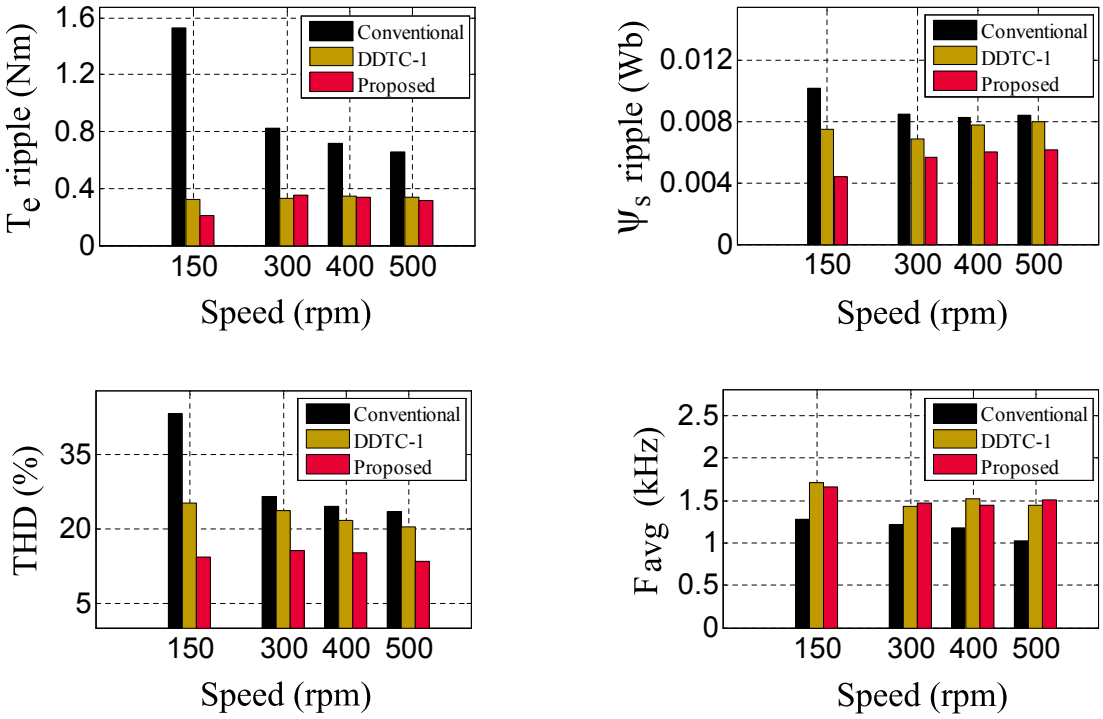

Figure 3.17: Comparison of steady state torque ripple, flux ripple, current THD and the average switching frequency at different operating speeds (load: 3 Nm).

achieved by the proposed 3L-DTC for torque and flux ripples is 67.64% and 35.59%, respectively, when compared to classical 3L-DTC. The highest reduction in torque and flux ripples occurs when the motor is operating at low speeds. At 150 rpm, the reduction in torque and flux ripples is 86.1% and 55.87%, respectively. As flux ripples are reduced, significant improvements are seen in the THD of the stator current.

It is also clearly evident from Figs. 3.14-3.17 that the DDTC-1 method is more or less, equally capable of achieving appreciable torque ripple reduction, as the proposed method. However, it needs to be pointed out that the improvements seen are attained at the cost of poorer flux regulation and THD of the output current.

The classical 3L-DTC has an average switching frequency ranging from 1.28 kHz at 150 rpm to 1.03 kHz at 500 rpm. As expected, the average switching frequency of the DDTC-1 and the proposed method is higher than that of the

classical 3L-DTC. Nevertheless, it is kept well below 2 kHz in the proposed 3L-DTC; the proposed 3L-DTC has an average switching frequency ranging from a high of 1.6 kHz at 150 rpm to a low of 1.46 kHz at 400 rpm. This constitutes an average increment in the average switching frequency of about 1.3 times, which is a small price to pay for the significant improvements seen in the torque and flux dynamics, especially at lower operating speeds.

The line to line and the dc-link capacitor voltages corresponding to high, medium and low speed operations are presented in Fig. 3.18 for the proposed 3L-DTC. It can be observed that smooth voltage vector switching is generally maintained while dc-link capacitor voltages are controlled to be within a band of about ± 5 V.

When comparing the line to line and dc-link capacitor voltages of the proposed 3L-DTC to that of the classical 3L-DTC and DDTC-1, the differences observed are rather insignificant when the IPMSM is operating at high and medium speeds. However, in the lower speed regions, the proposed method is clearly superior. The proposed method uses mostly SVVs and ZVVs at lower speeds, and this is proven by the two-level line to line voltage shown in Fig. 3.18(a). In contrast, LVVs/MVVs are still employed in the classical 3L-DTC and the DDTC-1 methods, resulting in the irregular three-level line to line voltages and the larger dc-link capacitor voltage ripples observed in Fig. 3.19.

3.6.3 Parametric robustness of the proposed method

All the experimental results presented previously in this chapter are attained with the design parameters listed in Table. 3.2, which were first determined using the known machine parameters, and subsequently fine-tuned. Therefore, the parametric robustness of the proposed 3L-DTC method is investigated in this subsection.

Parametric robustness can be thought of how the tuned, 3L-DTC drive will react to variations in known machine parameters. However, to replicate machine

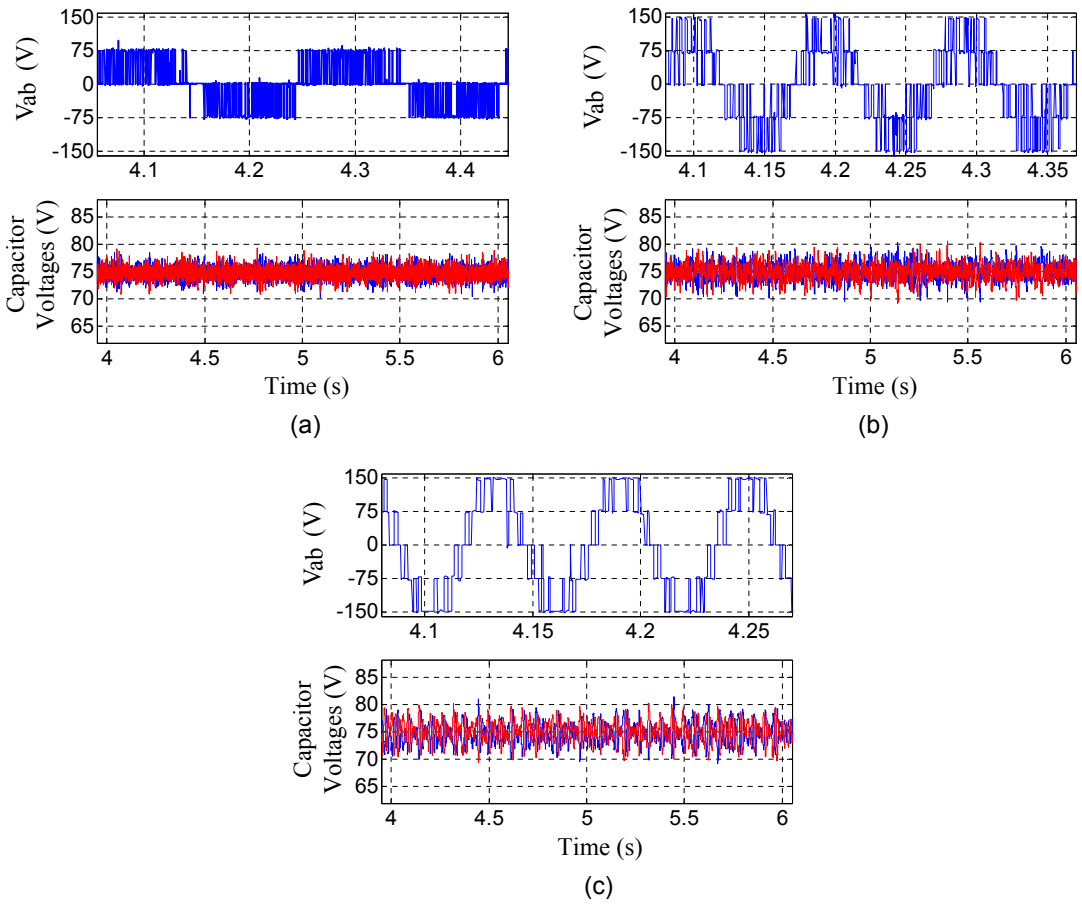

Figure 3.18: Steady state line to line voltages and dc-link capacitor voltages of the proposed 3L-DTC with a load of 3 Nm. (a) 150 rpm, (b) 300 rpm (c) 500 rpm.

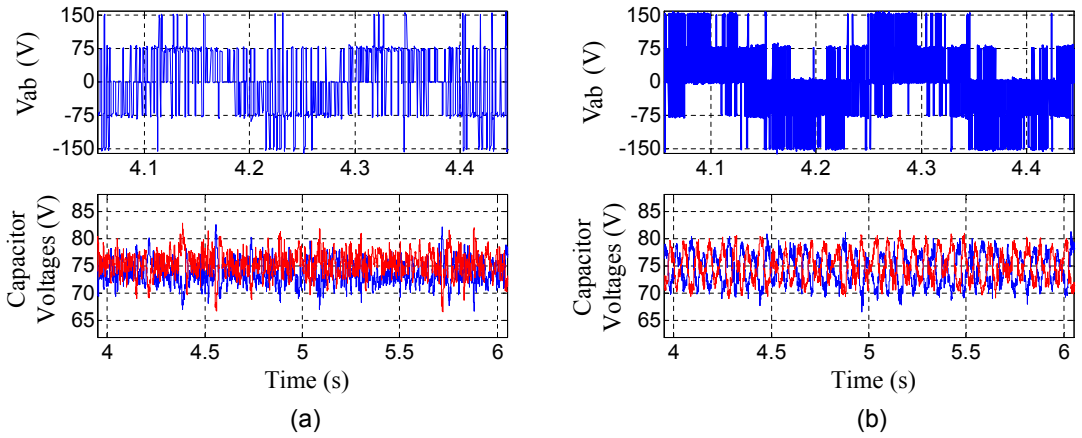

Figure 3.19: Steady state line to line voltage and dc-link capacitor voltages at 150 rpm with a load of 3 Nm. (a) Classical 3L-DTC. (b) DDTC-1 method.

parameter variations in experiments is not easy. One practical way to emulate these variations in experiments is to detune the constants C_1 and C_2 and analyze the sensitivity of the proposed 3L-DTC drives transient and steady state performance. The rationale for investigating parameter robustness through such sensitivity analysis is explained below.

From (2.18), it follows that the torque slope is dependent on the stator resistance R_s, quadrature inductance L_q and the active flux ψ_r. In approximating the generalized torque slope equations for duty ratio calculations, the influence of load torque is not considered since they are comparatively insignificant to that of the operating speed, as explained previously. Consequently, in the design process for robustness analysis, the torque slope can be approximated as

$$\rho T_e \approx -\frac{3P}{2L_q}|\psi_s|\psi_{rx}\omega_{re} + \frac{3P}{2L_q}v_s \otimes \psi_r \tag{3.21}$$

The design parameters C_1 and C_2 are dependent on two variables, s_0 and k which are parameter dependent. s_0 is the approximate torque slope of LVVs at zero speed and varies sinusoidally within a sector (3-18). In other words, the peak value of s_0 would be equal to

$$\widehat{s_0} = \widehat{\nabla} T_e = \frac{3P}{2L_q}v_s \otimes \psi_r \tag{3.22}$$

k is the factor by which torque slope of LVV differs at the rated speed ω_n with respect to the peak torque slope, $\widehat{\nabla} T_e$. Therefore, the range for k can be approximated as

$$\begin{aligned} k = \frac{-\frac{3P}{2L_q}|\psi_s|\psi_{rx}\omega_{re} + \frac{3P}{2L_q}(v_s \otimes \psi_r)}{\frac{3P}{2L_q}(v_s \otimes \psi_r)} &= -\frac{|\psi_s|\psi_{rx}\omega_{re}}{(v_s \otimes \psi_r)} + 1 \\ &\approx -\frac{|\psi_s|\omega_{re}}{v_s}\cos\delta + 1 \end{aligned} \tag{3.23}$$

From (3.22) and (3.23), it follows that the changes in k due to machine parameter variations would be minimal. On the other hand, s_0 is dependent on quadrature inductance, L_q and active flux linkage, ψ_r. Using the peak amplitude

of torque slope as an approximation for s_0, the design parameters C_1 and C_2 can be rewritten as

$$C_1 = \frac{3P}{2L_q}(v_s \otimes \psi_r)T_s \qquad C_2 = \frac{3P(k-1)}{2L_q\omega_n}(v_s \otimes \psi_r)T_s \tag{3.24}$$

From (3.24), two important aspects of machine parameter dependence can be noticed. Firstly, C_1 and C_2 are inversely proportional to L_q. This means that when L_q decreases over time to a new value $\breve{L_q}$, it is analogous to an proportional increment in both C_1 and C_2.

Secondly, C_1 and C_2 are approximately proportional to the active flux ψ_r as $\psi_{rx}v_{sy} >> \psi_{ry}v_{sx}$ in PMSMs during steady state. This assumption is generally true since the slope of stator flux in PMSM is small compared to that of torque slope. Consequently, stator flux can be tightly regulated by setting small hysteresis bands to reduce the THD in the outputs. This means that when ψ_r decrease over time to a new value $\breve{\psi_r}$, it is analogous to a proportinal decrease in both C_1 and C_2.

The analysis above shows that the possible parameter variations of L_q and ψ_r that could occur when the proposed drive is operating with tuned C_1 and C_2, can be emulated by detuning C_1 and C_2. However, two issues needs to be highlighted. Firstly, the parameter C_2 is directly proportional to C_1. However, the dependence is only valid for determining the starting point of C_2 which is then tuned independently. Secondly, as previously discussed in Section 3.4, the impact of increasing or decreasing C_1 and C_2 will produce opposite effects on the duty ratio, although at different rates. This means that the net change seen in the actual duty ratio would be small for realistic detuning of machine parameters.

For L_q, a realistic maximum variation would be around 20% in PMSMs, while for permanent magnet flux linkages, the mismatch should not be higher than $\pm 10-15\%$. Subsequently, sensitivity analysis of C_1 and C_2 are carried out separately with a detuning of 20% in experiments to analyze the parametric robustness of the proposed method.Firstly, C_1 was detuned by -20% to 0.984 at $t = 4$ s (see Fig. 3.20

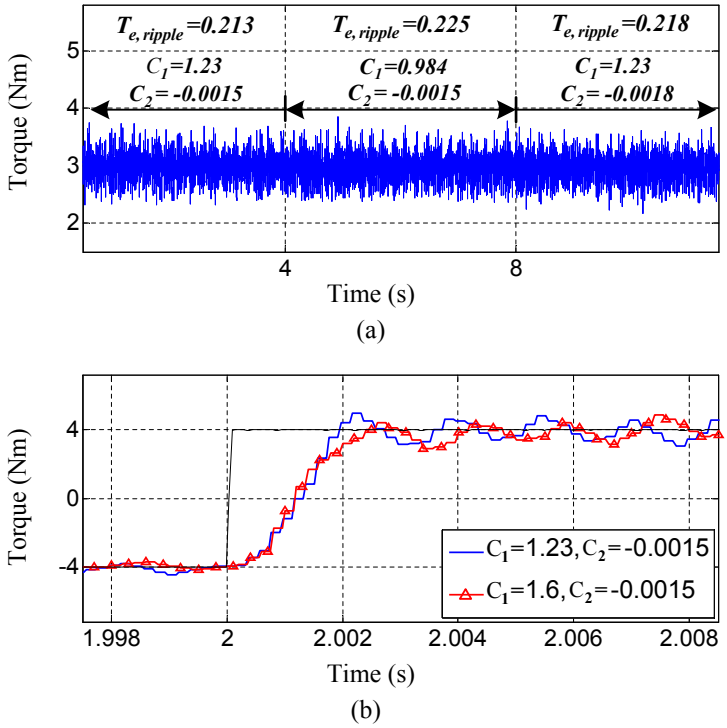

Figure 3.20: Torque responses with detuning of C_1 and C_2. (a) Steady state response. (b) Transient response during torque reversal with detuning of C_1.

(a)) when the motor was operating at 150 rpm with a load of 3 Nm. No significant differences in the torque regulation are seen in Fig. 3.20(a). Nevertheless, torque ripples were found to be increased by about 5.6%, from 0.213 Nm to 0.225 Nm, which concurs with the earlier analysis that a decrement in C_1 will increase the torque ripples. Secondly, C_2 was detuned by +20% ($C_2 = -0.0018$) at $t = 8$ s, while C_1 was restored to the originally tuned value of 1.23. As shown in Fig. 3.20(a), a negligible increment of about 2.4% in torque ripples is noted.

Lastly, the influence of C_1 on the transient torque dynamics is demonstrated through torque reversal experimental results shown in Fig. 3.20(b), where C_1 is increased by +30% ($C_1 = 1.6$). The resulting torque response points to a slightly inferior transient dynamics and negligible reductions in torque ripples, which substantiates the analysis provided in Section 3.4.

The preceding studies show that torque regulation in the proposed 3L-DTC drive is indeed sensitive to variations in the control variables. Nevertheless, the

differences noted in transient and steady state responses are rather inconsequential considering the amount of detuning that was used for the experimental study. Therefore, it can be concluded that the proposed 3L-DTC method, which must be tuned according to the guidelines specified in Section 3.4, is adequately robust against machine parameter mismatch.

3.7 Conclusion

In this chapter, a new duty cycle based DTC method is proposed to improve the performance of a three-level inverter driven IPMSM. The proposed method significantly reduces the torque ripples and improves the flux responses and THD in switching table based 3L-DTC, at the cost of a minimal increase in average switching frequency.

Torque ripple reduction is achieved through the application of more than one voltage vectors per switching cycle. All the available voltage vectors of a 3L-NPC inverter are utilized in the proposed method, with special attention paid to neutral point voltage control and smooth voltage vector switching.

An approximate duty ratio calculation method, based on the instantaneous torque error and the operating speed of the motor is developed. The proposed duty ratio calculation method has a simple structure and uses design parameters that do not rely on the accuracy of machine parameters.

The effectiveness of the proposed 3L-DTC is confirmed by the experiments results and the comparative analysis presented against classical 3L-DTC and a prior art. Results show that the proposed method achieves excellent steady state and transient performances while maintaining the simplicity and robustness of classical DTC.

Chapter 4

Three-Vector Based DDTC Strategy for 3L-DTC of IPMSM

4.1 Motivation and Objectives

For the optimum effect of DDTC strategy, the torque slopes of the active and passive vectors used in each sampling cycle should be of opposite polarity and hence, counteracting to reduce the large excursions of torque. For instance, the zero voltage vector which generally has a torque slope that is opposite to the non-zero vectors are generally used as passive vectors in DDTC strategies for 2L-DTC drives.

In 3L-DTC drives, the use of zero voltage vectors as passive vectors is not possible at all times due to the inverter inherent switching constraints. Switching transitions are usually limited to be between adjacent vectors in 3L-DTC drives; for instance, when either an LVV or an MVV is selected as the active vector for high torque demands in 3L-DTC drives, only an SVV can be used as the passive vector. In comparison to LVV/MVVs, the torque slopes of SVVs are negative at high speeds. Nonetheless, they remain positive during normal and low speeds. This implies that a vector combination of LVV/MVV-SVV will not be as effective for torque ripple reduction as a vector combination involving LVV/MVVs and ZVVs respectively, as active and passive vectors.

The use of ZVVs as passive vectors with LVV/MVVs has been reported for

3L-DTC drives in [91], where up to four voltage vectors are applied in each sampling cycle. Nevertheless, the analytical TR-RMSM approach used for duty ratio calculations is tedious, and its validity is dependent on the accurate knowledge of the machine parameters. Furthermore, inverter switching limitations are not considered in developing the switching table.

As previously discussed in Chapter 2, flux drooping or poor flux regulation is a problem in DTC drives during low speed operations. Flux drooping occurs near sector transitioning regions during low speeds, especially when the motor is heavily loaded. Several solutions are proposed for 2L-DTC drives in the literature; such as using variable switching sectors [101], reverse voltage vectors [102], [103] and dithering techniques [41]. However, these methods are not readily applicable to 3L-DTC drives due to the practical implementation issues discussed in Chapter 2.

For 3L-DTC drives, the method in [91], [93] recommends the use of a modified switching lookup table when the stator flux droops below a minimum fixed level. The proposed method improves stator flux performance. Nevertheless, it uses medium voltage vectors which have the potential to produce large torque ripples due to their high torque slopes at lower speeds. Moreover, switching transitions are allowed between medium voltage vectors for torque ripple reduction, which clearly violates the smooth vector switching criteria.

To resolve the aforementioned problems in 3L-DTC drives, a novel three-vector based DDTC strategy that attains effective torque ripple reduction and improves the low speed performance is proposed in this chapter. The major aspects of the proposed method are: 1) easy implementation and robustness to parameter variations, thus retaining the virtues of the classical DTC.; 2) improved flux and torque regulation during low speed operations using a new switching strategy that requires no additional switching tables; 3) all improvements listed in 1 and 2 are attained by respecting the switching constraints of the 3L-NPC inverter.

The remaining part of this chapter is organized as follows: The proposed switching lookup table for torque ripple reduction is presented in Section 4.2. The

simplified duty ratio calculation method is introduced in Section 4.3 while the guidelines used for the selection of design parameters are explained in Section 4.4. The switching strategies proposed for improving the low speed performance and proper voltage vector sequencing are discussed in Sections 4.5 and 4.6, respectively. Experimental results are presented in Section. 4.7 to compare and evaluate the effectiveness of the proposed method against that of classical 3L-DTC and two existing DDTC methods for 3L-DTC drives in [90] and [91], [93].

4.2 Switching Lookup Table

The lookup table for the proposed drive is developed based on four-level ($\epsilon_T = \pm 2, \pm 1$) torque and two-level ($\epsilon_{psi} = \pm 1$) flux hysteresis control and a sector division of twelve (S_{1a}, S_{1b}, S_{2a}, ..., S_{6b}), identical to the proposed two-vector based DDTC method in Chapter 3. The resultant switching lookup table is presented in Table. 4.1, where the main voltage vector to be applied in a switching cycle is termed 'active' while the nonactive one/s is/are termed 'passive'.

For high torque demands ($\epsilon = \pm 2$), either an LVV or an MVV is selected as the active vector and therefore, the inverter switching constraints will limit the selection of passive vector to adjacent SVV vectors. However, the selection of an SVV as the sole passive vector will not be adequate for effective torque ripple reduction under all operating conditions, as demonstrated by the approximate peak torque characteristics of different voltage vectors in Fig. 4.1.

It can be observed in Fig. 4.1 that the peak torque slope of the SVV is negative at high speeds, but remains positive during normal and low speeds. Therefore, the combination of LVV/MVV-SVV only contributes to attenuate torque ripples effectively at high speeds. On the contrary, torque ripples can be significantly reduced at normal and low speeds if ZVVs are used as passive vectors. However, the direct transition from LVV/MVVs to ZVVs is prohibited by the smooth vector switching criteria.

Table 4.1: Switching Table For The Proposed 3L-DTC Drive

Flux ε_ψ		+1				-1			
Torque ε_T		-2	-1	+1	+2	-2	-1	+1	+2
Sector Ska	v_{active}	v_{Mk-2}	v_{Sk-1}	v_{Sk+1}	v_{Lk+1}	v_{Lk-2}	v_{Sk-2}	v_{Sk+2}	v_{Mk+1}
	$v_{passive}$	v_{Sk-1}, v_Z	v_Z	v_Z	v_{Sk+1}, v_Z	v_{Sk-2}, v_Z	v_Z	v_Z	v_{Sk+2}, v_Z
Skb	v_{active}	v_{Lk-1}	v_{Sk-1}	v_{Sk+1}	v_{Mk+1}	v_{Mk-2}	v_{Sk-2}	v_{Sk+2}	v_{Lk+2}
	$v_{passive}$	v_{Sk-1}, v_Z	v_Z	v_Z	v_{Sk+1}, v_Z	v_{Sk-2}, v_Z	v_Z	v_Z	v_{Sk+2}, v_Z

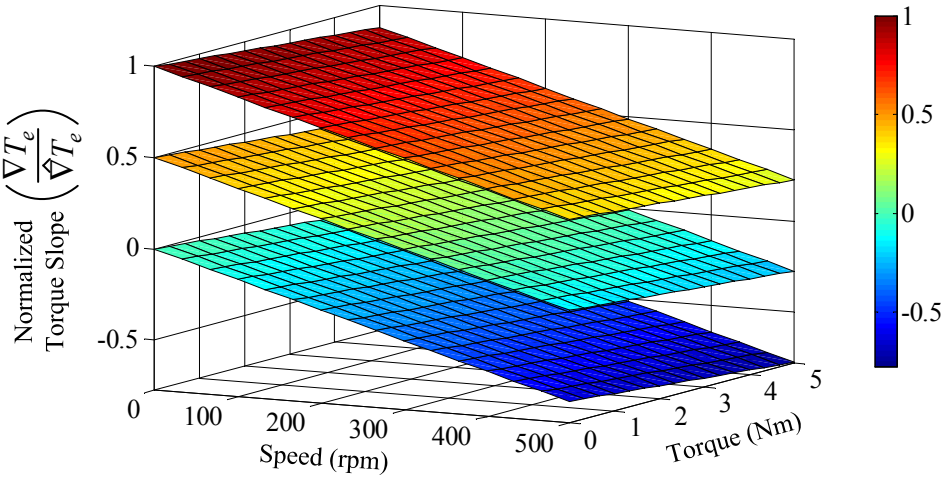

Figure 4.1: Normalized peak torque slope characterization of LVV (upper surface), SVV (middle surface) and ZVV (lower surface).

To resolve such problems, the DDTC strategy proposed in this chapter uses the vector combination of LVV/MVV-SVV-ZVV during high torque demand, as shown in Table 4.1. In other words, an active vector and two passive vectors, an SVV that is adjacent to the selected active vector and a ZVV, are applied sequentially within each sampling cycle during high torque demand. For instance, in sector S_{1a}, if torque ($\epsilon_T = +2$) and flux ($\epsilon_\psi = +1$) demands are high and positive, the chosen vector combination would be $v_{L2} - v_{S2} - v_Z$.

When the torque demand is low ($\epsilon_T = \pm 1$), SVVs are selected as active vectors. From Fig. 4.1, it can be noticed that ZVVs have negative torque slopes even at

very low speeds, which are sufficient to counteract the small positive slopes of SVVs. Consequently, SVVs and ZVVs are used respectively as active and passive vectors, as illustrated in Table 4.1.

4.3 Duty Ratio Calculation

Since multiple vectors are chosen by the switching lookup table, the sampling period T_s has to be divided appropriately into several intervals to attenuate the torque ripples. For high torque demands ($\epsilon_T = \pm 2$), the expected torque ripple profile would be as shown in Fig. 4.2(a), where D_{act}, D_{pas}^1 and D_{pas}^2 represent respectively, the duty ratios of the active vector (LVV/MVV), the first (SVV) and second (ZVV) passive vector in one sampling period.

The duty ratios in Fig. 4.2(a) can be determined using the TR-RMSM approach in [91]. However, the direct application of this TR-RMSM method would lead to complicated and lengthy solutions, as seen in [91]. In view of this, a simplified duty ratio calculation method is developed through the usage of a virtual voltage vector (VVV) that is synthesized from the combination of SVV-ZVV (see Fig. 4.2(b)). The synthesized vector can be expressed as

$$VVV = m * SVV + (1 - m)ZVV \tag{4.1}$$

where m denotes the modulation index of the SVV within the switching time allocated for the VVV, $D_{pas}T_s$. Subsequently, if the value of m is known, the duty ratios in Fig. 4.2(b) can be easily calculated by applying the well-established TR-RMSM method in (3.2) with s_1 and s_2 representing the torque slopes of active and passive (VVV) vectors, respectively.

When SVV-ZVV combinations are used during low torque demands ($\epsilon_T = \pm 1$), the expected torque ripples would have the same profile as those produced by LVV/MVV-VVV in Fig. 4.2(b). Therefore, (3-2) can also be used for determining D_{act}, in this instance, the duty ratio of the active vector, SVV.

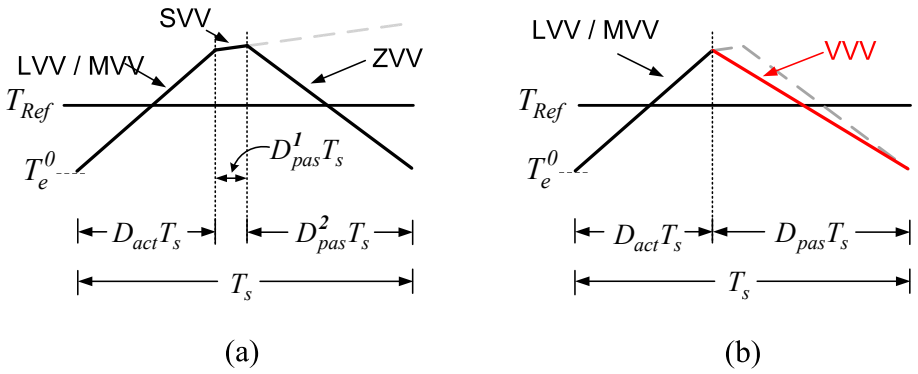

Figure 4.2: Typical torque ripple profiles in one switching cycle during normal speed operations. (a) Using the vector combination of LVV/MVV-SVV-ZVV. (b) Using the combination of LVV/MVV-VVV.

Conventionally, slopes s_1 and s_2, are estimated from (2.18), thus yielding a machine parameter dependent D_{act}. In order to improve the parameter robustness of the proposed 3L-DTC method, generalized equations for slopes s_1 and s_2 are developed considering the instantaneous torque error and the operating speed of the motor.

From the discussion on torque slope characteristics of IPMSM drive in Chapter 3, two important aspects are clear. Firstly, the torque slope of voltage vectors decreases proportionally as the machine speed increases at constant load torque. Secondly, in comparison to the operating speed, the influence of load torque on torque slope is negligible. These characteristics are also evident in Fig. 4.1.

Therefore, the effect of instantaneous changes in load torque is not considered for the torque slope calculations. The generalized slope equations for the vector combinations of LVV-VVV, MVV-VVV and SVV-ZVV are derived in the following subsections and subsequently, substituted into (3.2) to obtain the duty ratios of the active vectors D_{act}, in Table 4.2.

4.3.1 LVV-VVV

For high, increasing torque demand $\epsilon_T = +2$, the torque slope of the active vector (LVV) at zero speed (s_L^0) and the rated speed (s_L^n) can be approximated as

$$s_L^0 = s_0 \qquad\qquad s_L^n = ks_0 \tag{4.2}$$

where k is the factor by which torque slope of LVV differs at the rated speed ω_n with respect to the slope at zero speed s_0.

The selected LVV and SVV are always spatially aligned in the $\alpha - \beta$ the plane and thus, maintain a constant torque slope ratio. Consequently, the torque slopes of the passive vectors SVV and ZVV, at zero speed and the rated speed can be expressed as

$$s_{SL}^0 = 0.5s_0 \qquad\qquad s_{SL}^n = (k - 0.5)s_0 + 0.5s_0 \tag{4.3}$$

$$s_Z^0 = 0 \qquad\qquad s_Z^n = (k - 1)s_0 \tag{4.4}$$

From (4-2)-(4-4), the generalized torque slope equations for LVV (s_L^+), SVV (s_{SL}^+) and ZVV (s_Z^+) can be obtained as

$$s_L^+ = s_0[1 + (k - 1)R_\omega] \tag{4.5}$$

$$s_{SL}^+ = s_0[0.5 + (k - 1)R_\omega] \tag{4.6}$$

$$s_Z^+ = s_0(k - 1)R_\omega \tag{4.7}$$

where R_ω denotes the ratio of actual rotor speed ω_r to the rated speed ω_n. By combining (4.6) and (4.7), the generalized torque slope equation of the VVV can be expressed as

$$s_{VVL}^+ = s_0[0.5m + (k - 1)R_\omega] \tag{4.8}$$

By substituting (4.5) and (4.8) into (3.2) as s_1 and s_2, respectively, the duty ratio of LVV for increasing $\epsilon_T = +2$ and decreasing $\epsilon_T = -2$ torque demands, can be derived as tabulated in Table 4.2. Note that two design parameters, C_1 and C_2,

are introduced in Table 4.2 to minimize the parametric dependence of the proposed method. The criteria used for the initial selection, and the subsequent fine-tuning of C_1 and C_2 are described in Section 4.4.

4.3.2 MVV-VVV

In Chapter 3, it is discussed in detail how the torque slope ratio of an SVV to an adjacent MVV varies from 0.5 to 0.33 in a sector. Accordingly, the highest ratio of 0.5 is used as the reference point to ensure that the duty cycle of the MVV is always sufficient in a sector. Using the same approach, the generalized torque slope equations for MVVs (s_M^+) and SVVs (s_{SM}^+) are derived as

$$s_M^+ = s_0[\sqrt{3}/2 + (k-1)R_\omega] \tag{4.9}$$

$$s_{SM}^+ = s_0[\sqrt{3}/4 + (k-1)R_\omega] \tag{4.10}$$

From (4.7) and (4.10), the generalized torque slope equation of the VVV for this vector combination can be obtained as

$$s_{VVM}^+ = s_0[m\sqrt{3}/4 + (k-1)R_\omega] \tag{4.11}$$

Then, by substituting (4.9) and (4.11) into (3.2), the duty ratio of the active vector, MVV can be derived as shown in Table 4.2.

4.3.3 SVV-ZVV

The generalized torque slope equations in (4.6) and (4.7) respectively, for SVVs and ZVVs are valid when the vector combinations of SVV-ZVVs are used during low torque demands ($\epsilon_T = \pm 1$). Substituting (4.6) and (4.7) into (3.2) as s_1 and s_2, respectively, the duty ratio of the active vector, SVV can be obtained as illustrated in Table 4.2.

Table 4.2: Duty ratio of the active vector, D_{act}

Vector Combination	Increasing Torque Demand, $\varepsilon_T = \{+2,+1\}$	Decreasing Torque Demand, $\varepsilon_T = \{-2,-1\}$
LVV-VVV	$\frac{2\left(T_e^* - T_e^o\right) - 0.5C_1 m - C_2\omega_r}{C_1\left(2 - 0.5m\right) + C_2\omega_r}$	$\frac{2\left(T_e^* - T_e^o\right) - 0.5C_1 m - C_2\omega_r}{-C_1\left(2 - 0.5m\right) + C_2\omega_r}$
MVV-VVV	$\frac{2\left(T_e^* - T_e^o\right) - \sqrt{3}/4\, C_1 m - C_2\omega_r}{C_1\left(2 - \sqrt{3}/4\, m\right) + C_2\omega_r}$	$\frac{2\left(T_e^* - T_e^o\right) - \sqrt{3}/4\, C_1 m - C_2\omega_r}{-C_1\left(2 - \sqrt{3}/4\, m\right) + C_2\omega_r}$
SVV-ZVV	$\frac{2\left(T_e^* - T_e^o\right) - C_2\omega_r}{C_1 + C_2\omega_r}$	$\frac{2\left(T_e^* - T_e^o\right) - C_2\omega_r}{-C_1 + C_2\omega_r}$

where $C_1 = s_o T_s,\ C_2 = C_1\left(k-1\right)/\omega_n$

4.3.4 Modulation index m

To minimize the torque ripples effectively, the modulation index m must be regulated so that ideally, the slope of the VVVs is sufficiently large and opposite to that of the active vector. Consequently, m is varied according to the operating speed as shown in Table 4.3.

During low speeds, it can be observed from Fig. 4.1 that the SVVs have positive torque slopes. On the contrary, the torque slopes of ZVVs are small and negative. Therefore, m is designed to be small so that VVVs will have adequate negative torque slope to counteract the large positive torque slopes of the LVV/MVVs. Considering the smooth voltage vector switching criteria, and the dead-time of $3\mu s$ used for the 3L-NPC inverter in experiments, m is fixed to be 0.1.

As the motor speed increases, LVV/MVVs will be used more frequently as active vectors to overcome the increasing back e.m.f of the motor. From Fig. 4.1 and (2.18), it follows that the slope of SVVs will be small and becomes negative around half the rated speed. At the same time, ZVVs will have large and negative torque slopes. Therefore, m is regulated proportionally with the operating speed up to the high speed region ($\omega_r > 0.9\omega_n$).

In the high speed regions, the negative torque slopes of SVVs are sufficient to

Table 4.3: Modulation index, m

Operating Speed, ω_r	m
$\omega_r \leq 0.9\omega_n$	$\max\left[\frac{(2\omega_r - \omega_n)}{\omega_n}, 0.1\right]$
$\omega_r > 0.9\omega_n$	1.0

counteract the slopes of LVV/MVVs. In addition, the duty ratios of LVV/MMVs will be high, and therefore, the switching time allocated for ZVVs in a sampling cycle would be very small. Consequently, m is set to 1.0 in this speed range. As SVVs are used as the sole passive vector, the average switching frequency of the inverter would be reduced.

4.4 Design Guidelines of Parameters C_1 and C_2

The methodology used for the initial approximation of design parameters in the proposed two-vector based DDTC method in Chapter 3 is also applicable to the three-vector based DDTC presented in this chapter. Once the initial values of C_1 and C_2 has been approximated using (3.17)-(3.19), they have to be tuned to optimize the torque ripple reduction and minimize the vulnerability to the possible mismatches or variations in the known machine parameters.

By comparing the duty ratios in Tables 3.2 and 4.2, it can be observed that the duty ratio of the active vector for the vector combination of SVV-ZVV for both two-vector and three-vector DDTC methods are identical. Conversely, the duty ratio of the active vector in vector combination involving LVVs and MVVs are understandably different due to the use of additional passive vector in the three-vector based DDTC.

Therefore it is important to examine the influence of C_1 and C_2 on the duty ratios of LVV/MVVs. This can be effectuated by plotting the characteristics of duty ratios formulated in Table 4.2. For instance, the duty ratio characterization

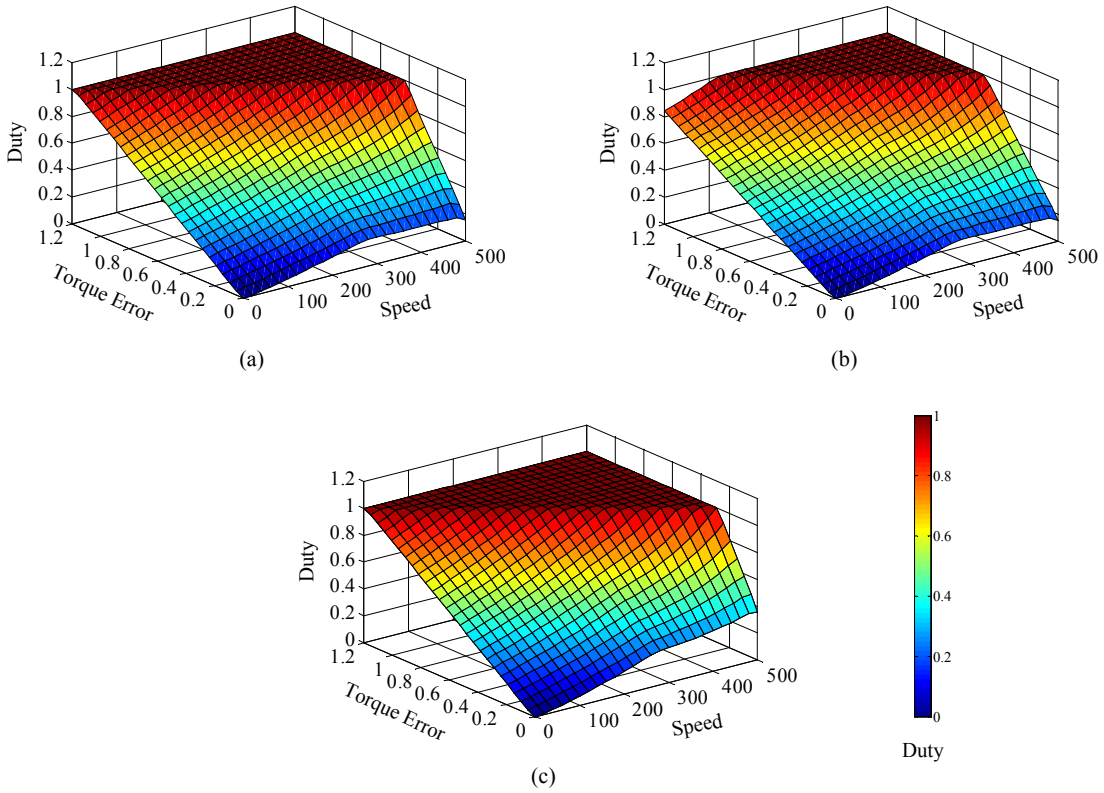

Figure 4.3: Duty cycle characteristics using the proposed method for LVV-VVV (a) $C_1 = 1.18, C_2 = -0.0015$. (b) With 20% increase in C_1. (c) With 20% increase in C_2.

of the LVV-VVV combination, by using the tuned design constants tabulated in Table 4.4, is shown in Fig. 4.3(a). The effects of using zero voltage vectors as the passive vector can be observed in Fig. 4.3, as the LVVs are regulated for the entire speed range. This is because the torque slopes of ZVVs are sufficient to counteract against the large excursions of torque ripple caused by LVVs even at low speeds.

By comparing Fig. 4.3(a) and Fig. 4.3(b), it can be observed that the instances where the active vector is used as the sole vector during a sampling cycle will be reduced with increased C_1. This indicates that increasing C_1 will intensify the duty cycle control. Consequently, as the usage of passive vectors is increased, torque ripple reduction will be higher. Nevertheless, it should be noted that significant increment of C_1 can lead to poor transient torque dynamics.

In contrast, increasing C_2 as shown in Fig. 4.3(c), will lead to the decreased usage of passive vectors, especially at higher speeds. As a result, higher torque ripples will be produced. At the same time, attentions should be given to the amount of reduction in C_2 because the excessive usage of passive vectors at high speeds can lead to undershoots of torque, and subsequently, sluggish drive response.

Once well adjusted, C_1 and C_2 can be considered as independent design constants to be used for duty ratio calculations under all operating condition.

4.5 Low Speed Performance Improvement

Virtual short voltage vectors (VSVV), as shown in Fig. 4.4, are proposed to mitigate the flux drooping problem. The VSVVs are synthesized by applying the two adjacent vectors equally during the time interval of an SVV. For instance, v_{VS1} in Fig. 4.4 can be synthesized by the equal application of SVVs, v_{S1} and v_{S2}.

In the proposed method, VSVVs are used only when the stator flux drooping exceeds the fixed flux drooping tolerance level $\Delta\psi_{dm}$. The magnitude of flux error $|\psi_s|^{err}$ is considered in the voltage vector selection process as shown in the detailed block diagram of the proposed method in Fig. 4.5, and only if $|\psi_s|^{err} > \Delta\psi_{dm}$, VSVVs are used.

For instance, assuming that the torque demand is low and positive ($\epsilon_T = +1$), flux drooping could occur when v_{S2} is selected as the active vector for an increase in flux ($\epsilon_\psi = +1$) just after the stator flux vector has transitioned into sector S_{1a} from S_{6b}. If $|\psi_s|^{err} > \Delta\psi_{dm}$, then the VSVV v_{VS1} would be applied instead of v_{S2} until the stator flux recovers.

It has to be noted that when VSVVs are used, one additional switching transition in each switching cycle is necessary (e.g., for $v_{VS1} - v_z$ combination, $100 - 110 - 111$). However, the increment in average switching frequency is still an improvement compared to the proposed method in [91], [93] where switching transitions are allowed between MVVs in one switching cycle (e.g., 01-1 − 1-10).

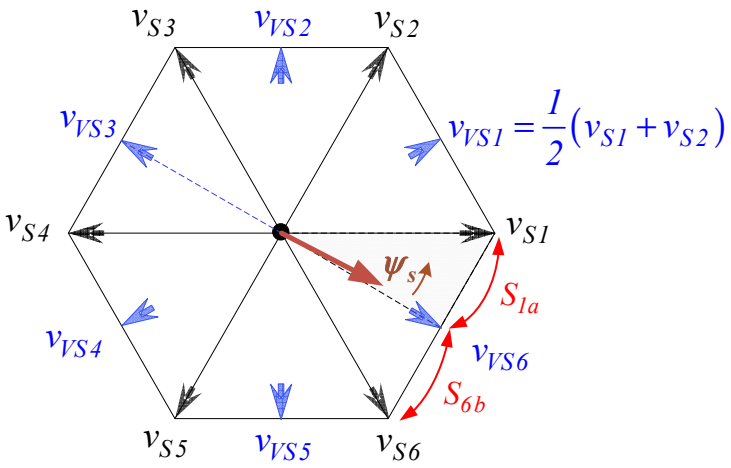

Figure 4.4: The inner hexagon of the vector space with synthesized vectors, $v_{VS,1-6}$.

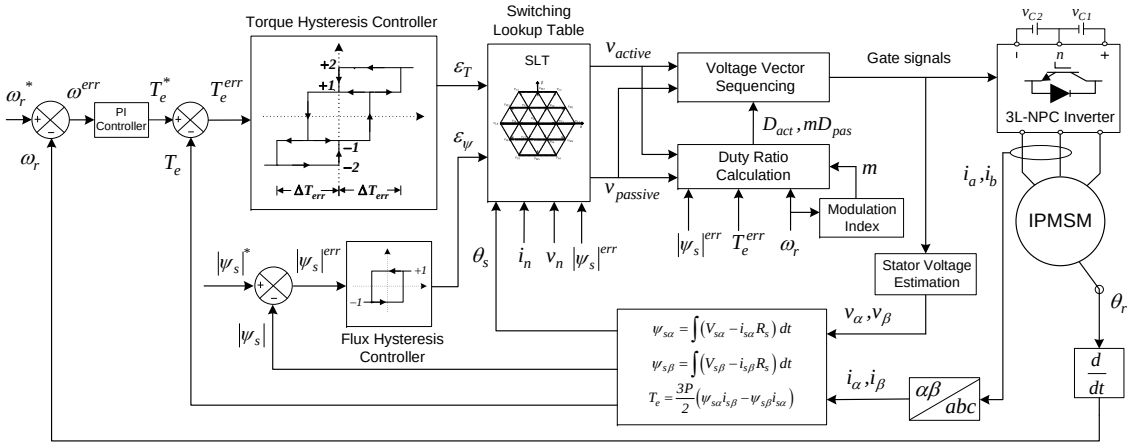

Figure 4.5: Block diagram of the proposed three-vector based 3L-DTC method.

4.6 Voltage Vector Sequencing

The smooth voltage vector switching criteria limits the switching transitions in 3L-NPC inverter to be between adjacent voltage vectors. Therefore, a saw tooth comparator based approach as shown Fig. 4.6 is used for the practical implementation of the proposed 3L-DTC drive. Figs. 4.6(a) and 4.6(b) respectively show the switching sequences and the expected torque profiles within a sampling cycle during high and low torque demands.

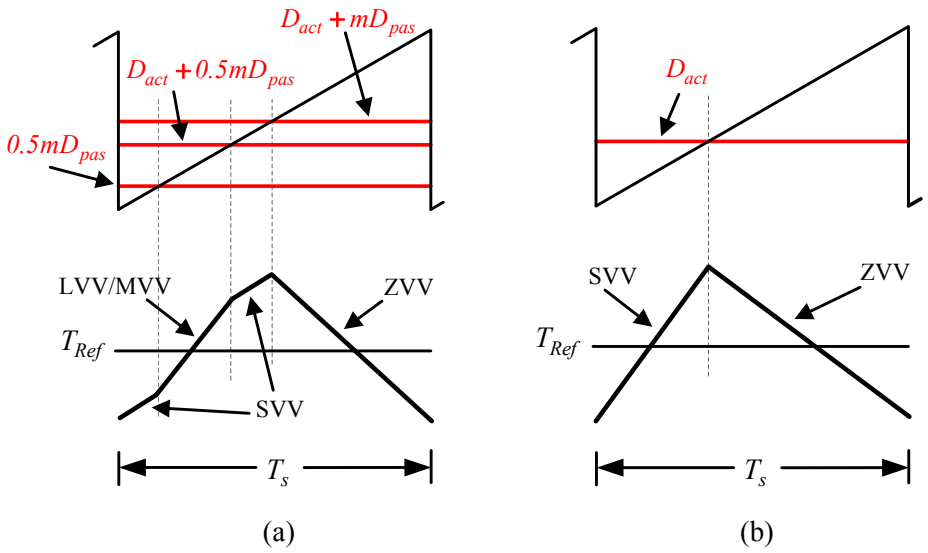

Figure 4.6: Carrier based approach used in the proposed 3L-DTC during (a) High torque demands ($\epsilon_T = \pm 2$). (b) Low torque demands ($\epsilon_T = \pm 1$).

Smooth vector switching is attained through the placement of: 1) SVVs at the beginning of the sampling cycle; 2) ZVVs at the end of the sampling cycle. In order to facilitate this requisite during high torque demands ($\epsilon_T = \pm 2$), it can be noticed in Fig. 4.6(a) that the SVV is switched twice within a sampling cycle. Needless to say, this increases the switching frequency of the inverter; however, this is ensures that any of the SVV can be switched at the start of next switching period.

In some instances, the switching transitions other than those depicted in Fig. 4.6 could still occur in the proposed drive. For example, during high speeds ($\omega_r > 0.9\omega_n$) as m is fixed to 1, the vector combination applied would be LVV/MVV-SVV, i.e., ZVV is not placed at the end of the sampling cycle. Nevertheless, with large back e.m.f to overcome at high speeds, the vast majority of switching transitions at steady state will be due to the change in flux hysteresis controller output. Therefore, smooth voltage vector switching is generally followed as the voltage vectors selected purely for flux regulation in Table 4.1 are all adjacent. Additionally, if switching transitions between non-adjacent vectors are prompted by the hysteresis control, an intermediate voltage vector combination will be applied to

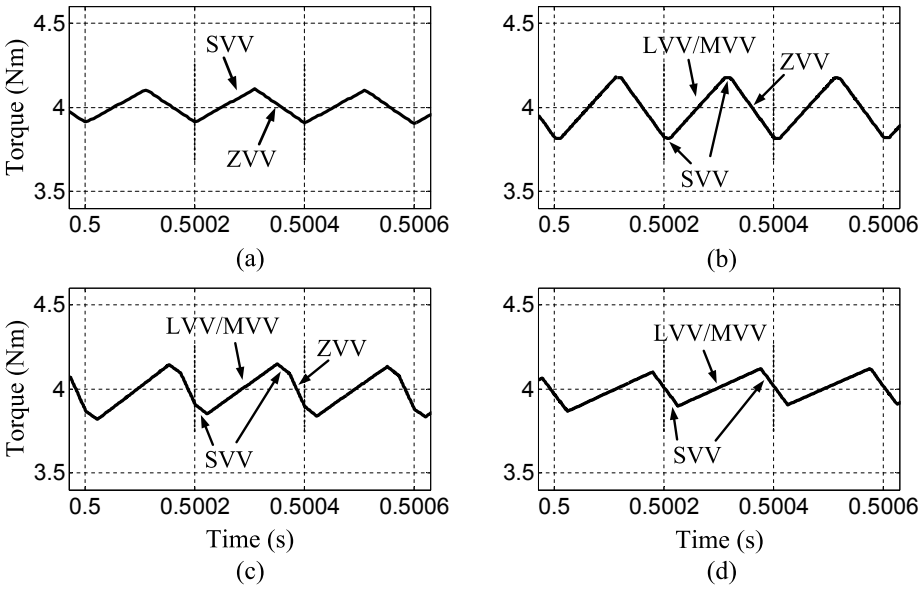

Figure 4.7: Simulation results showing steady state torque ripples in a sampling cycle. (a) 100 rpm. (b) 275 rpm. (c) 400 rpm. (d) 475 rpm.

ensure smooth voltage vector switching.

To illustrate the smooth voltage vector switching and the resultant torque ripple characteristics within each sampling cycle, the results of simulations carried out using Matlab/Simulink are presented in Fig. 4.7. Torque ripple profile during low ($0.2\omega_n$), normal ($0.55\omega_n, 0.8\omega_n$) and high ($0.95\omega_n$) speeds are shown to demonstrate the application of different voltage vectors combinations during these speeds.

The balancing of neutral point voltage v_n is also taken into consideration when selecting the SVVs, as shown in Fig. 4.5. The well-established technique of using the redundancy of the SVVs is employed to minimize the fluctuations of v_n. When SVVs are selected either as active or passive vectors, based on the polarity of v_n and the neutral point current i_n, the SVV that will move the v_n in the direction opposite to the direction of unbalance is selected.

4.7 Experimental Results

In this section, the effectiveness of the proposed 3L-DTC method is experimentally verified using the laboratory prototype illustrated in Fig. 3.11. The perfor-

mance of the proposed 3L-DTC method is compared with a classical 3L-DTC setup and the two other DDTC methods that are referred to simply as DDTC-1 [90] and DDTC-2 [91], [93] in the continuation of this chapter.

The classical 3L-DTC setup uses the same hysteresis control as the proposed 3L-DTC, but only the active vectors of the switching lookup table in Table 4.1 are applied during a sampling period. To make a fair comparative analysis considering the average switching frequencies of the inverter, the sampling frequency of the classical 3L-DTC and DDTC-1 is set to 10 kHz and 7.75 kHz, respectively. Conversely, for DDTC-2 and the proposed method, both of which employ up to three voltage vectors in one switching cycle, a sampling frequency of 5 kHz is used.

In experiments, the hysteresis band, $\epsilon_T = \pm 2$ of the torque controller is set to ± 0.6 Nm (12% of the rated torque), while a band of ± 0.3 Nm is used for the $\epsilon_T = \pm 1$ level. The tuned design constants and the flux drooping tolerance level ($\Delta\psi_{dm}$) used for the proposed 3L-DTC in experiments are tabulated in Table 4.4.

4.7.1 Transient performance

It is important to analyze the transient behavior because, as discussed in the previous section, excessive duty cycle regulation in the proposed method can affect the fast dynamics of DTC. The transient response of the proposed 3L-DTC is compared with the classical 3L-DTC in Fig. 4.8, during a torque reversal from -4 Nm to 4 Nm. The results show that, with well-adjusted control variables, the torque ripples can be reduced without affecting the dynamic torque response.

4.7.2 Steady state performance

Experiments were carried out for all four 3L-DTC approaches at various operating speeds with a load of 3.5 Nm to evaluate the steady state performance of the proposed method. The steady state torque response and the stator current corresponding to high and medium speeds are presented in Figs. 4.9 and 4.10, respectively. The full sets of experimental results are quantitatively summarized

Table 4.4: Optimized design parameters

C_1	1.23	C_2	- 0.0015	$\Delta\psi_{dm}$	0.0133

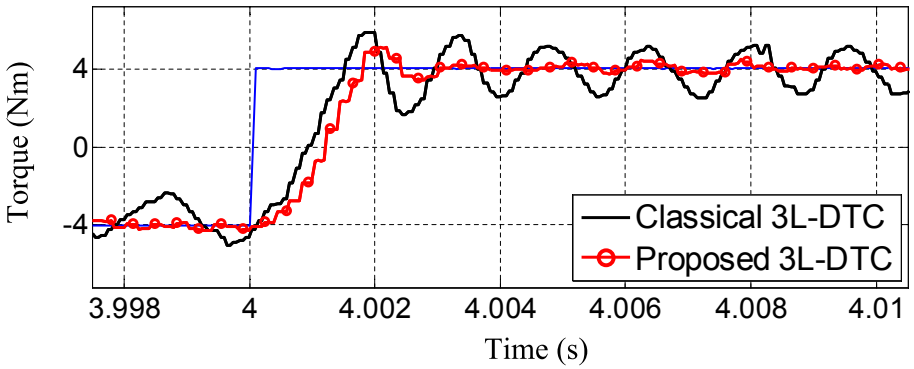

Figure 4.8: Zoomed in torque responses during torque reversal.

in Fig. 4.11. Torque ripples are computed using (3-20). For THD calculations, the maximum frequency used is 5.5 kHz.

The average switching frequency is calculated by counting the number of switching commutations for the upper six switches in the 3L-NPC inverter and averaging for a fixed period (50 ms is used in this study). By using different sampling frequencies, all four 3L-DTC methods operate with similar average switching frequencies, as shown in Fig. 4.11.

In the high to medium speed ranges, it can be observed from Figs. 4.9-4.11 that the average reduction in torque ripples with the proposed 3L-DTC is about 37.1%, when compared to the classical 3L-DTC. The experimental results also show that the proposed method does not offer significantly higher torque ripple reduction than the existing DDTC methods in DDTC-1 and DDTC-2. This is understandable as LVV/MVVs are commonly used as active vectors in all three DDTC methods. The major contribution of the proposed method during this speed range, with regards to motor performance, is that the THD of the output current is reduced (see Fig. 4.11).

It is well recognized that the THD in the stator current is heavily influenced

by the ripples in stator flux [35]. In DDTC-1, the focus is solely on torque ripple reduction; voltage vectors are applied purely based on their instantaneous torque variation rate. Consequently, flux regulation deteriorates, and the THD of the stator current is almost similar to the classical 3L-DTC, which is also observable in the results presented in [90].

On the contrary, the poor flux regulation and high THD in DDTC-2 can be attributed to the switching lookup table used. It should be noted that MVVs are not used in DDTC-2 during normal operating speeds. Only the six LVVs in the outer hexagon of the voltage vector space (see Fig. 3.1) are used as active vectors, and this means that: 1) the output voltages and currents would contain larger THD; 2) the flux regulation would be poor near the sector transitioning regions due to flux drooping, even in the high speed regions. In addition, smooth vector switching criteria is not followed in both DDTC-1 and DDTC-2, and this introduces large voltage jumps and subsequently, higher low order harmonics in the outputs.

During low speed ranges, as evidenced by the results presented for 100 rpm and 15 rpm in Figs 4.11 and 4.12, the proposed 3L-DTC method attains the highest reduction in both torque ripples and THD. The torque slopes of the LVV/MVVs during low speeds are significantly larger than that is required to satisfy the low back e.m.f of the machine. Therefore, the application of LVV/MVVs has to be minimized during low speed steady state conditions to improve the torque regulation in the machine.

With DDTC-1 and DDTC-2 methods, this is clearly not possible according to the switching lookup tables used in [90] and [91]. Of course, large torque hysteresis bands can be used to limit the usage of voltage vectors to mainly SVVs in classical 3L-DTC. However, this will lead to large torque errors during high speeds and consequently, sluggish drive response.

With the proposed method, an SVV-ZVV combination is applied during most switching cycles which confine the torque hysteresis controller typically to the low

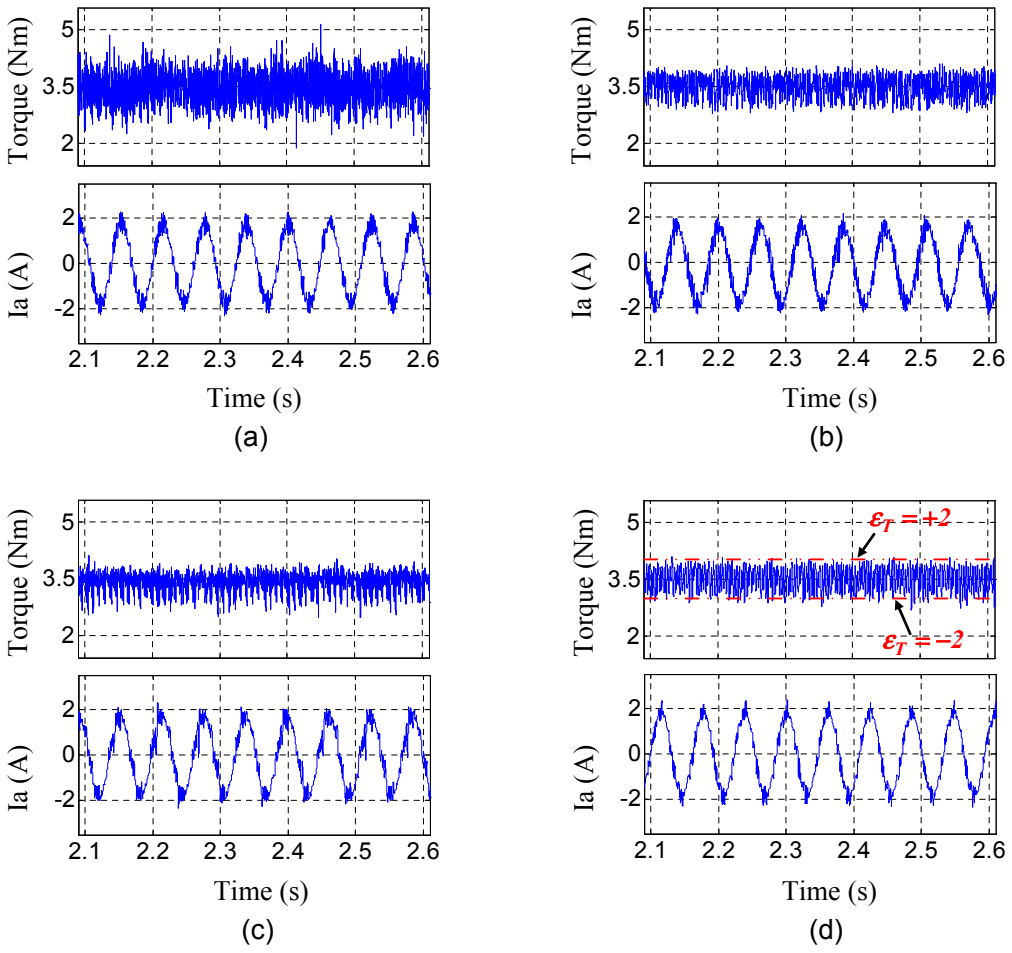

Figure 4.9: Steady state responses of the IPMSM drive at 475 rpm, 3.5 Nm; (a) Conventional 3L-DTC. (b) DDTC-1. (c) DDTC-2. (d) Proposed 3L-DTC.

hysteresis states, $\epsilon_T = \pm 1$. The increased usage of SVVs as active vectors leads to improved torque regulation and THD seen in Fig 4.11.

To summarize the steady state experimental data presented in Fig. 4.11, the average reduction in torque ripples and the THD attained by the proposed 3L-DTC is 66.19% and 39.4%, respectively, when compared to classical 3L-DTC. In comparison, the average torque ripple reduction obtained by DDTC-1 and DDTC-2 compared to classical 3L-DTC is only 48.6% and 52.3%, respectively.

The flux regulation and the average THD of the stator current in the proposed 3L-DTC drive is also superior when compared to DDTC-1 and DDTC-2 methods. Overall, the proposed method achieves about 36.8% and 32.5% more reduction in

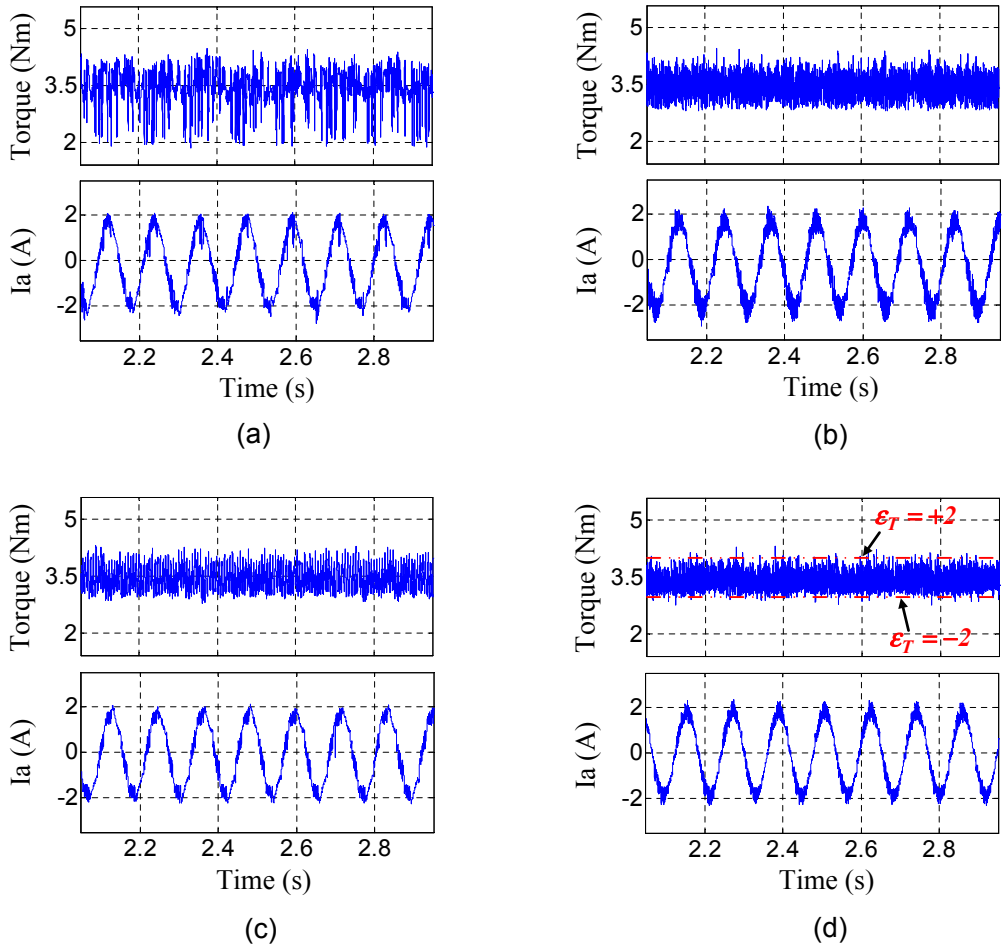

Figure 4.10: Steady state responses of the IPMSM drive at 250 rpm, 3.5 Nm; (a) Conventional 3L-DTC. (b) DDTC-1. (c) DDTC-2. (d) Proposed 3L-DTC.

THD than DDTC-1 and DDTC-2, respectively.

4.7.3 Low speed performance improvement

The steady state low speed performance of the proposed 3L-DTC is evaluated through experiments carried out at 3% of the test IPMSMs rated speed (15 rpm), with a load of 3.5 Nm. The torque response and stator current corresponding to DDTC-1, DDTC-2, proposed 3L-DTC with and without low speed flux drooping control are shown in Fig. 4.12.

DDTC-1 shows the worse performance among the three DDTC methods. In fact, the stator current THD of the DDTC-1 method is almost as poor as the

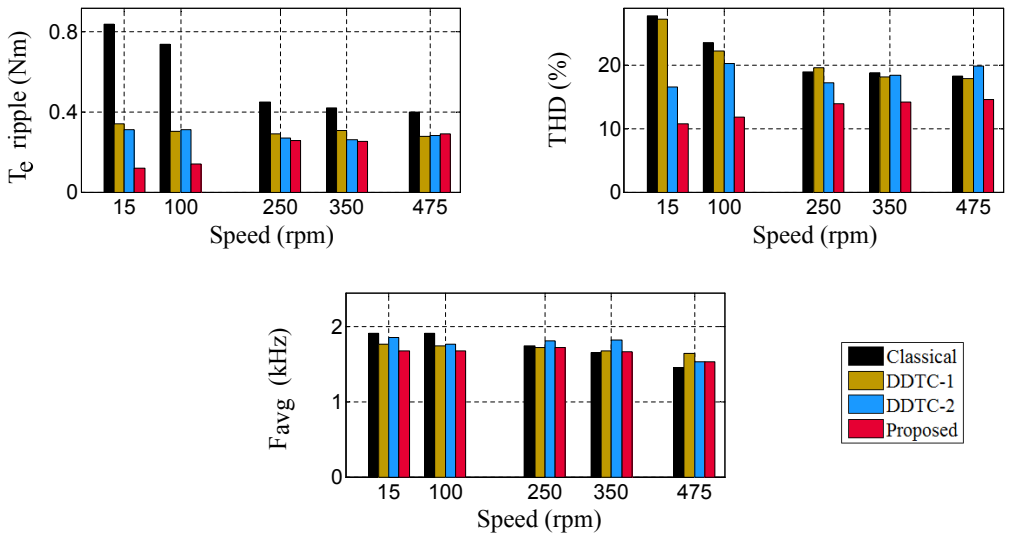

Figure 4.11: Comparison of steady state torque ripple, stator current THD and the average switching frequency at different operating speeds (3.5 Nm).

classical 3L-DTC (see Fig. 4.11). With DDTC-2, the flux drooping problem is solved by applying the modified switching table proposed in [91], [93]. Nevertheless, the modified table uses up to four vectors in one switching cycle, and smooth vector switching criteria, similar to DDTC-1, is not considered. Therefore, low order harmonics in the stator current are increased, as shown in Fig. 4.12(b).

The flux drooping problem is clearly noticeable in Fig. 4.12(c) which shows the responses of the proposed 3L-DTC without the flux drooping control algorithm. As the flux drooping control is enabled, it can be seen in Fig. 4.12(d) that the THD of the stator current is significantly improved.

It should also be noted that the both DDTC-1 and DDTC-2 methods use MVVs at low speeds. This will lead to larger neutral point voltage fluctuations than the proposed 3L-DTC which uses mostly SVVs as the active vectors in this speed range. The smaller neutral point voltage fluctuations in the proposed 3L-DTC drive also contribute to the smaller THD seen in the stator currents.

In the proposed 3L-DTC drive, the modulation index m of SVV in the vector combination of MVV-SVV-ZVV is fixed; it is fixed to 0.1 when $\omega_r < 0.5\omega_n$ and regulated thereafter according to the operating speed (see Table 4.3). Consequently,

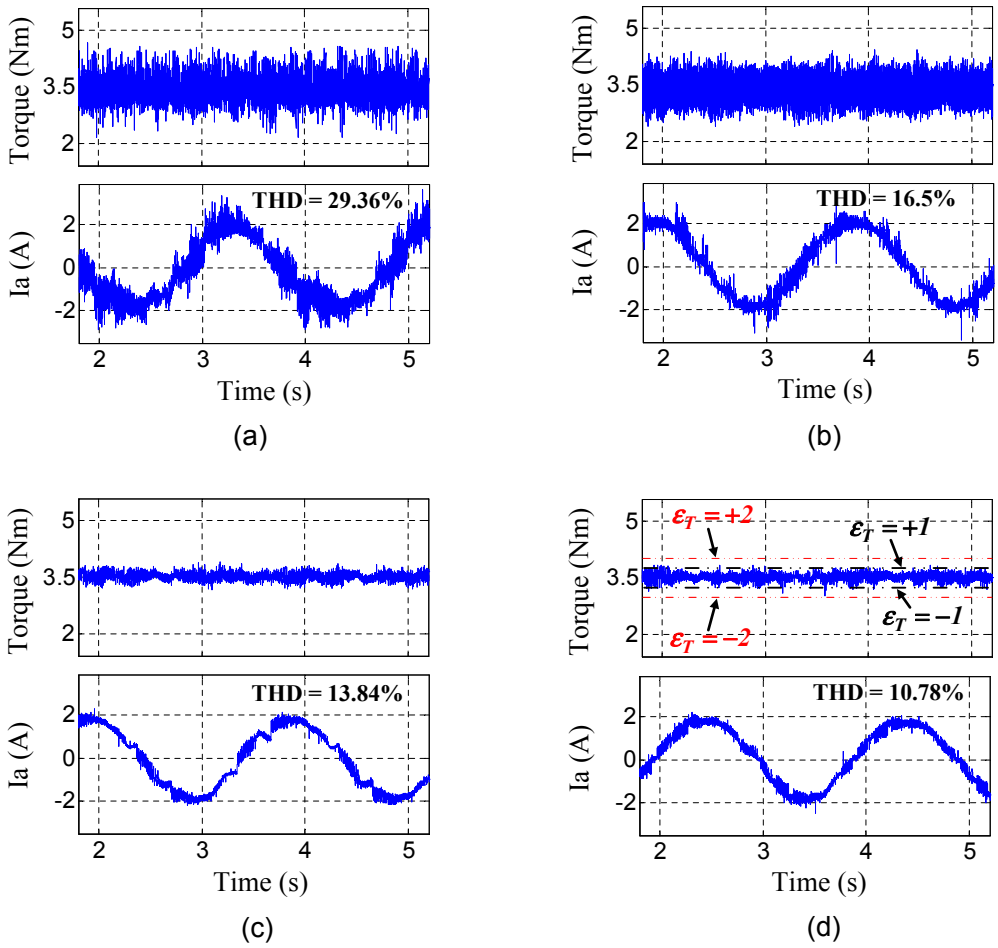

Figure 4.12: Steady state responses of the IPMSM drive at 15 rpm, 3.5 Nm; (a) DDTC-1 (b) DDTC-2. (c) Proposed 3L-DTC without low speed improvement. (d) Proposed 3L-DTC with low speed improvement.

the suppression effect of SVV on the fluctuations of the neutral point voltage could decrease, especially for medium to low speed operations.

In order to examine the control performance of the neutral point voltage, especially in medium to low speed ranges, the experimental waveforms of dc-link capacitor voltages are shown in Fig. 4.13. The results show that the fluctuations in the NP voltages at lower speeds are not significant; in fact, it is much lower than the fluctuations at higher speed due to the following reasons.

Firstly, when MVV-SVV-ZVV combinations are used during lower speeds, the torque slopes of MVVs are very high. Therefore, the duty ratio of MVV in a

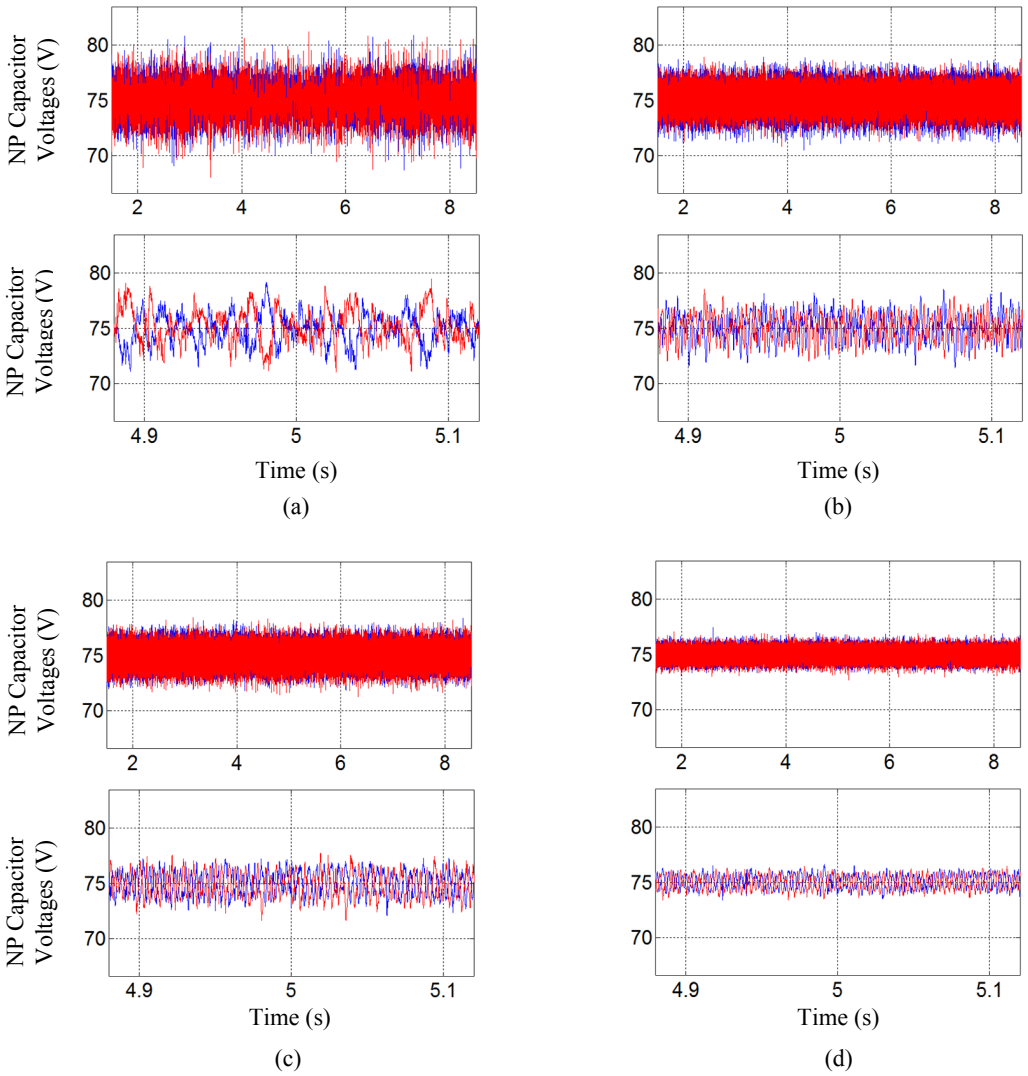

Figure 4.13: Steady state dc-link capacitor voltages when the IPMSM is operating with a load of 4 Nm at different operating speeds: (a) 475 rpm. (b) 250 rpm. (c) 100 rpm. (d) 15 rpm. Zoomed-in dc-link capacitor voltages are showed in the bottom figures.

switching cycle would be very low when compared to the duty cycle of the MVV at higher speeds. This means that MVVs will be applied for a shorter time (compared to high speed regions) in a switching cycle and therefore, the fluctuations in neutral point voltage would be smaller.

Secondly, the back e.m.f of the machine is low at lower speeds. Hence, at steady state, the output of the proposed four-level torque hysteresis controller would be

confined mostly to low torque demands $\epsilon_T = \pm 1$. This means that SVV-ZVV would be applied most of the time during low speeds. Voltage vector combinations involving LVVs and MVVs will still be used; however, its usage frequency would diminish in tandem with the back e.m.f of the machine. As more and more SVV-ZVV combinations are used during low speeds, neutral point voltage fluctuations will be better controlled.

The application of mainly SVV at lower speeds is confirmed in Fig. 4.14 which shows the line voltage V_{ab}, recorded using a digital oscilloscope, when the proposed 3L-DTC drive is operating at speeds of $0.2\omega_n$ and $0.8\omega_n$. Additionally, the zoomed-in line voltages in Figs. 4.14(b) and 4.14(d) illustrate the vector switching sequencing within each sampling cycle. It can be observed that proposed voltage vector selection principles are respected to achieve smooth voltage vector switching.

4.7.4 Parametric robustness of the proposed method

Based on the theoretical analysis presented in Section 3.6, the sensitivity of steady state and transient drive performances to variations in C_1 and C_2 are presented in Figs. 4.15 and 4.16, respectively.

Fig. 4.15 depicts the steady state torque response when the design parameters C_1 and C_2 are detuned as the machine is operating at a speed of 350 rpm, with a load torque of 3.5 Nm. At $t = 25$ s, C_1 is decreased by 20% to 0.944, while C_2 is detuned by +20% to -0.0018 at $t = 50$ s. No significant changes in torque response are immediately noticeable in Fig. 4.15. Nevertheless, a slight increment in torque ripples of about 5.4% was detected due to the detuning of C_1, which substantiates the earlier analysis that a decrement in C_1 could increase the torque ripples. With the detuning of C_2, the change noted in torque ripples is even smaller; torque ripples are increased by about 2.2%.

The transient torque response as C_1 is increased by 20% is shown in Fig. 4.16 (a). As C_1 is increased, the duty cycle control will intensify, i.e., the duty ratio of the active vector will reduce as the torque error reduces. This leads to the

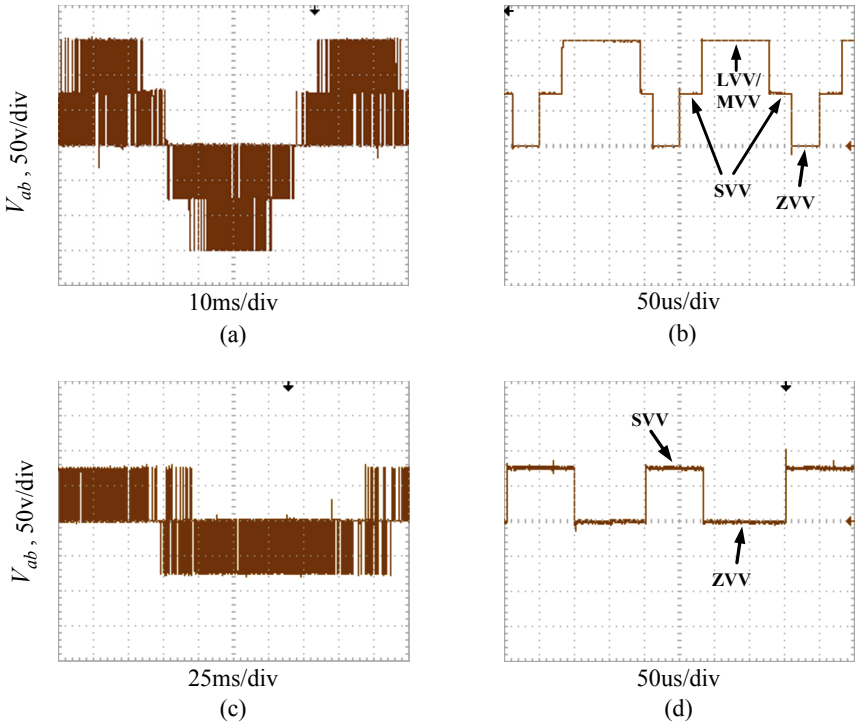

Figure 4.14: Line voltage at different speeds and their respective zoomed-in profile showing the proposed voltage vector sequencing within each sampling cycle. (a) and (b) 400 rpm. (c) and (d) 100 rpm.

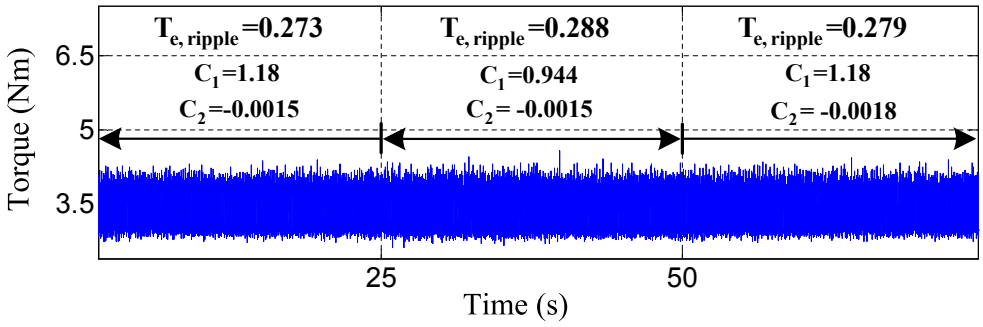

Figure 4.15: Steady state torque response with the detuning of C_1 and C_2.

slightly slower torque response as observed in Fig. 4.16 (a). Conversely, when C_2 is detuned by +20% as shown in Fig. 4.16(b), negligible improvement in transient response is noted.

The transient and steady state experimental results demonstrate the sensitivity of the torque dynamics in the IPMSM to substantial variations in the tuned design

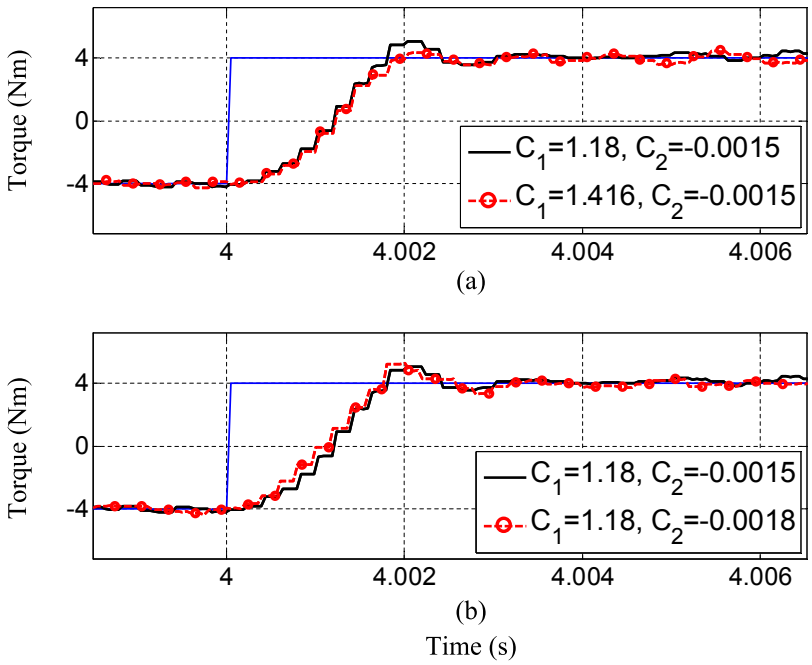

Figure 4.16: Transient torque responses with the detuning of design parameters. (a) C_1 detuned by +20%. (b) C_2 detuned by +20%.

constants. At the same time, it can be reasoned that when the proposed 3L-DTC drive is operating with tuned design constants, C_1 and C_2, and if the known machine parameters vary, the impact on drive performance will be marginal as shown in this subsection. Therefore, it can be concluded that the proposed method is adequately robust against the machine parameter variations.

The experimental evidence and analysis presented in this section confirm the effectiveness of the proposed method in reducing torque ripples and output THD in 3L-DTC drives. Compared to the existing DDTC algorithms in DDTC-1 and DDTC-2, the proposed method achieves marginal improvement in torque ripple reduction during normal and high speeds, nevertheless, with reduced machine parameter dependence. In addition, the approximation of m, the modulation index of the SVVs, in the proposed method means that the duty cycle calculation is less computationally taxing than both DDTC-1 and DDTC-2. This is confirmed by the tabulated run-times of the DSP in Table 4.5 as the IPMSM is operating at half the rated speed with a load of 3.5 Nm. It can be noticed that the run-times of the

Table 4.5: DSP Run-times of the DTC algorithms at 250 rpm, 3.5 Nm

Method	Time (μs)
Classical 3L-DTC	19.43
DDTC-1	28.95
DDTC-2	31.36
Proposed 3L-DTC	26.57

proposed method are approximately 8.2% and 15.3% lower than the DDTC-1 and DDTC-2, respectively. The higher run-time of DDTC-1 can be attributed to the prediction and comparison of torque slope multiple times within each sampling cycle while the analytical TR-RMSM approach to determine the duty cycles in DDTC-2 leads to the solving of lengthy quadratic equations.

When comparing the low speed performances, the proposed method is clearly superior in terms of torque ripples and THD. In fact, the THD in the proposed 3L-DTC drive is significantly lower than DDTC-1 and DDTC-2 at all operating speeds, and this can be attributed to the strict smooth voltage vector switching criteria and the introduction of VVSV during low speeds.

Needless to say, the application of VVV and VSVV slightly increases the complexity of switching mechanism in the proposed method. However, such switching mechanisms can be easily implemented in a DSP controller, and the average switching frequency in the proposed 3L-DTC drive is kept well below 2 kHz as shown in Fig. 15.

4.8 Conclusion

In this chapter, a novel duty cycle based 3L-DTC algorithm is presented to improve the performance of a 3L-NPC inverter driven IPMSM through the use of zero voltage vectors as passive vectors. In the proposed method, up to three

voltage vectors are applied sequentially within each switching cycle to improve the regulation of torque and flux under all operating conditions.

Different from the existing duty cycle based 3L-DTC algorithm in the literature that uses zero voltage vector to minimize torque ripples, the duty ratio calculation method used in the proposed method is computationally less exhaustive and achieves parameter independence through the introduction of tunable control parameters. Furthermore, the switching constraints of the 3L-NPC inverters are respected, with special attention paid to voltage vector sequencing within each switching period to attain smooth voltage vector switching.

The proposed method also reduces the effects of stator flux drooping during low operating speeds through a simple improvisation that does require the use of the medium voltage vectors as previously proposed by a prior art. Instead, virtual short voltage vectors, synthesized from two adjacent short voltage vectors are used to mitigate the droop in flux during low speeds.

The experimental results of the proposed 3L-DTC algorithm are presented and comparatively analyzed against that of classical 3L-DTC and two other duty cycle based 3L-DTC algorithms in the literature to confirm the effectiveness and superiority of the proposed method.

Chapter 5

Constant Switching Frequency Based 3L-DTC of IPMSM

5.1 Motivation and Objectives

At the cost of little increment in complexity, DDTC methods significantly improve the regulation of torque and flux in switching table based DTC drives. When compared to classical DTC drives, the variations in the inverter switching frequency of DDTC drives are relatively moderate as a fixed number of voltage vectors are applied sequentially within each switching cycle. Nonetheless, as the experimental results prove for the two-level inverter fed DDTC algorithms in [40], [81] and also the proposed DDTC methods in the previous chapters, the inverter switching frequency remains variable in DDTC drives.

The main reason for variable inverter switching frequency in DTC drives is the use of hysteresis control with fixed bands to regulate torque and flux, both of which have variations rates that depend on the operating point of the machine. Accordingly, some studies have recommended the use of variable hysteresis bands to achieve constant inverter switching frequency in switching table based 2L-DTC drives [104], [105]. Nevertheless, these methods use analytical approaches that are complicated and machine parameter dependent. For instance, the method in [104] proposes an offline determination of optimal hysteresis bands to minimize the harmonic distortion in motor currents for the desired switching frequency. On

the other hand, the proposed method in [105] requires integrators, pulse counters and linear regulators for the adaptation of hysteresis bands to attain constant switching frequency.

In order to achieve constant inverter switching frequency in 3L-DTC drives, a novel 3L-DTC algorithm is proposed in this chapter. The proposed method is effective in significantly reducing the high torque and flux ripples at low and constant switching frequency while addressing the intrinsic switching limitations of the 3L-NPC inverter. Furthermore, it reserves the merits of simplicity and robustness of the conventional DTC. The block diagram of the proposed 3L-DTC algorithm is shown in Fig. 1. It can be seen that a simple torque regulator, consisting of a PI controller and triangular carriers, is introduced to replace the conventional torque hysteresis controller in the classical 3L-DTC setup.

This remainder of this chapter is organized as follows. In Section 5.2, the proposed constant switching frequency based 3L-DTC strategy is introduced. Design guidelines and detailed stability analysis of the proposed torque regulator using small signal modeling are provided in Section 5.3. The voltage vector switching strategies adopted in the proposed method are discussed in Section 5.4. Experimental results are presented in Section 5.5: firstly, the transient and steady state responses are comparatively analyzed against those of classical 3L-DTC and a prior DDTC method to verify the effectiveness of the proposed method; secondly, a detailed analysis is carried out to investigate the parametric robustness of the proposed 3L-DTC.

5.2 Proposed Constant Switching 3L-DTC Algorithm

The inverter switching frequency in a DTC drive is a function of the fixed torque and flux hysteresis bands and the motor operating point in terms of rotational speed and load torque [101]. From the discussion on torque and flux variation rates of an IPMSM DTC drive in Section 2.3, three important aspects are clear:

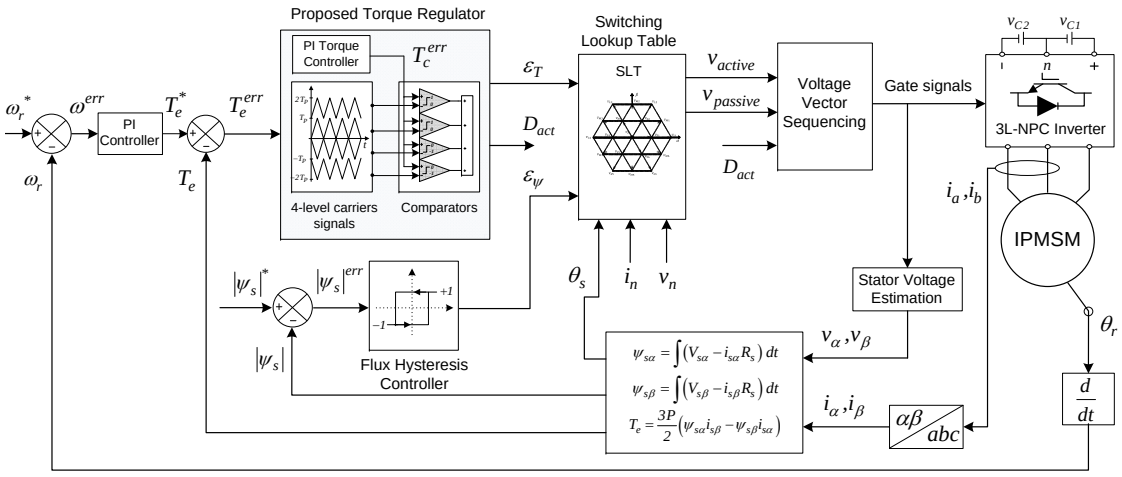

Figure 5.1: Block diagram of the proposed constant switching frequency based 3L-DTC scheme.

1) the variation rates of torque and flux vary according to the operating point of the machine; 2) torque variation rates are much larger than those of flux; 3) when compared to torque variation rates, the variation rates of flux are not heavily influenced by the operating point of the motor. Consequently, the regulation of flux has negligible influence on the switching frequency variations in DTC drives [35]. On the contrary, the inverter switching frequency is heavily influenced by the large variations of torque slope.

In the proposed 3L-DTC, a torque regulator is introduced in place of the traditional torque hysteresis controller to minimize the influence of large torque slopes to attain a constant inverter switching frequency with reduced torque ripples. The detailed block diagram of the proposed torque regulator consisting of a PI controller, four triangular carriers and the corresponding comparators is illustrated in Fig. 5.2.

By using a PI controller to reshape and smoothen the torque error T_e^{err} , the effects of large torque slopes are negated, and this is desirable for reducing torque ripples. A constant switching frequency is achieved by using triangular carriers that have a peak to peak amplitude of T_p. The smoothened output of the PI

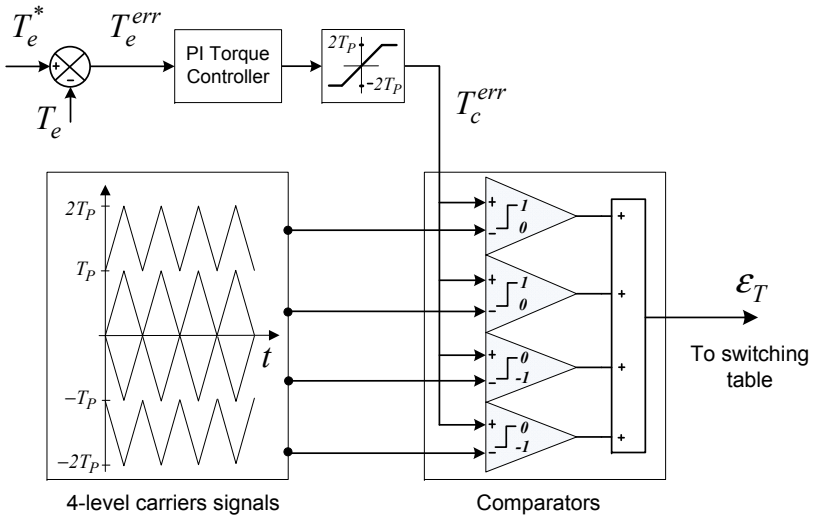

Figure 5.2: Proposed torque regulator.

controller is limited to $\pm 2T_p$, and compared individually with the four triangular carriers. Subsequently, the outputs of the comparators are added up to synthesize the torque regulator output ϵ_T, which in principle will be analogous to a five-level hysteresis controller output.

The possible outputs from the proposed torque regulator are shown in Fig. 5.3. For instance, if the output of the PI controller (T_c^{err}) lies between T_p and $2T_p$, the torque regulator will produce an output of high torque demand ($\epsilon_T = +2$) for a period of time ($D_{act}T_{carr}$) during each switching cycle T_{carr}. For rest of the switching cycle ($(1 - D_{act})T_{carr}$), the torque demand will be low ($\epsilon_T = +1$), which means that two voltage vectors with differing torque variation rates can be applied sequentially in each switching cycle. Note that the term D_{act} is used here to denote the duty ratio of the main voltage vector to be applied in each switching cycle.

From Section 3.2 and (2.18), it can be observed that the torque variation rate of SVVs decreases as the speed of IPMSM is increased. In fact, it eventually becomes negative as the operating speed approaches the rated speed. As the operating speed increases, LVV/MVVs are required to counteract the back e.m.f of the motor. Therefore, the PI controller output T_c^{err} will be between $2T_p$ and T_p. This will prompt the torque regulator output states of $\epsilon_T = +2$ and $\epsilon_T = +1$ in

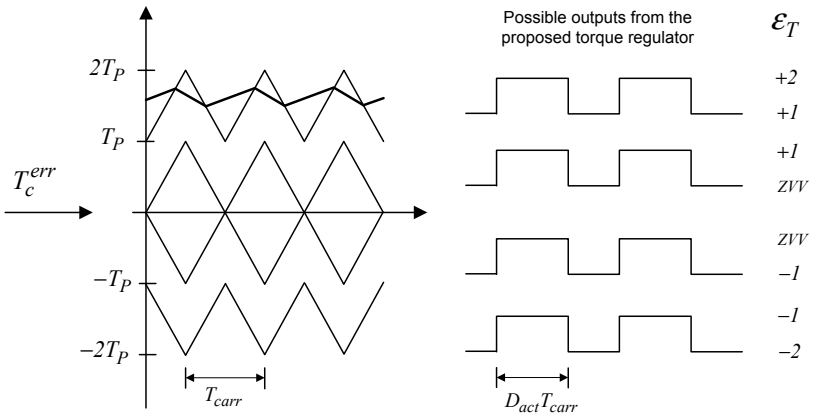

Figure 5.3: Expected outputs from the torque regulator.

one switching cycle.

Since two voltage vectors are to be applied within each switching cycle, the switching logic used for the proposed two-vector based DDTC algorithm in Chapter 3 (see Table 3.1) is used for the proposed constant switching frequency based 3L-DTC method. i.e., the switching table used in this chapter is based on four-level ($\epsilon_T = \pm 2, \pm 1$) torque and two-level ($\epsilon_\psi = \pm 1$) flux hysteresis control with sector identification realized using twelve equal sectors of 30° (S_{1a}, S_{1b}, S_{2a}, ..., S_{6b}).

In the proposed method, a LVV/MVV is applied as the active vector when the torque regulator output is $\epsilon_T = +2$. When the output is $\epsilon_T = +1$, a SVV that is adjacent to the selected LVV/MVV is chosen as the passive vector. For example, in sector S1a, if torque ($\epsilon_T = +2$) and flux ($\epsilon_\psi = +1$) demands are high and positive, the chosen vector combination would be $v_{L2} - v_{S2}$.

Conversely, when the operating speed of the machine is low, T_c^{err} is expected to lie between T_p and 0. During this period, SVVs will have positive torque slopes, whereas the torque slopes of ZVVs will be negative. Therefore the vector combination of a SVV and ZVV can be applied sequentially in a switching cycle to control the torque ripples. It has to be noted that ZVVs are always selected appropriately to keep the switching transition to a minimum, e.g., 110 → 111, 00-1 → 000.

The aforementioned observations are also applicable when machine speed is reversed. For completeness, the expected output of the proposed torque controller

for reversed speed operation is also shown in Fig. 5.3.

5.3 Design of Torque Regulator

Small signal modeling technique is employed to analyze the stability of the proposed torque controller. To simplify the analysis, two basic assumptions are made below without the loss of generality. Firstly, the voltage drop across the stator resistance is assumed to be negligible. Therefore, the $x-$component of stator voltage is equivalent to the rate of change of stator flux. Typically, the small flux hysteresis bandwidth used in DTC drives ensures that flux is tightly regulated and is nearly constant. This means that both v_{sx} and V_{sy} can be approximated as constants as shown in (5.1) and (5.2).

$$v_{sx} = \rho|\psi_s| \approx 0 \tag{5.1}$$

$$\begin{cases} v_{sy} = |v_s|, & T_e^{err} > 0 \\ v_{sy} = -|v_s|, & T_e^{err} < 0 \end{cases} \tag{5.2}$$

Secondly, it is assumed that the active flux is aligned with the x-axis as shown in (5.3), which means that the angle between the rotor and stator flux linkages, δ is assumed to be zero. It is noted that such an assumption is only introduced for the simplicity of expression, and it does not affect the validity of the modeling as shown in the following sections. Consequently, the torque variation rate in (2.18) is modified to (5.4).

$$\psi_{rx} = \psi_r \cos\delta \approx \psi_r \tag{5.3}$$

$$\rho T_e = -\frac{R_s}{L_q} T_e + \frac{3P}{2L_q}(v_s - |\psi_s|\omega_{re})\psi_r \tag{5.4}$$

5.3.1 Average torque variation rate

In the proposed 3L-DTC algorithm, one active and one passive voltage vector is applied during each switching cycle. Therefore, the average torque variation rate

can be expressed in terms of the duty ratio of the active vector D_{act} as

$$\rho T_{e(avg)} = D_{act}\rho T_{e(active)} + (1 - D_{act})\rho T_{e(passive)} \tag{5.5}$$

By referring to the proposed voltage vector selection logic in Table 3.1, three vector combinations (LVV-SVV, MVV-SVV and SVV-ZVV) are possible. From the analysis of torque variation rates in Chapter 3, it follows that the magnitude of a LVV in a sector is twice the magnitude of a SVV as they are spatially aligned. Hence, the average torque variation rate for a LVV-SVV combination can be derived as

$$\begin{aligned}\rho T^{L}_{e(avg)} =& D_{act}\Big[- \frac{R_s}{L_q}T_e + \frac{3P}{2L_q}\Big(v_s - |\psi_s|\omega_{re}\Big)\psi_r\Big] + \\ & (1 - D_{act})\Big[- \frac{R_s}{L_q}T_e + \frac{3P}{2L_q}\Big(\frac{1}{2}v_s - |\psi_s|\omega_{re}\Big)\psi_r\Big]\end{aligned} \tag{5.6}$$

In the case of a MVV-SVV combination, the vectors are not spatially aligned. The ratio between a MVV and a SVV varies from 0.5 to 0.33 in a sector. Using the rationale explained previously in Section 3.3, the maximum ratio of 0.5 is taken as the reference point to derive the average torque variation rate for the MVV-SVV combination as

$$\begin{aligned}\rho T^{M}_{e(avg)} =& D_{act}\Big[- \frac{R_s}{L_q}T_e + \frac{3P}{2L_q}\Big(\frac{\sqrt{3}}{2}v_s - |\psi_s|\omega_{re}\Big)\psi_r\Big] + \\ & (1 - D_{act})\Big[- \frac{R_s}{L_q}T_e + \frac{3P}{2L_q}\Big(\frac{\sqrt{3}}{4}v_s - |\psi_s|\omega_{re}\Big)\psi_r\Big]\end{aligned} \tag{5.7}$$

Simplifying (5.6) and (5.7), it is found that the average torque variation rate when either a LVV or MVV is used in combination with a SVV is the same and can be expressed as

$$\rho T^{LM}_{e(avg)} = -\frac{R_s}{L_q}T_e + \frac{3P}{2L_q}\psi_r\Big[\frac{1}{2}v_s(1 + D_{act}) - |\psi_s|\omega_{re}\Big] \tag{5.8}$$

In a similar manner, the average torque variation rate for a SVV-ZVV combination can be derived as

$$\rho T^{S}_{e(avg)} = -\frac{R_s}{L_q}T_e + \frac{3P}{2L_q}\psi_r\Big[\frac{1}{2}v_s D_{act} - |\psi_s|\omega_{re}\Big] \tag{5.9}$$

5.3.2 Small-signal control-to-output transfer function

The variables T_e and D_{act} in (5.8) and (5.9) can be decomposed into the sum of AC and DC components as

$$T_e = T_{e,0} + \widetilde{T}_e \tag{5.10}$$

$$D_{act} = D_{act,0} + \widetilde{D}_{act} \tag{5.11}$$

By substituting (5.10) and (5.11) into (5.8) and (5.9), and after removing the DC components, it is found that the derived equations in both instances, reduce to

$$\rho\widetilde{T}_e = -\frac{R_s}{L_q}\widetilde{T}_e + \frac{3P}{4L_q}\psi_r v_s \widetilde{D}_{act} \tag{5.12}$$

Equation (5.12) represents the piecewise linear approximation of the proposed torque regulator, from which, the control-to-output transfer function can be deduced as

$$\widetilde{T}_e(s) = \frac{3P\psi_r v_s}{4L_q\Big(s + \frac{R_s}{L_q}\Big)}\widetilde{D}_{act}(s) \tag{5.13}$$

5.3.3 Design guidelines of the torque regulator

The small-signal closed-loop block diagram of the proposed torque regulator is shown in Fig. 5.4, where K_p and K_i represent the proportional and integral gains of the torque PI controller respectively. The closed loop transfer function of the torque regulator can be expressed in the standard second-order form as

$$G(s) = \frac{\widetilde{T}_e(s)}{\widetilde{T}_e^*(s)} = \frac{A(K_p s + K_i)}{s^2 + s(AK_p + \frac{R_s}{L_q}) + AK_i} \tag{5.14}$$

where $A = \frac{3P\psi_r v_s}{4L_q T_p}$.

Then, the controller gains can be derived in terms of the designing damping ratio (ζ_d) and natural frequency (ω_{nd}) as

$$K_p = \frac{1}{A}\Big(2\zeta_d\omega_{nd} - \frac{R_s}{L_q}\Big) \qquad\qquad K_i = \frac{\omega_{nd}^2}{A} \tag{5.15}$$

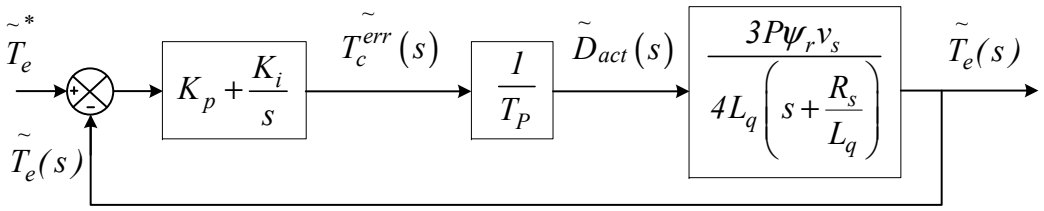

Figure 5.4: Small signal closed-loop block diagram of the proposed torque regulator.

In second-order systems, the transient response is typically parameterized by the percentage overshoot, $OS\%$ (5.16) and the settling time, T_{st} (5.17). Therefore, based on the required transient response, appropriate values for ζ_d and ω_{nd} can be carefully selected by the designer.

$$OS\% = e^{-\frac{\zeta_d \pi}{\sqrt{1-\zeta_d^2}}} \times 100 \tag{5.16}$$

$$T_{st} = \frac{4}{\zeta_d \omega_{nd}} \tag{5.17}$$

Additionally, it is worth highlighting the correlation between the absolute slopes of the PI controller output (T_c^{err}) and the triangular carriers. The proposed torque regulator works on the principle that the torque variation rate or slope is changed periodically within each switching cycle. Therefore, it is important to ensure that the absolute maximum slope of T_c^{err} does not exceed the absolute slope of the triangular carriers ($|\rho T_{ri}|$) under all operating conditions. Otherwise, poor torque dynamics and in a worst case scenario, the motor will be out of control. The absolute slope of T_c^{err} is mainly influenced by the proportional gain of the controller. Consequently, design criterion for the proportional gain can be established as

$$|\rho T_{ri}| \geq max|\rho T_e| K_p \tag{5.18}$$

From (2.18), it follows that the maximum decreasing torque slope in an IPMSM is always greater than the maximum increasing slope. In other words, the maximum torque variation will occur at the rated speed and torque when a LVV,

corresponding to torque hysteresis state $\epsilon_T = -2$, is used. Accordingly, motor parameters can be substituted into (2.18) and if either the desired switching frequency or the tuned proportional gain K_p is known, the design criterion in (5.18) can be computed. For instance, the absolute maximum torque slope is approximately $1.1 \times 10^4 s^-1$ for IPMSM used in this study. In experiments, a fixed switching frequency of 2 kHz is used for the proposed 3L-DTC algorithm and this equates to a slope of $5 \times 10^4 s^-1$ for the triangular carriers. As a result, the design criteria for K_p can be established as $K_p < 4.545$.

5.3.4 Validity of s-domain based analysis

In general, s-domain analysis is used for continuous time signals while z-domain analysis is preferred for discrete control systems such as the proposed torque regulator. Nonetheless, if sufficiently high sampling frequencies are used, the simpler s-domain approach can provide a good approximation of discrete time system. By using high enough sampling frequencies, a quasi-continuous working area for a discrete control system can be approximated and consequently, simple Laplace transformation can be used for stability analysis.

Designing for a damping ratio of 0.75 ($\zeta = 0.75$), the natural frequency of the proposed torque regulator can be approximated as 798 rad/s using (5.15). Consequently, the poles of the system are at $-598 \pm j528$. This shows that the system has conjugate pole pairs in the left half plane (LHP) that generates a response component which is a decaying sinusoid of the form $Ke^{-598t}sin(528t + \phi)$.

To ensure the validity of Laplace transformation, the frequency range of $s = \sigma \pm j2\pi f$ must satisfy the condition $f \ll 0.5 f_{regulator}$, where $f_{regulator}$ is the operating frequency of the torque regulator. The proposed torque regulator operates with a fixed frequency of 2 kHz. As the conjugate poles pairs of the system are at $-598 \pm j528$, f is approximately 84 Hz and therefore, the condition $f \ll 0.5 f_{regulator}$ is satisfied.

5.4 Voltage Vector Sequencing

It is important that inverter switching constraints are adhered to at all times; i.e., smooth voltage vector switching criteria is given preference irrespective of the voltage vector combinations chosen according to the output of the torque regulator. As the proposed constant switching frequency based 3L-DTC method in this chapter uses the same switching lookup table as the two-vector based DDTC method in Chapter 3, the voltage vector sequencing discussed in Section 3.5 also applies to the proposed constant switching frequency based 3L-DTC.

Also, as illustrated in the block diagram of the proposed method in Fig. 5.1, the neutral point current and dc-link capacitor voltages are monitored to select appropriate SVVs to minimize the voltage imbalance between the dc-link capacitors.

5.5 Experimental Results

In this section, the performance of the proposed constant switching frequency based 3L-DTC method is experimentally verified. An annotated configuration of the experimental setup is shown in Fig. 3.11. Firstly, the transient and steady-state performance of the proposed 3L-DTC is investigated and compared to that of the classical 3L-DTC and the DDTC method proposed in [90]. Following that, parametric robustness analysis of the proposed torque regulator is presented.

For simplicity, the DDTC method in [90] is referred to as DDTC-1, in the continuation of this chapter. For the classical 3L-DTC setup, only the active voltage vectors of the switching logic in Table 3.1 are used. For all the three 3L-DTC methods, the hysteresis band of flux hysteresis controller is fixed to 1% of the rated flux. In the experiments, the sampling frequency of classical 3L-DTC and DDTC-1 is set to 20 kHz while the torque regulator in the proposed 3L-DTC is operating at fixed frequency of 2 kHz. The torque regulator gains used in the experiments are tabulated in Table. 5.1.

Table 5.1: Optimized torque regulator gains for the proposed 3L-DTC

K_p 4.25	K_i 2550	T_p 12.5

5.5.1 Transient performance

To compare the dynamic torque response of the 3L-DTC methods, the zoomed-in torque responses during reversed torque control is shown in Fig. 5.5. It can be observed that the proposed method is efficient in reducing torque ripples, and at the same time, its dynamic torque response is comparable to that of classical 3L-DTC and DDTC-1.

The dynamic responses during reverse speed control from -300 rpm to 300 rpm are depicted in Fig. 5.6. Identical speed reversal time of about 0.2 s is observed for all three 3L-DTC methods, which substantiates the excellent dynamic response of the proposed 3L-DTC algorithm.

5.5.2 Steady state performance

In a 3L-DTC drives, the dynamics of torque, flux, and dc-link capacitor voltages are all dependent on the operating point of the motor and the applied voltage vectors. To have a better understanding of these dynamics and the effectiveness of the proposed 3L-DTC algorithm in torque and flux ripple reduction, experiments were carried out at different operating speeds with a load torque of 3 Nm.

The steady state torque and current responses corresponding to three operating speeds (high, medium and low) are illustrated in Figs. 5.7-5.9. Subsequently, experimental results are quantitatively presented in Fig. 5.10. The maximum frequency used for THD calculation is 5.5 kHz while the ripple content in torque, flux and capacitor voltages are computed using (3.20).

High Speed – Fig. 5.7 shows the steady-state responses of the IPMSM at 500 rpm. As the motor speed increases, the usage frequency of LVVs/MVVs will increase to overcome the back e.m.f of the motor. Nevertheless, SVVs will still

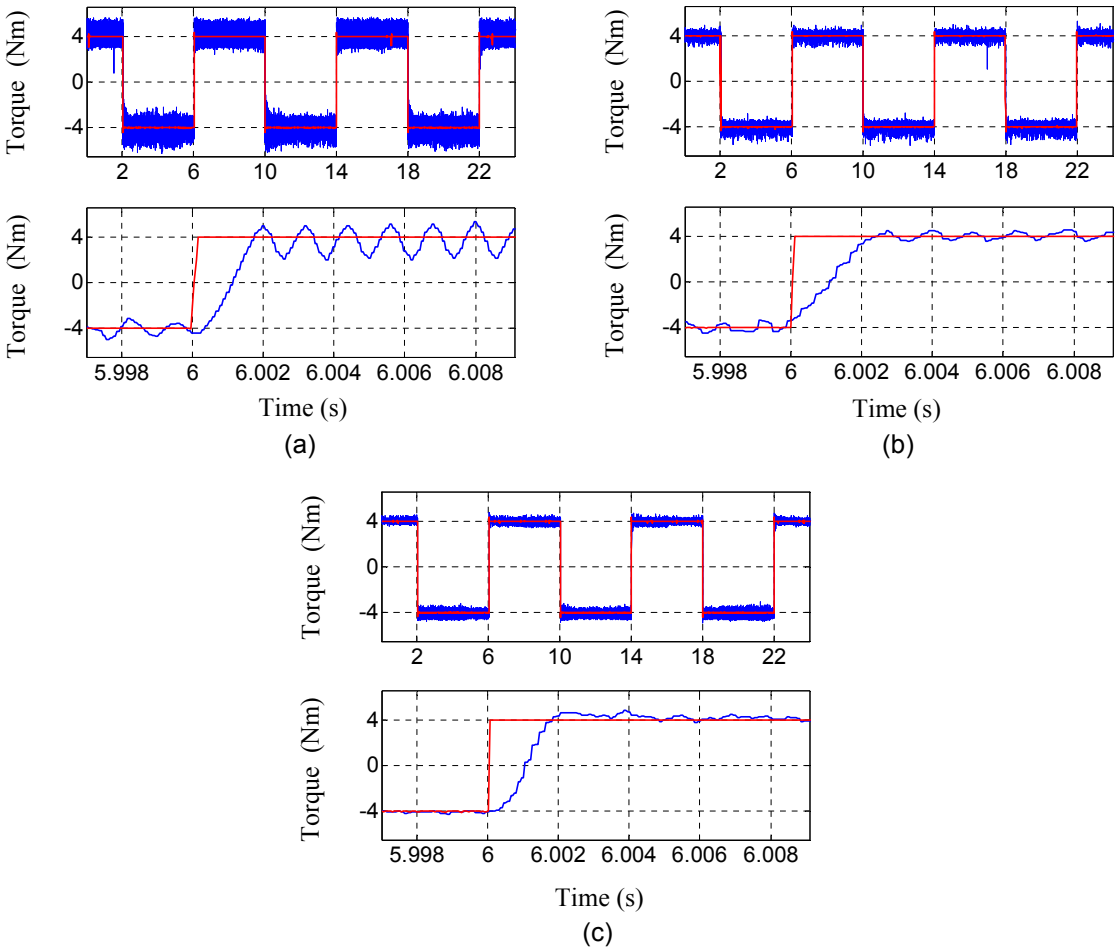

Figure 5.5: Torque Reversal from −4 Nm to 4 Nm (a) Classical 3L-DTC (b) DDTC-1 (c) Proposed 3L-DTC (Reference values: red, Actual: blue).

be used. From (2.18) and the torque slope characteristics illustrated in Fig.3.3, it is evident that the torque variation rate of SVVs in this region is nearly zero or negative. In the case of classical 3L-DTC, the usage of a single SVV will result in large torque ripples below the torque reference as shown in Fig. 5.7(a). Moreover, the torque reference will be pushed to a much higher value than the load torque (the required average torque output).

With the proposed 3L-DTC algorithm, the PI controller output T_c^{err} will be between $2T_p$ and T_p during steady state. Therefore, a LVV/MVV is applied along with a SVV during most switching cycles. SVVs are primarily used as passive

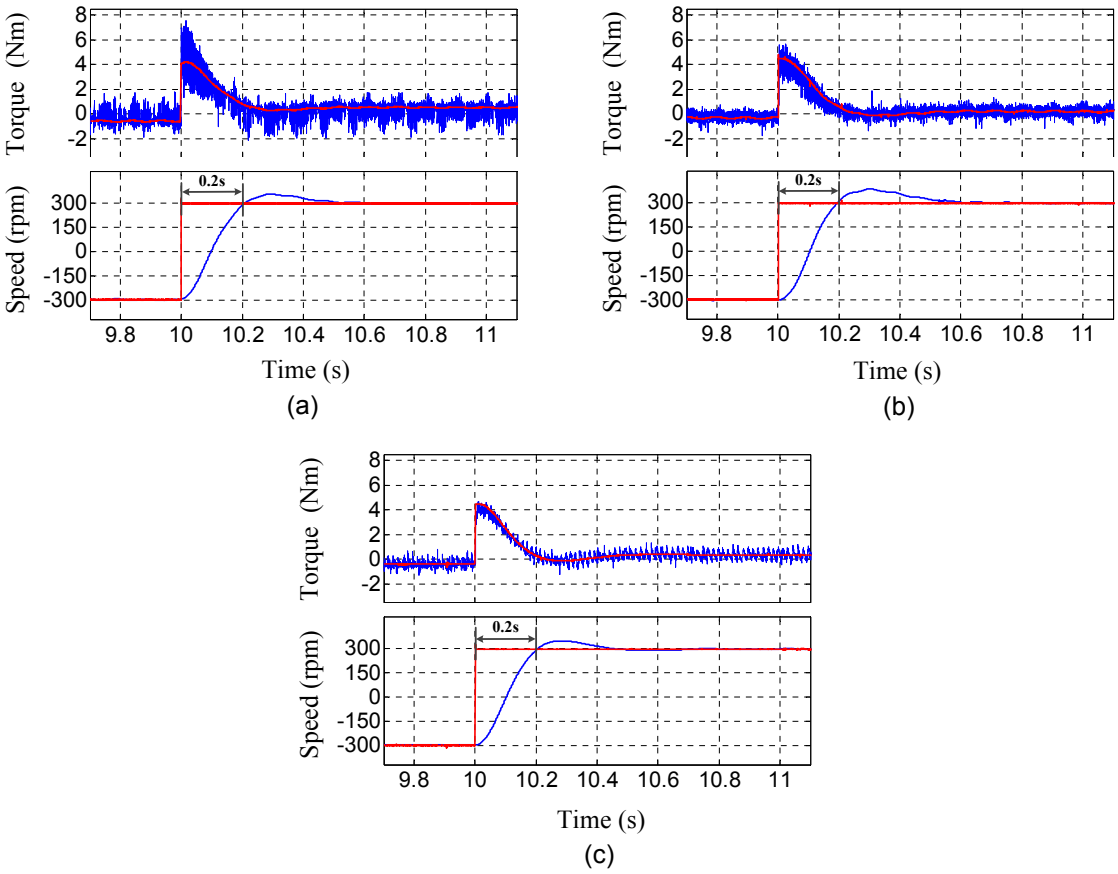

Figure 5.6: Speed Reversal from −300 rpm to 300 rpm (a) Classical 3L-DTC (b) DDTC-1 (c) Proposed 3L-DTC (Reference values: red, Actual: blue).

vectors. As shown in Fig. 5.7(c), this result in smaller torque ripples and zero steady state error between the reference torque and the average torque produced.

DDTC-1 method also shows significantly reduced torque ripples and zero steady state error in Fig. 5.7(b). Nevertheless, since this method focuses purely on torque ripple reduction, it exhibits poor stator flux regulation, and consequently, a larger stator current THD compared to classical 3L-DTC.

In contrast, flux control is improved with the proposed 3L-DTC method, as presented in Fig. 5.10. Subsequently, the THD of the output line current is improved to 8.54% as shown in Fig.5.7(c). A constant switching frequency component at 2 kHz is also clearly evident in the frequency spectrum of the output current in Fig.

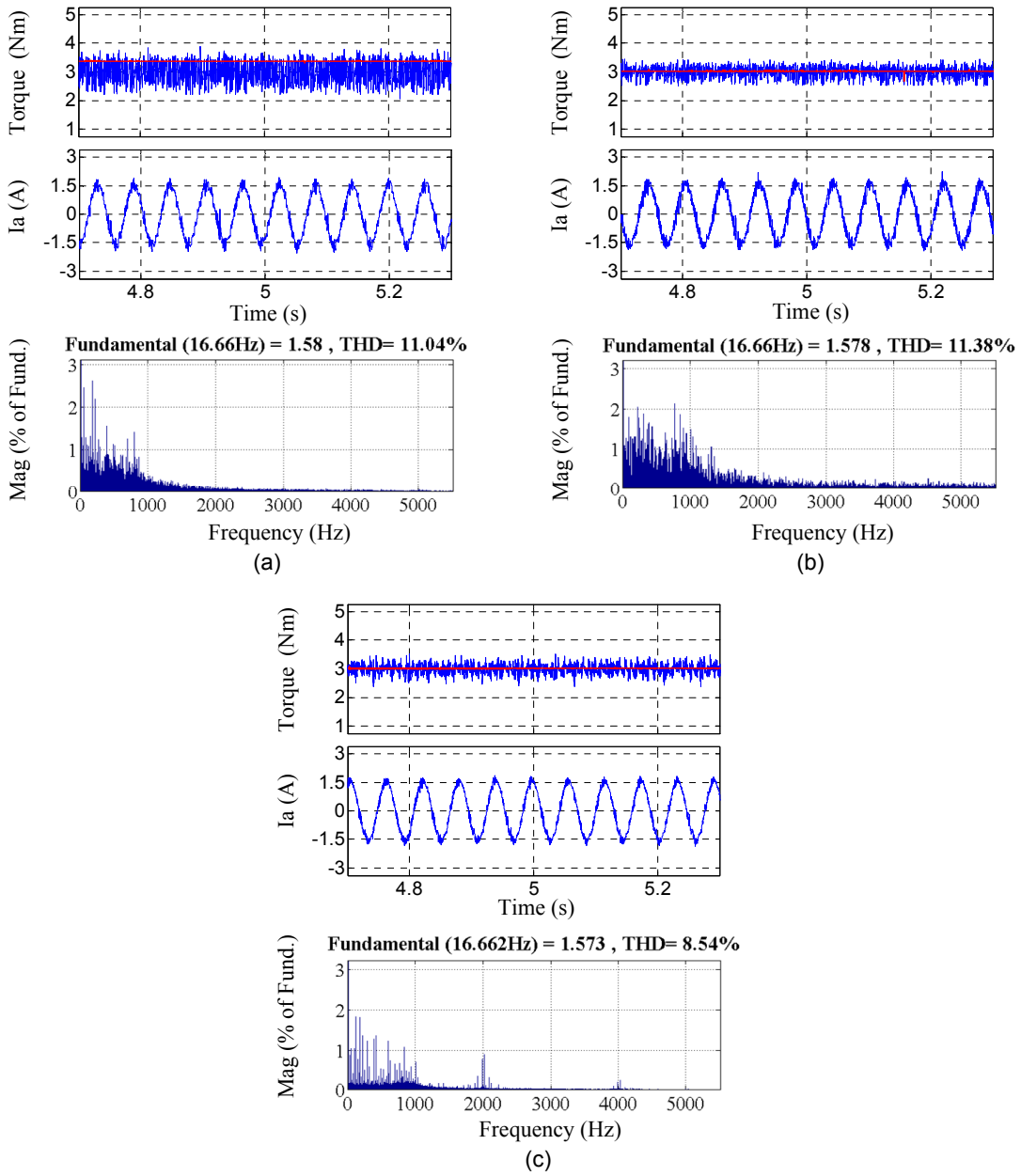

Figure 5.7: Steady-state response of the IPMSM at 500 rpm, 3 Nm. (a) Classical 3L-DTC (b) DDTC-1 (c) Proposed 3L-DTC showing torque response (top), stator current (middle) and harmonic spectrum of the stator current (bottom). (Reference values: red, Actual: blue).

5.7(c).

Medium Speed – The steady-state responses of the IPMSM, operating at a speed of 300 rpm is shown in Fig. 5.8. Compared to high speed regions, SVVs

are much more frequently used. The torque slope of SVVs will be positive in this speed range, but it is much smaller, compared to those of LVVs/MVVs.

In the case of classical 3L-DTC, the utilization of LVVs/MVVs for an entire switching cycle will result in large torque overshoots. This will in turn lead to the application of negative torque producing voltage vectors. The application of negative torque producing voltage vectors, which have large negative torque variations at these speeds, will ultimately result in the large torque ripples seen in Fig. 5.8(a). In contrast, the proposed 3L-DTC algorithm controls the torque overshoot by manipulating the time intervals of LVV/MVVs and SVVs. This leads to a reduction of almost 50% in torque ripples (see Fig. 5.10). Moreover, the limited application time of LVVs/MVVs ensures a better control of stator flux trajectory.

Consequently, an improvement in stator current THD, from 13.67% to 8.66%, is observed in Fig. 5.8(c). It is seen in Fig. 5.8(b) that torque ripples are also effectively reduced by DDTC-1. However, poor stator current performance is again, clearly noticeable.

Low Speed − Fig. 5.9 shows the steady-state responses of the IPMSM at an operating speed of 50 rpm. To avoid large torque ripples in this speed range, it is important to minimize the usage of LVV/MVVs. With the classical 3L-DTC, it is impossible to limit the usage of voltage vectors to mainly SVVs unless large torque hysteresis bands are used. Using larger band could confine the torque hysteresis controller output to be between $+1$ and -1. However, this will result in steady state torque errors at high speed regions, and consequently, the drive response could become sluggish.

LVV/MVVs are also frequently employed in the case of DDTC-1, leading to poor flux control. Subsequently, large THD is observed in the stator current as shown in Fig. 5.9(b). It is also noticeable that the percentage of torque ripple reduction by DDTC-1 is slightly lower than that of the proposed method. This

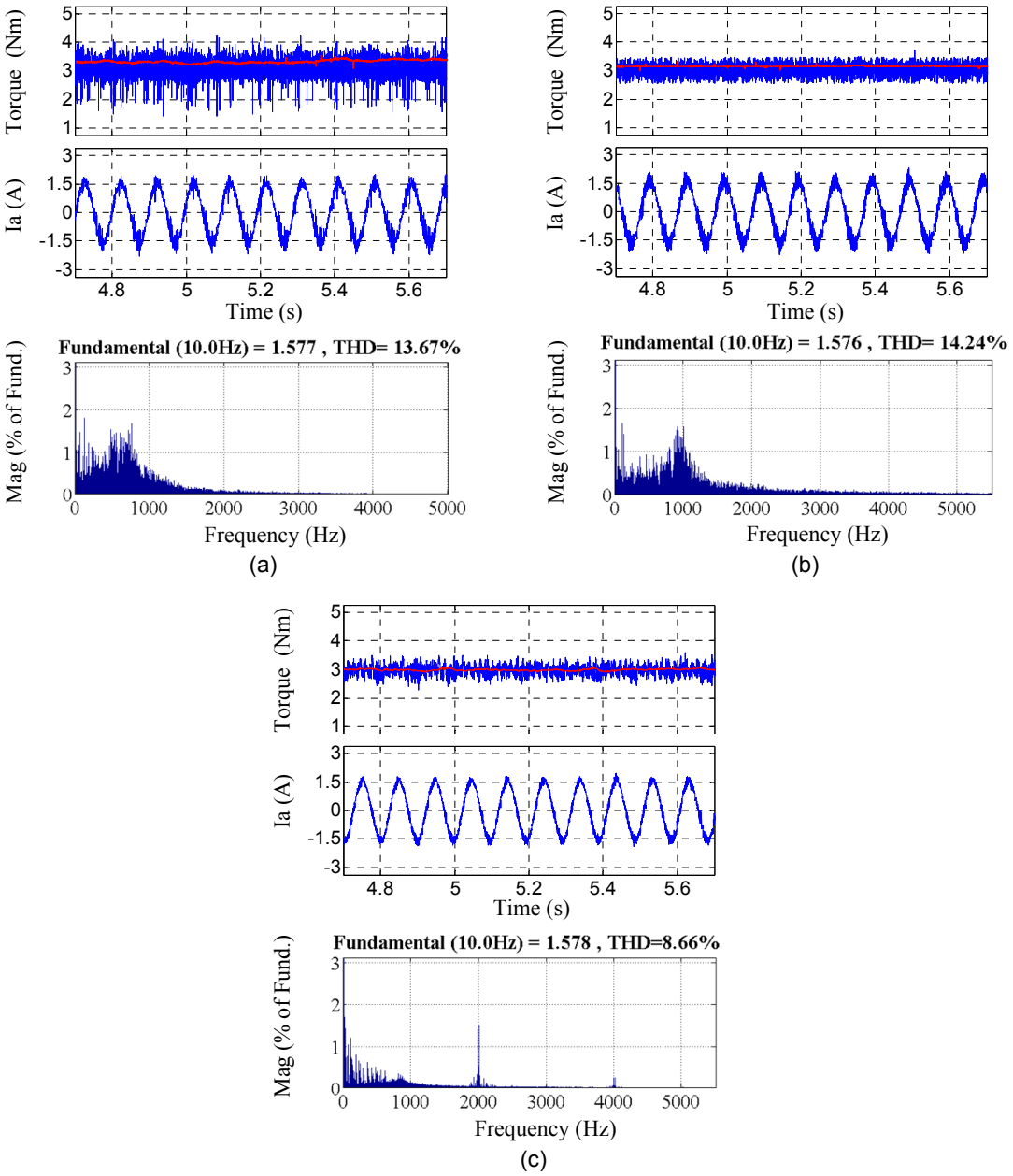

Figure 5.8: Steady-state response of the IPMSM at 300 rpm, 3 Nm. (a) Classical 3L-DTC (b) DDTC-1 (c) Proposed 3L-DTC showing torque response (top), stator current (middle) and harmonic spectrum of the stator current (bottom). (Reference values: red, Actual: blue).

can be attributed to the torque overshoots/undershoots caused by the large torque variation rates of the LVV/MVVs at these speeds.

In the case of proposed 3L-DTC, the PI controller output T_c^{err} will be regulated

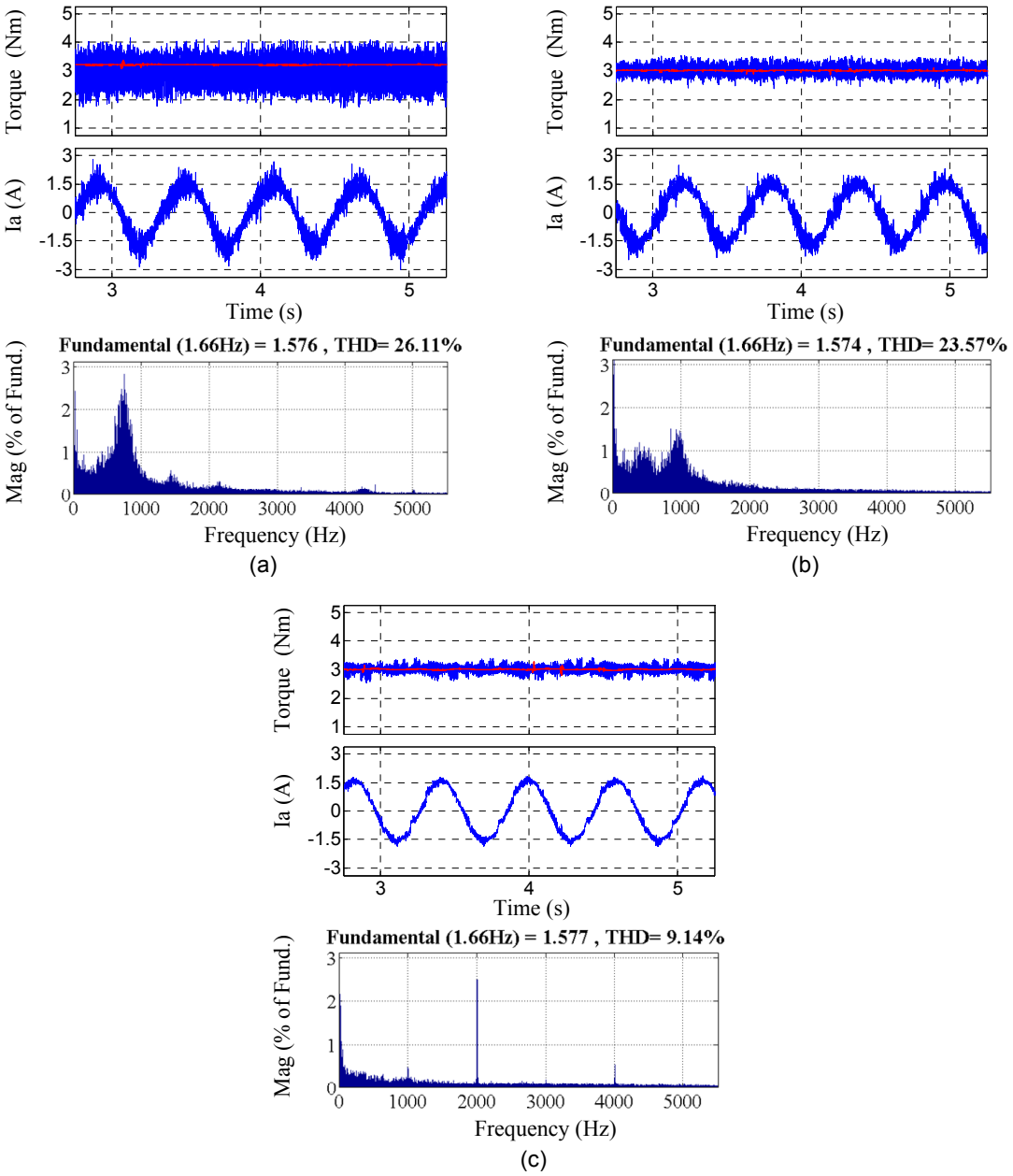

Figure 5.9: Steady-state response of the IPMSM at 50 rpm, 3 Nm. (a) Classical 3L-DTC (b) DDTC-1 (c) Proposed 3L-DTC showing torque response (top), stator current (middle) and harmonic spectrum of the stator current (bottom). (Reference values: red, Actual: blue).

to lie between T_p and 0. SVVs and ZVVs are proportionally applied, resulting in significant reduction of torque and flux ripples as presented in Fig. 5.10. In comparison to classical 3L-DTC, the reductions in torque and flux ripples are

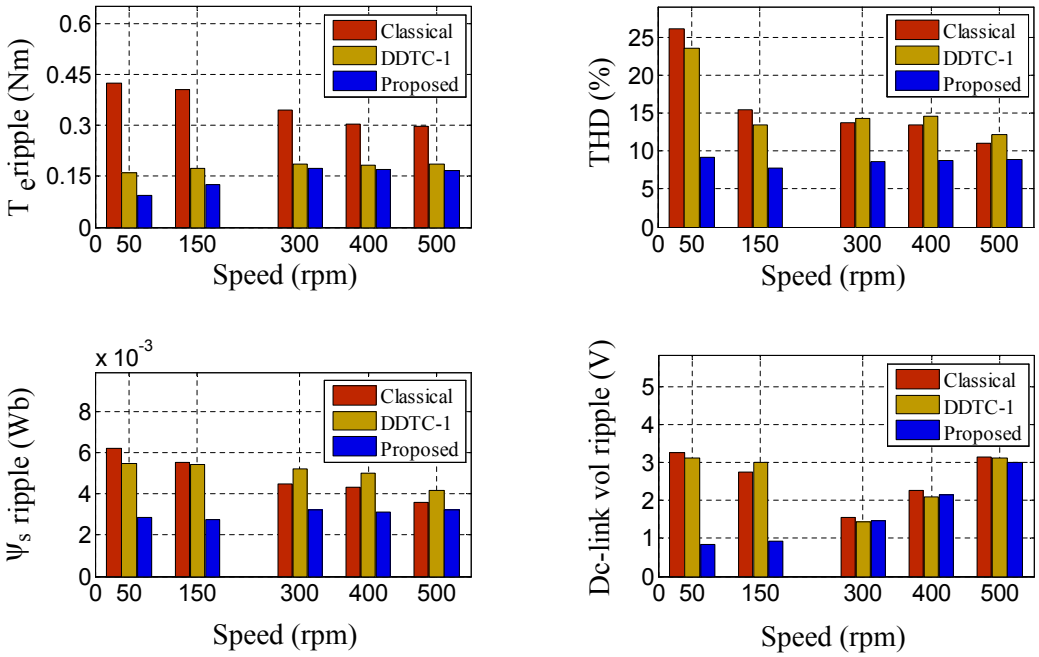

Figure 5.10: Steady state torque ripple, flux ripple, dc-link voltage ripple and stator current THD at different operating speeds with a load of 3 Nm.

69.35% and 50.2%, respectively. Consequently, significant improvement in THD of the output current is observed in Fig. 5.9(c).

The line to line voltages and the dc-link capacitor voltages corresponding to high, medium and low speed operations of the proposed 3L-DTC are presented in Fig. 5.11. It can be observed that smooth voltage vector switching criteria is respected. Besides, capacitor voltage fluctuations are approximately controlled to be within a band of ± 5 V.

For low speed operations, the utilization of mainly SVVs and ZVVs in the proposed 3L-DTC method indicates that voltage vector selection is limited to the inner hexagon of the 3L-NPC inverter voltage vector space. This is proven by the two-level line to line voltage seen in Fig.5.11, when the IPMSM is operating at the low speed of 150 rpm.

In contrast, low speed line to line voltages under the regulation of classical 3L-DTC and DDTC-1, as shown in Fig. 5.12, exhibit irregular switching patterns and three-level voltages. Consequently, the combined capacitor voltage ripples for

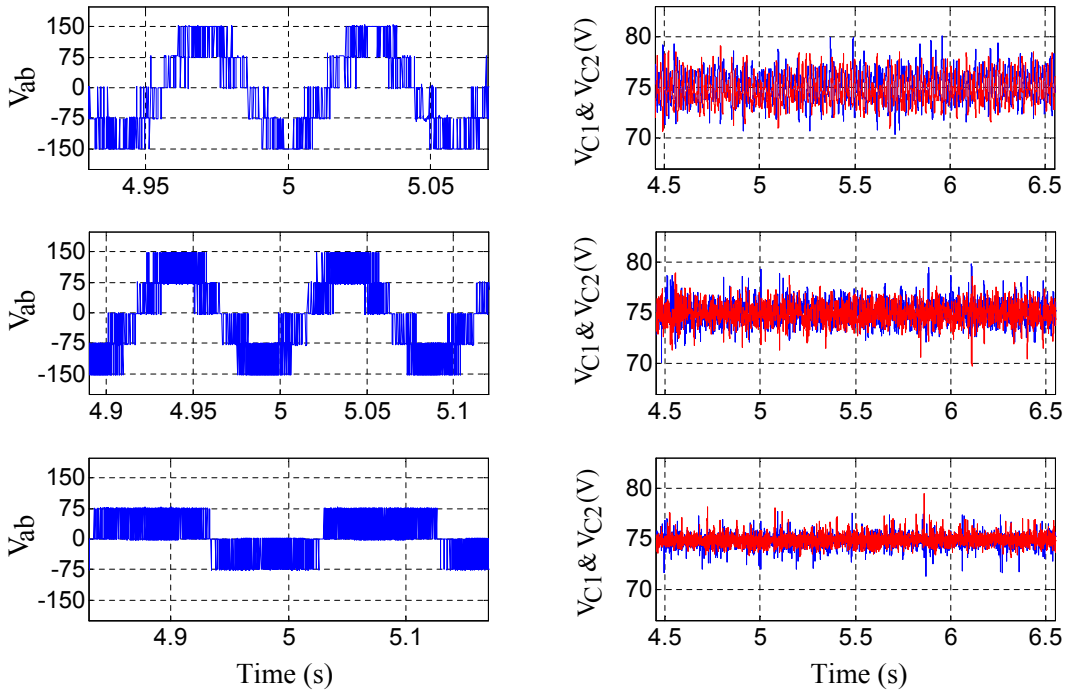

Figure 5.11: Zoomed-in line to line voltages and capacitor voltages fluctuations of the proposed 3L-DTC IPMSM drive at 500 rpm (top), 300 rpm (middle) and 150 rpm (bottom).

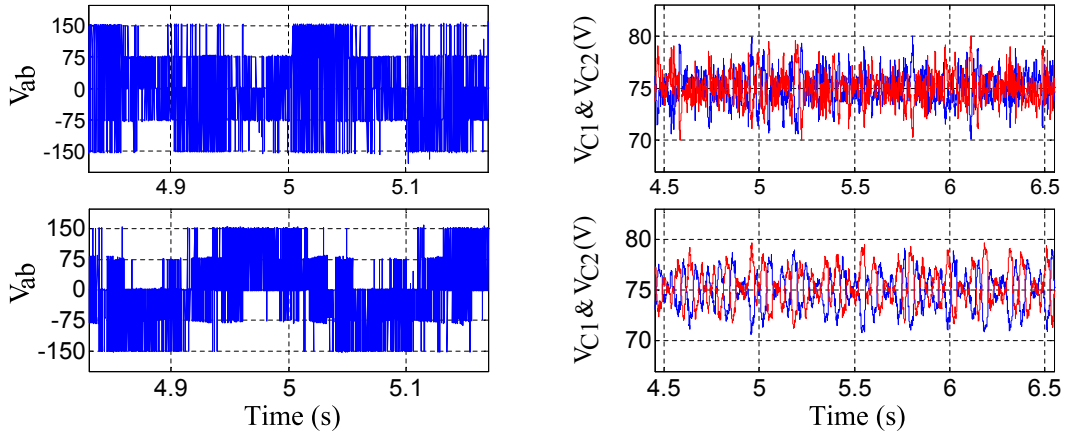

Figure 5.12: Zoomed-in line to line voltages and capacitor voltages fluctuations of the classical 3L-DTC (top) and DDTC-1 (bottom) drives at 150 rpm.

both methods are increased by a factor of approximately three, compared to the proposed method.

Lastly, the robustness of the proposed method is investigated by studying its

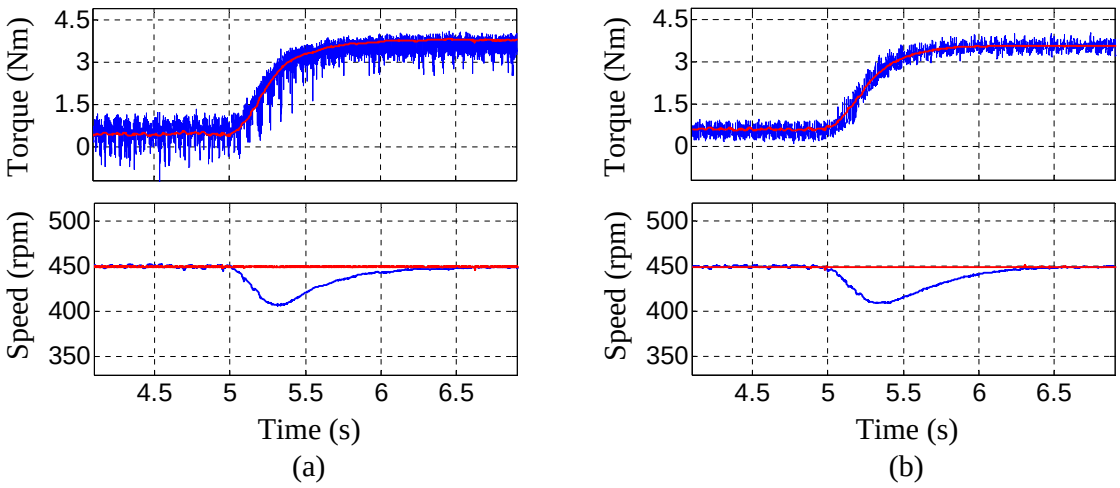

Figure 5.13: Torque and speed response of the IPMSM drive to external load disturbance for: (a) Classical 3L-DTC. (b) Proposed 3L-DTC.

dynamic response to external load disturbances. The results are illustrated in Fig.5.13. The motor is initially operating at a speed of 450 rpm with no load. A load of 3.5 Nm is subsequently applied to the motor at 5 s. Identical settling time of about 1.3 s is observed for both classical 3L-DTC and the proposed 3L-DTC algorithm.

In summary, based on the results presented in this section, it is clear that the proposed 3L-DTC algorithm improves the performance of a 3L-NPC inverter fed IPMSM drive under all operating conditions. Experimental results and the quantitative evidence presented in Fig. 5.10 have substantiated the superior performance of the proposed 3L-DTC over classical 3L-DTC and DDTC-1. Experimental results show that torque and flux dynamics generally deteriorate as the operating speed is decreased in classical 3L-DTC drives, which is reasonable, and can be attributed mainly to the speed dependent nature of torque variation rate.

On the other hand, DDTC-1 has been proven to be more or less equally efficient in minimizing torque ripples as the proposed method. Nevertheless, very little attention is paid to smooth voltage vector switching in this method, and it consistently exhibits poor flux control and high stator current THD. Besides,

similar to classical 3L-DTC, the switching frequency of DDTC-1 is variable and dependent on the operating conditions of the motor.

In the proposed 3L-DTC algorithm, the influence of torque variation rate is negated by the torque error regulating PI controller, which regulates the duty ratio of the applied voltage vectors. The manipulation of the duty ratios and the periodic nature of the applied voltage vectors, respecting the switching constraints of the 3L-NPC inverter, have ensured constant switching frequency and consistent dynamic performance under all operating conditions.

5.5.3 Parametric robustness of the torque controller

Torque controller gains K_p and K_i (5.15) are designed with the known values of stator resistance R_s and the quadrature-axis inductance L_q. Therefore, when the machine parameters vary, the designed controller gains will not be optimal. Consequently, torque response of the drive could be significantly affected if the proposed torque controller is not parametrically robust. To experimentally investigate the parametric robustness of the torque controller, the controller gains are detuned using the methodology discussed in the following subsections.

1. Variations in stator resistance R_s

By substituting the controller gains in (5.15) into (5.14), the closed loop transfer function the proposed torque regulator can also be expressed as

$$G(s) = \frac{\widetilde{T}_e(s)}{\widetilde{T}_e^*(s)} = \frac{\left(2\zeta_d\omega_{nd} - \frac{R_s}{L_q}\right)s + \omega_{nd}^2}{s^2 + 2\zeta_d\omega_{nd}s + \omega_{nd}^2} \tag{5.19}$$

Typically, in an IPMSM the known stator resistance $R_{s(kn)}$ will increase to a new actual resistance $R_{s(act)}$ due to the temperature increase in the machine. In other words, the resistance value used for controller design is usually smaller than the actual stator resistance of the IPMSM as it is operational, i.e., $R_{s(kn)} < R_{s(act)}$. Accordingly, the closed loop transfer function of the proposed torque controller

would be modified as

$$G(s) = \frac{\left(2\zeta_d\omega_{nd} - \frac{R_{s(kn)}}{L_q}\right)s + \omega_{nd}^2}{s^2 + s\left(2\zeta_d\omega_{nd} + \frac{1}{L_q}(R_{s(act)} - R_{s(kn)})\right) + \omega_{nd}^2} \tag{5.20}$$

By comparing the actual characteristic equation of (5.20) to the designed equation in (5.19), the following relations between the designed and actual values of the natural frequency $\omega_{n(act)}$ and damping ratio ζ_{act} can be found as

$$\omega_{n(act)} = \omega_{nd} \tag{5.21}$$

$$\zeta_{act} = \zeta_d + \frac{1}{2\omega_{n(act)}L_q}(R_{s(act)} - R_{s(kn)})$$

$$\zeta_{act} > \zeta_d \tag{5.22}$$

Equation (5.21) shows that the natural frequency remains the same (i.e., K_i is unchanged). Consequently, it can be acknowledged that the variations in R_s will have no impact on the natural frequency of the torque regulator.

On the other hand, the actual damping ratio as shown in (5.22) is increased by the term $(2\omega_{nd}L_q)^{-1}(R_{s(act)} - R_{s(kn)})$. As the damping ratio is increased, the actual transient response of the system would be affected; the percentage overshoot ($OS\%$) and the settling time T_{st} will reduce, albeit marginally since the term $(2\omega_{nd}L_q)^{-1}(R_{s(act)} - R_{s(kn)})$ is usually very small. Consequently, negligible improvements in transient responses are noted in Fig. 5.14 as the controller is detuned for +25% and +50% variation in stator resistance.

2. Variations in quadrature inductance L_q

Similarly, for variation in known quadrature inductance $L_{q(kn)}$ to a new actual value $L_{q(act)}$, the closed loop transfer function would be modified to

$$G(s) = \frac{B\left[\left(2\zeta_d\omega_{nd} - \frac{R_s}{L_{q(kn)}}\right)s + \omega_{nd}^2\right]}{s^2 + sB2\zeta_d\omega_{nd} + B\omega_{nd}^2} \tag{5.23}$$

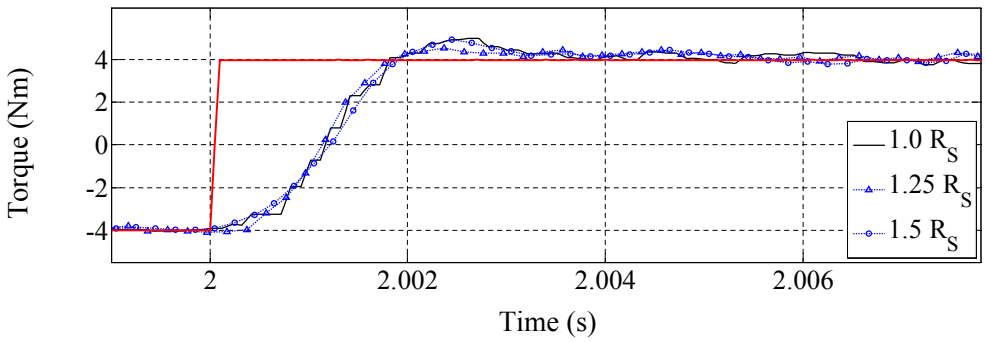

Figure 5.14: Torque responses with detuning of stator resistance in experiments.

where B denotes $L_{q(kn)}/L_{q(act)}$. Typically in an IPMSM, $L_{q(kn)} > L_{q(act)}$. i.e., $B > 1$. Then, the relations between the actual and designed natural frequency and the damping ratio can be derived by comparing the characteristic equations of (5.23) and (5.19) as

$$\omega_{n(act)}^2 = \frac{L_{q(kn)}}{L_{q(act)}}\omega_{nd}^2 = B\omega_{nd}^2$$

$$\omega_{n(act)} > \omega_{nd} \tag{5.24}$$

$$\zeta_{act} = \frac{L_{q(kn)}}{L_{q(act)}}\frac{\omega_{nd}}{\omega_{n(act)}}\zeta_d = \frac{\omega_{n(act)}}{\omega_{nd}}\zeta_d = \sqrt{B}\zeta_d$$

$$\zeta_{act} > \zeta_d \tag{5.25}$$

From (5.24) and (5.25), it can be observed that the actual natural frequency and damping ratio are increased by a factor of $B^{0.5}$. As a result, $OS\%$ and T_{st} are reduced (i.e., K_p and K_i are increased). In other words, when L_q of the IPMSM varies to a lower value, faster torque dynamics can be expected.

The experimental transient torque responses when the rated L_q is detuned by -10% and -20% are presented in Fig 5.15. For the variation in L_q, the improvement in transient toque response is clearly noticeable with smaller rise-time and overshoot. This is because the natural frequency and damping ratio are both increased by a factor of $B^{0.5}$.

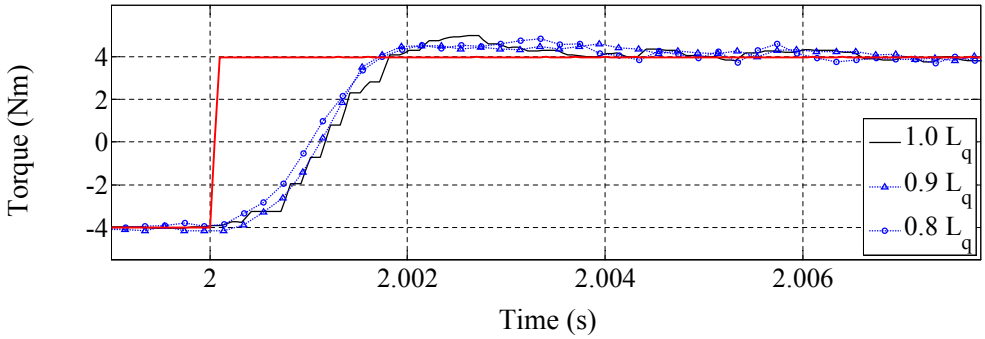

Figure 5.15: Torque responses with detuning of quadrature inductance in experiments.

Experimental results presented in this subsection have shown that the torque responses of the proposed 3L-DTC drive are influenced by the variations in machine parameters. However, the differences noted in transient responses are rather inconsequential, especially considering the significant detuning that was introduced in the experiments. Furthermore, it is clearly noticeable that there is hardly any difference in torque responses during steady state operation. Therefore, it can be concluded that the proposed method is adequately robust against possible variations in machine parameters.

5.6 Conclusion

A constant switching frequency based 3L-DTC algorithm for 3L-NPC inverter driven IPMSMs has been presented in this chapter. In the proposed method a torque regulator consisting of one PI controller and four triangular carriers is introduced to replace the conventional torque hysteresis controller.

The PI controller reshapes and smoothens the large slopes of torque while the constant inverter switching within each sampling period is attained by using triangular carriers that operate at the desired switching frequency. Consequently, two voltage vectors are applied sequentially within each sampling cycle and this helps to improve the torque and flux regulation.

To aid in the design procedure and to analyze the stability of the proposed

torque regulator, small-signal model of the torque control loop is developed. Based on this, detailed design guidelines are provided for the proposed torque regulator.

The performance of the proposed 3L-DTC drive is experimentally compared to classical 3L-DTC and an existing DDTC method in the literature. Results show that the proposed method contributes to significantly reduce torque ripples and THD of the stator current while attaining constant switching frequency and smooth voltage vector switching.

The gains of the proposed torque regulator are undoubtedly machine parameter dependent and therefore, the gains might not be optimal when the parameters vary. In order to study the parametric robustness of the proposed torque regulator, controller gains are detuned in experiments according to the theoretical analysis presented. Experimental results are provided to discuss the sensitivity of the proposed torque regulator to possible variations in the machine parameters.

Chapter 6

Generalized Constant Inverter Switching Frequency Based DTC Strategy for IPMSM

6.1 Motivation and Objectives

The integration of multilevel inverters (MLIs) into DTC drives has been receiving increased attention from researchers in the recent years. In addition to the well documented advantages of MLIs, the increased degree of freedom in the context of DTC means that the rotational speed of stator flux can be more precisely controlled in MLI fed DTC (MLI-DTC) drives to improve the regulation of torque and flux.

The 3L-NPC inverter is the most commonly used inverter in MLI-DTC drives. A number of MLI-DTC algorithms have also been reported in the literature for MLIs with more than three voltage levels. Nevertheless, a common theme among the proposed MLI-DTC algorithms, including the 3L-DTC algorithms proposed in Chapters 3, 4 and 5 of this thesis, is that they are mostly inverter specific. In other words, the hysteresis controllers and switching tables are tailored to the specific voltage level of the inverter used. Consequently, these MLI-DTC approaches are not readily applicable to generic n-level inverter fed DTC drives.

An important aspect of the inverter specific MLI-DTC is that the complexity in implementing DTC concepts will increase proportionally with the increase in

number of voltage vectors. This is unavoidable if the extra degree of freedom in MLI-DTC is to be fully exploited.

For instance, a typical 2L-DTC setup for PMSM drives uses a two-level torque and flux hysteresis control with six sector divisions to utilize the six active vectors of the two-level inverter. In comparison, the five-level inverter fed DTC in [94] uses three-level hysteresis control for torque and flux with twelve sector divisions and five separate switching tables to utilize the full depth of available voltage vectors. This clearly introduces a significant increment in complexity, which can get even more challenging if inverter inherent switching limitations are to be strictly addressed.

Therefore, it is desirable to have simple structured generalized MLI-DTC algorithms that respect the inverter switching constraints while being readily applicable to generic inverters with any number of voltage levels. In addition, as MLIs are typically intended for use in medium to high power drives, MLI-DTC algorithms should operate with low average inverter switching frequency while maintaining the ripples in torque and flux to an acceptable level.

A handful of MLI-DTC algorithms reported in the literature are generic in nature [95]–[99]. The proposed seven-level hybrid CHB fed DTC drive in [94] is an extension of classical DTC concept to MLI-DTC using the vector decomposition method proposed in [94]. As a single voltage vector is applied during each sampling cycle based on fixed band hysteresis control, high ripples in torque and flux and a variable inverter switching frequency is inevitable. Conversely, the methods in [97], [98] and [99] employs predictive control to apply two voltage vectors within each sampling period to impose a constant switching frequency and reduce the torque ripples. Nevertheless, the use of predictive model makes the accuracy of the proposed methods highly susceptible to possible variations in the machine parameters.

To resolve these problems, a novel MLI-DTC method that is parametrically robust and yet, capable of operating at constant and low switching frequency with

reduced ripples in torque and flux is proposed in this chapter. The proposed MLI-DTC method is essentially an improvisation of the proposed constant switching frequency based 3L-DTC method in Chapter 5; it has the same basic structure as the 3L-DTC method in Fig. 5.1, but the peripherals of the torque regulator are modified to accommodate to generic n-level inverters.

Subsequently, two voltage vectors are applied sequentially in one switching cycle and this leads to an imposition of constant inverter switching and improved regulation of stator voltage which alleviates the torque and flux ripples in the drive. Moreover, as proved by the design analysis and the experimental results, the proposed generalized MLI-DTC method shows excellent transient dynamics and robustness against the variations in the machine parameters, thus maintaining the merits of the classical DTC.

The rest of this chapter is structured as follows. In Section 6.2, vector decomposition technique and the voltage vector selection strategy for the proposed MLI-DTC are discussed. The switching sequence acceleration technique used in the proposed MLI-DTC to improve the transient performance of the proposed MLI-DTC drive is introduced in Section 6.3 while the design guidelines for the improvised torque regulator are provided in Section 6.4. Experimental results and comparative analysis against the generalized MLI-DTC in [95], [96] are presented in Section 6.5 to confirm the efficacy of the proposed method. In addition, sensitivity analysis of the torque regulator is carried out in Section 6.5 to investigate the parametric robustness of the proposed method.

6.2 Proposed Generalized MLI-DTC Algorithm

6.2.1 DTC for n-level inverter

In general, an n-level inverter will generate $3n(n-1)+1$ space vectors in the stationary $\alpha-\beta$ frame while the total number of switching states will be n^3. In the proposed MLI-DTC, a vector decomposition technique is used to simplify the

voltage vector selection process, so that the vector selection can be determined in a similar way as in two-level inverter fed DTC (2L-DTC).

For instance, Fig. 6.1 shows the space vector diagram of a five-level inverter in the $\alpha - \beta$ plane. The vector space in Fig. 6.1 can also be seen as a composition of several sub-hexagons (sh) with each sub-hexagon comprised of seven voltage vectors with one at the center and six on the perimeter, which is identical to the vector space used in typical 2L-DTC drives. For an n-level inverter, the total number of sub-hexagons will be $3n(n-3)+7$.

In classical DTC drives, one voltage vector is typically applied during an entire sampling period T_s. As such, the vector that is applied at the start of the current sampling period at $t = T_0$ can be considered to be at the center of the current active sub-hexagon. Subsequently, based on the torque and flux requirements and the approximation of stator flux location through a sector division of 60° (see Fig. 6.1), the voltage vector to be applied at the start of next switching period ($t = T_0 + T_s$) can be determined using the classical 2L-DTC vector selection principles illustrated in Fig. 6.1. This implies that the voltage vector selection will be limited to the six adjacent voltage vectors, thus satisfying the MLI switching constraint of switching transition between adjacent voltage vectors [63], [87].

Inverter saturation occurs when the active sub-hexagon is near the edges of the vector space as shown in Fig. 6.2. Under such circumstances, some of the voltage vectors selected according to classical 2L-DTC switching principles cannot be attained by the inverter. Therefore, the vector selection criteria must be modified to select new vectors which should influence the torque and flux dynamics as closely as possible to the originally selected vectors. Fig. 6.2 illustrates two examples (marked as I and II) when the active sub-hexagon is at the top right corner of the $\alpha - \beta$ vector space as the stator flux vector ψ_s is in sectorS_1. In the first instance, $v_{sh,3}$ is selected according to DTC principles for an increase in torque and decrease in flux. However, $v_{sh,3}$ is unattainable, and therefore, the nearest displacement vector $v_{sh,4}$ must be selected instead.

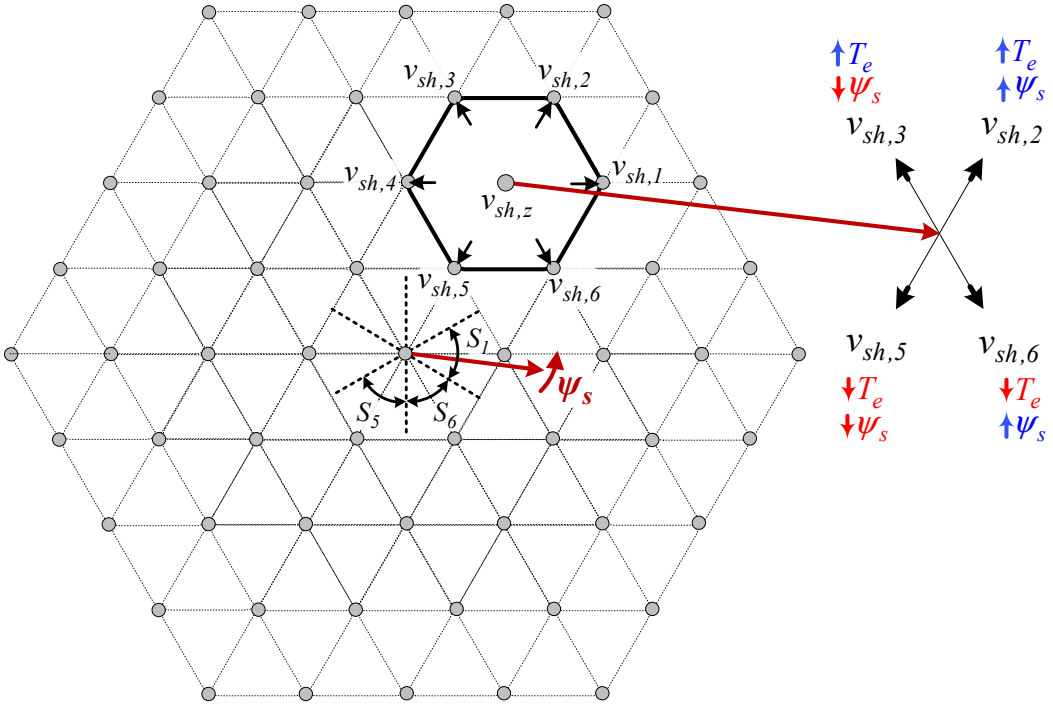

Figure 6.1: Space vector diagram of a five-level inverter in the $\alpha - \beta$ plane with $3n(n-3)+7$ sub-hexagons (sh) and $3n(n-1)+1$ voltage vectors which corresponds to the dots.

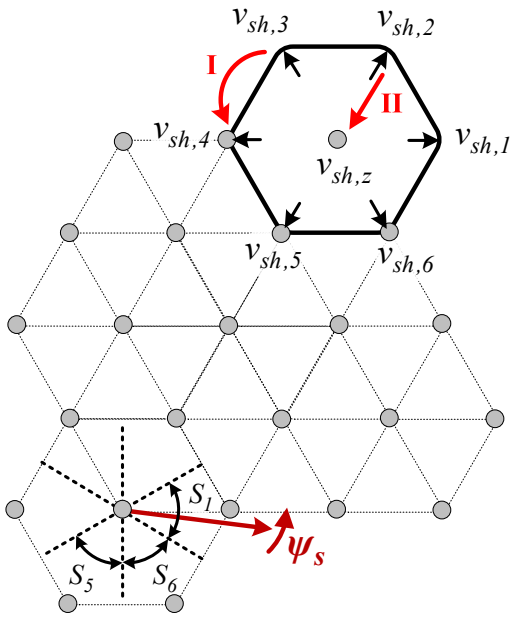

Figure 6.2: Two examples (I and II) of inverter saturation and the subsequent modifications in vector selection, as indicated by red arrows.

In the second instance, vector $v_{sh,2}$ will be unavailable when the demand is for an increase in both torque and flux. In this case, the selection of nearest possible vectors $v_{sh,4}$ and $v_{sh,6}$ will produce an almost opposite effect on the desired torque and flux dynamics. Therefore, the vector $v_{sh,z}$ should be retained and applied again during the next sampling cycle.

6.2.2 Torque ripple reduction strategy

A constant switching frequency is imposed in the proposed method by using a torque regulator as shown in Fig. 6.3. The torque regulator comprises of a PI controller and two triangular carrier fed comparator units. The function of the PI controller is to reduce the influence of large and varying torque slopes which contribute mainly to the poor torque regulation in the IPMSMs. The smoothed PI controller output T_c^{err} is limited to $\pm T_p$ and reflects the instantaneous torque demand. When the torque demand is positive, T_c^{err} will lie between T_p and 0. Similarly, when the instantaneous torque demand is negative, T_c^{err}will be between 0 and $-T_p$.

The output of the PI controller is compared separately to the positive and negative triangular carriers. Subsequently, the comparator outputs are added up to produce a pulse width modulated (PWM) output which is analogous to a three-level torque hysteresis controller output ($\epsilon_T = \pm 1, 0$). In general, the states "$+1$" and "-1" refer to positive and negative torque demand, respectively, while "0" indicates that the torque error is within the acceptable margins.

When the torque demand is positive, the comparator unit will produce an output that toggles between states $+1$ and 0 within one switching cycle T_{carr} (see Fig. 6.3). Similarly, when the torque demand is negative, the comparator output will toggle between states -1 and 0. For the duration of time $D_{act}T_{carr}$, when the comparator output is either $+1$ or -1, an active vector would be applied to meet the instantaneous torque demand.

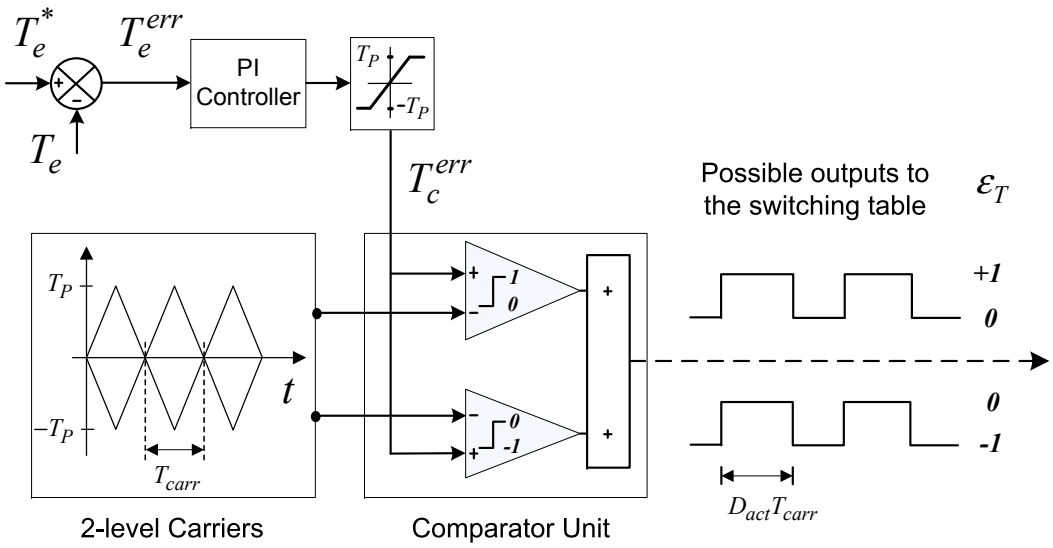

Figure 6.3: Proposed torque regulator for MLI-DTC.

Then, for the rest of the switching cycle $(1 - D_{act})T_{carr}$, when the comparator output is 0, a passive vector will be applied to minimize the exertion of torque beyond its reference. The sequential application of two voltage vectors within one carrier cycle will enable: 1) constant inverter switching; 2) a reduction in torque and flux ripples as the stator voltage vector v_s is modified.

In MLIs, there are a number of switching states that can be mapped onto identical voltage vectors in the $\alpha - \beta$ plane. These vectors are usually referred to as redundant switching states which increase dramatically with the number of levels of the inverter. In the proposed MLI-DTC algorithm, switching state redundancy is used to achieve dc-link voltage balancing, if it is applicable. If dc-link voltages are maintained within the desired bands, then, the redundancy of vectors is used to minimize the number of switching commutations.

6.2.3 Selection of active and passive voltage vectors

At the start of each switching period, one sub-hexagon in the voltage vector space in the α-β plane will be active. The vector at the center of this active sub-hexagon will be analogous to a zero voltage vector in the classical 2L-DTC.

Therefore, the vector at the center of the active sub-hexagon is chosen as the passive vector in the proposed MLI-DTC. Then, the active vector is selected from the six vectors that lie on the perimeter of the active sub-hexagon using the well-established 2L-DTC vector selection principles depicted in Fig. 6.1. In other words, the passive voltage vector selected during the current switching period is, in fact, the active voltage vector used during the previous switching period.

6.3 Switching Sequence Acceleration (SSA)

The proposed voltage vector selection procedure described in the previous section limits the switching transitions to adjacent voltage vectors. These switching constraints, which are necessary to safeguard the inverter and decrease the THD of the output currents, could nevertheless affect the torque dynamics of the proposed MLI-DTC during large torque transients; for instance, during a speed reversal. The deterioration of transient torque dynamics in the proposed MLI-DTC drive would be negligible if a large switching frequency is used, i.e., small T_{carr}. However, the proposed MLI-DTC algorithm is targeted for use in medium to high power drives, and therefore, should be designed to operate with low inverter switching frequency.

A graphical illustration of normal switching transition in the proposed MLI-DTC is shown in Fig. 6.4(a). For the scenario depicted in Fig. 6.4, it is assumed that at $t < 0$, the active voltage vector is v_z and the stator flux vector is in sector S_1 Also, for the ease of explanation, an unchanged positive flux demand is assumed.

Now, if there is a sudden positive torque demand or in other words, a large positive torque error, the ideal voltage vector to achieve the fastest change in torque dynamics would be $v_{k(3)}$. However, the application of $v_{k(3)}$ will violate the inverter switching constraints. Therefore, the switching sequence in the proposed MLI-DTC would follow the sequence shown in Fig. 6.4(a) as the PI controller output T_c^{err} would be fixed to T_p and the duty ratio of the active vector D_{act} will be unity.

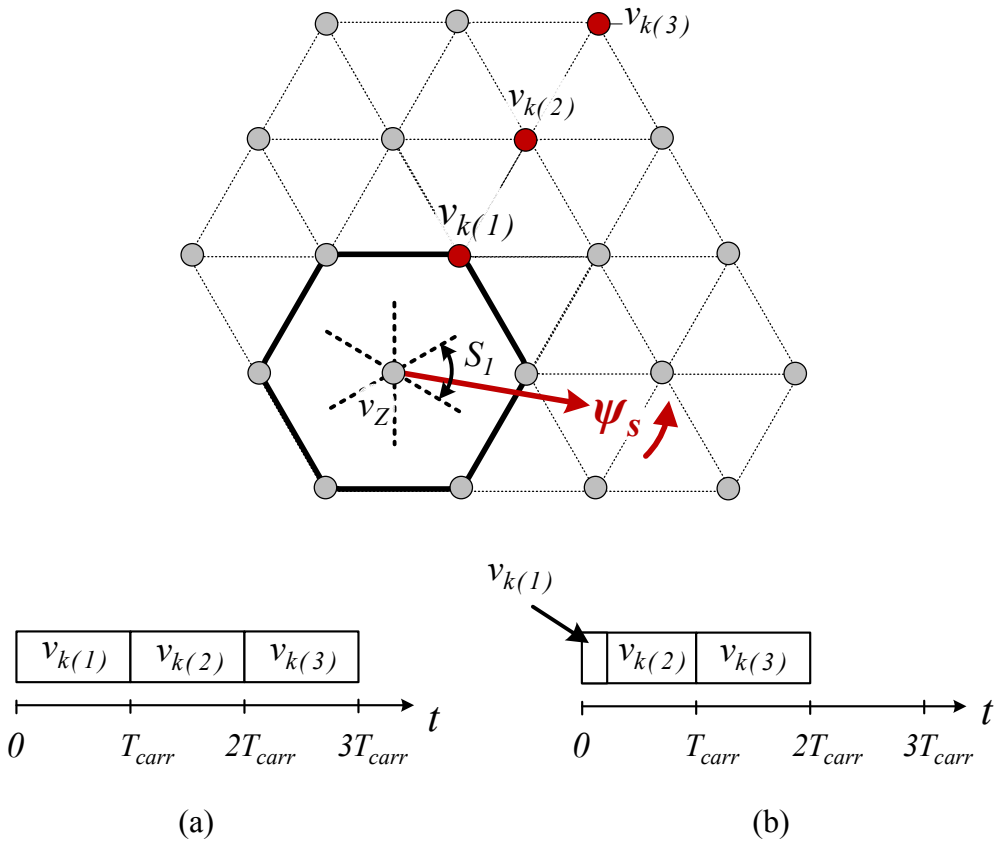

Figure 6.4: Switching sequence in the proposed MLI-DTC. (a) Without switching sequence acceleration. (b) With switching sequence acceleration.

In order to quicken the switching transition to the optimal voltage vector, a switching sequence acceleration (SSA) technique is included in the proposed MLI-DTC algorithm as shown in Fig. 6(b). The accelerated switching sequence is used whenever there is a large transient torque demand, which can be detected by the saturation of T_c^{err} ($|T_c^{err}| = |T_p|$). The selected active vector ($v_{k(1)}$ in Fig. 6.4(b)) will be applied first for a minimum fixed duration considering the dead-time used for the inverter. For instance, a dead-time of 3 μs is used for the experiments in this thesis; therefore, a reasonable duration of the first active voltage vector would be 3% of the T_{carr} for the proposed MLI-DTC drive in this chapter.

For the rest of the switching period, a second voltage vector, the vector that would typically be selected as the active vector for the next switching cycle ($v_{k(2)}$ in Fig. 6.4), would be used. This second vector can be easily determined by

assuming that the active sub-hexagon has moved adjacently towards the selected active vector used.

From the illustration in Fig. 6.4, it can be envisioned that the larger the number of levels n in an MLI, the longer the transition time for reaching the optimal voltage vector. This is especially true during large torque transients. Therefore, it can be reasoned that the significance of SSA's contribution would increase proportionally with the number of levels in an MLI.

6.4 Design of Torque Regulator

Design criteria of the proposed torque regulator are developed through the linearization of the torque control loop using small-signal modeling, similar to the methodology adopted for the proposed 3L-DTC algorithm in Chapter 5 (see Section 5.3).

6.4.1 Average torque variation rate

Based on the vector decomposition technique used in the proposed MLI-DTC, the torque slope of the active voltage vector for an n-level inverter can be derived by referring to (5.4) as

$$\rho T_{e,active} = -\frac{R_s}{L_q} T_e + \frac{3P}{2L_q}\Big(\frac{1}{n-1} v_s - |\psi_s|\omega_{re}\Big)\psi_r \tag{6.1}$$

where n denotes the number of voltage levels in the MLI used.

As explained previously, the selected passive vectors can be considered to be analogous to a zero voltage vector ($v_s = 0$). Therefore, the torque slope of the passive vectors is simply

$$\rho T_{e,passive} = -\frac{R_s}{L_q} T_e + \frac{3P}{2L_q}|\psi_s|\omega_{re}\psi_r \tag{6.2}$$

By substituting (6.1) and (6.2) into (5.5), the average torque slope in a switching period can be expressed in terms of the duty ratio of the active vector D_{act}

as

$$\rho T_{e(avg)} = D_{act}\Big[-\frac{R_s}{L_q}T_e + \frac{3P}{2L_q}\Big(\frac{1}{n-1}v_s - |\psi_s|\omega_{re}\Big)\psi_r\Big] + (1-D_{act})\Big[-\frac{R_s}{L_q}T_e - \frac{3P}{2L_q}|\psi_s|\omega_{re}\psi_r\Big]$$

$$= -\frac{R_s}{L_q}T_e + \frac{3P}{2L_q}\psi_r\Big(\frac{D_{act}}{n-1}v_s - |\psi_s|\omega_{re}\Big) \tag{6.3}$$

6.4.2 Small-signal control-to-output transfer function

In order to linearize the torque control loop, the state variables T_e and D_{act} must be subdivided into a DC component and a small AC perturbation (5.10)-(5.11). By substituting (5.10) and (5.11) into (6.3), and after separating the AC components, the piecewise linearized expression for the proposed for the torque regulator can be derived as

$$\rho\widetilde{T}_e = -\frac{R_s}{L_q}\widetilde{T}_e + \frac{3P\psi_r v_s}{2L_q(n-1)}\widetilde{D}_{act} \tag{6.4}$$

Applying Laplace transform to (6-4), the control-to-output transfer function of the torque regulator can be expressed as

$$\widetilde{T}_e(s) = \frac{3P\psi_r v_s}{2L_q(n-1)\Big(s+\frac{R_s}{L_q}\Big)}\widetilde{D}_{act}(s) \tag{6.5}$$

The resultant closed-loop model of the proposed torque control loop is shown in Fig. 6.5, where K_p and K_i represent the proportional and integral gains of the torque PI controller, respectively.

6.4.3 Design guidelines for PI controller

By comparing the control-to-output transfer function in (6.5) to (5.13), it is clear that the open loop gain of the torque regulator in MLI-DTC is modified by the voltage level n of inverter used. From Fig. 6.5, the closed-loop transfer

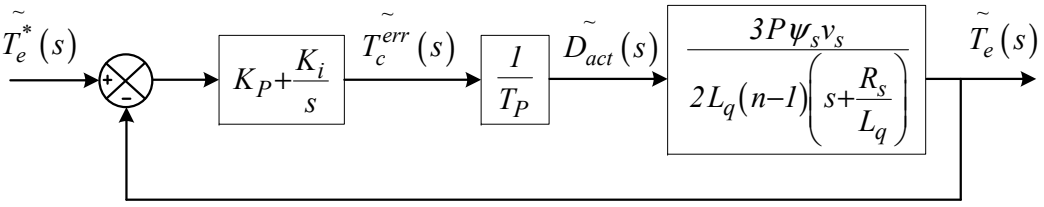

Figure 6.5: Closed-loop block diagram of torque control in the proposed MLI-DTC drive.

function of proposed torque regulator in the standard second-order form can be derived as shown in (6.6).

$$G(s) = \frac{\widetilde{T}_e(s)}{\widetilde{T}_e^*(s)} = \frac{A(K_p s + K_i)}{s^2 + s(AK_p + \frac{R_s}{L_q}) + AK_i} \tag{6.6}$$

where $A = \frac{3P\psi_r v_s}{(n-1)2L_q T_p}$.

From (6.6), it can be observed that the gains of the PI controller are influenced by the voltage level of the inverter used. Consequently, by using the same methodologies recommended in Chapter 5 (see Section 5.3), the PI controller gains can be carefully selected by the designer according to the desired transient response. It is also important to ensure that the absolute slope of the PI controller output T_c^{err} does not exceed the absolute slope of the carrier signals and therefore, the proportional gain of the PI controller should adhere to (5.18).

6.5 Experimental Results

In this section, the transient and steady state performance of the proposed MLI-DTC algorithm is compared to that of the generalized classical MLI-DTC method proposed in [95], [96], which is referred to as CMLI-DTC in the continuation of this chapter for simplicity. For all experiments, the setup of 3L-NPC inverter fed IPMSM drive as depicted in Fig. 3.11 is used.

In the experiments, the proposed torque regulator operates with a switching frequency of 2 kHz. To ensure a fair comparison, the sampling frequency of CMLI-DTC is fixed to 20 kHz which results in an average switching frequency of about

Table 6.1: Optimized torque regulator gains for the proposed MLI-DTC

K_p 14.5	K_i 10500	T_p 40

1.92 kHz. For both DTC algorithms, the band for flux hysteresis controller is set to 2% of the rated flux while the torque hysteresis band for CMLI-DTC is fixed to 10% of the rated torque. The torque regulator gains used in the experiments are given in Table 6.1.

6.5.1 Transient performance

In order to examine the transient torque dynamics of the proposed torque control, zoomed-in torque responses during torque reversal from -4 Nm to $+4$ Nm, at standstill, are shown in Fig. 6.6. The dynamic response of CMLI-DTC is approximately 1.9 ms while the response of the proposed MLI-DTC with SSA is slightly slower by about 0.2 ms, mainly due to the damping effect of the proposed torque PI controller.

The significance of the SSA technique is also noticeable in Fig. 6.6. It can be seen that without SSA, the initial torque response is sluggish. Consequently, the torque reversal response is about 0.7 ms or about 36% slower than the CMLI-DTC, which is significant considering that a three-level MLI is used for the experiments.

6.5.2 Steady state performance

Experiments were carried out at different operating speeds to investigate the steady state performances. Figs. 6.7-6.12 show the steady state torque, stator current and its THD when the IPMSM is operating at 90%, 20% and 5% of the rated speed with a load torque of 4 Nm. The numerical comparisons of the experimental results are presented in Fig. 6.13 in which the torque and flux ripples are calculated using (3.20). For determining the THD of the stator current, the maximum frequency used is 5.5 kHz.

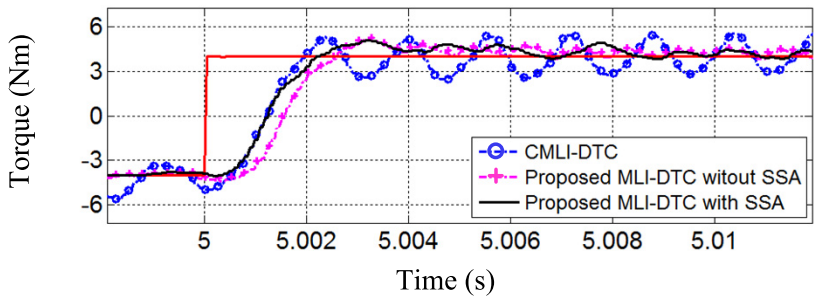

Figure 6.6: Zoomed in torque responses during torque reversal.

From the results presented in Fig. 6.7-6.12, it is clear that the proposed MLI-DTC consistently outperforms the CMLI-DTC in terms of torque and flux regulation and the THD in the stator current. It can be observed in Figs. 6.7, 6.9 and 6.11 that the torque ripples of the CMLI-DTC are well beyond the used hysteresis bands ($\pm$0.5 Nm) due to the application of a single voltage vector in each switching cycle. In contrast, the smoothing of torque slope and the sequential application of two voltage vectors in one switching cycle result in significant reduction of torque ripples with the proposed MLI-DTC.

When compared to the CMLI-DTC, the average reduction in torque ripples attained by the proposed MLI-DTC is about 66.8%. It is also evident in Fig. 6.13 that the torque ripples of the CMLI-DTC increase as the operating speed decreases, which concurs with the varying nature of torque slope (8). In contrast, an opposite effect is seen with the torque ripples of the proposed MLI-DTC. This can be attributed to the increased duty cycle regulation at lower speeds. At higher speeds, the duty ratio of the active vector needs to be high to overcome the large back e.m.f of the motor, and hence, torque ripple reduction is less effective.

Although the same hysteresis bands are used for flux control, the overall reduction noted for flux ripples is about 36.6% with the proposed MLI-DTC. It is well accepted that the THD in the stator current is heavily influenced by the ripples in the stator flux and, to a lesser extent, by the torque ripples [36].

Consequently, the average THD of the stator current is kept below 15% with the proposed MLI-DTC drive. In contrast, the THD of the CMLI-DTC is significantly

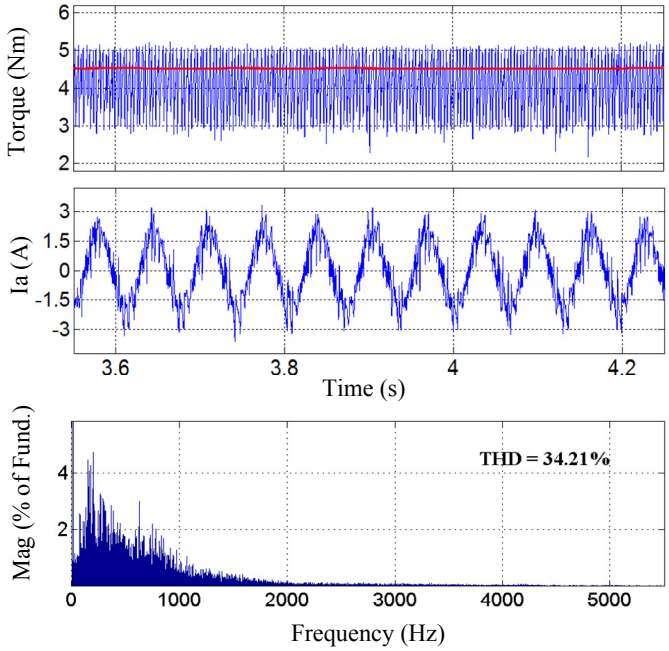

Figure 6.7: Steady state responses of the CMLI-DTC at 450 rpm, 4 Nm with torque response (top), stator current (middle) and harmonic spectrum of the stator current (bottom).

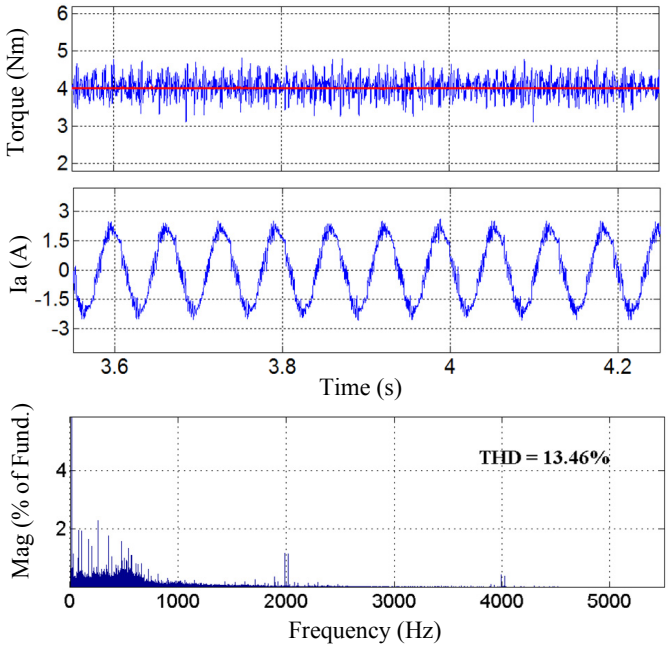

Figure 6.8: Steady state responses of the proposed MLI-DTC at 450 rpm, 4 Nm with torque response (top), stator current (middle) and harmonic spectrum of the stator current (bottom).

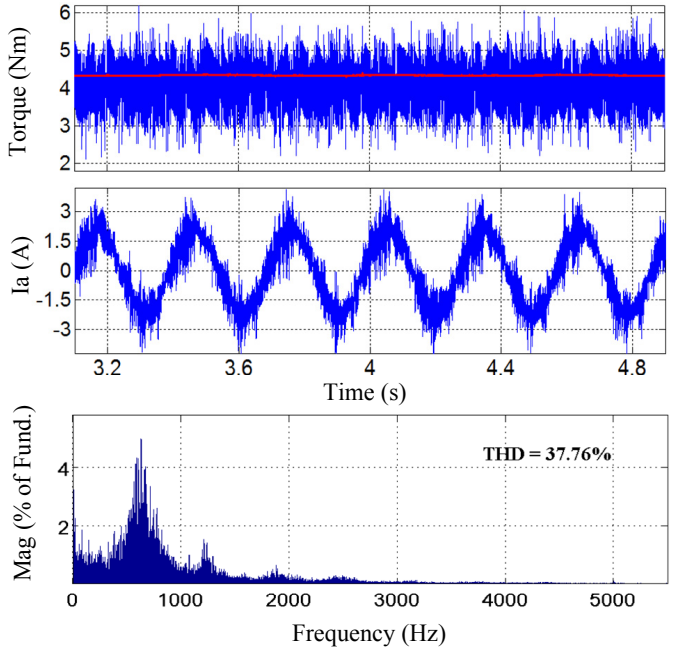

Figure 6.9: Steady state responses of the CMLI-DTC at 100 rpm, 4 Nm with torque response (top), stator current (middle) and harmonic spectrum of the stator current (bottom).

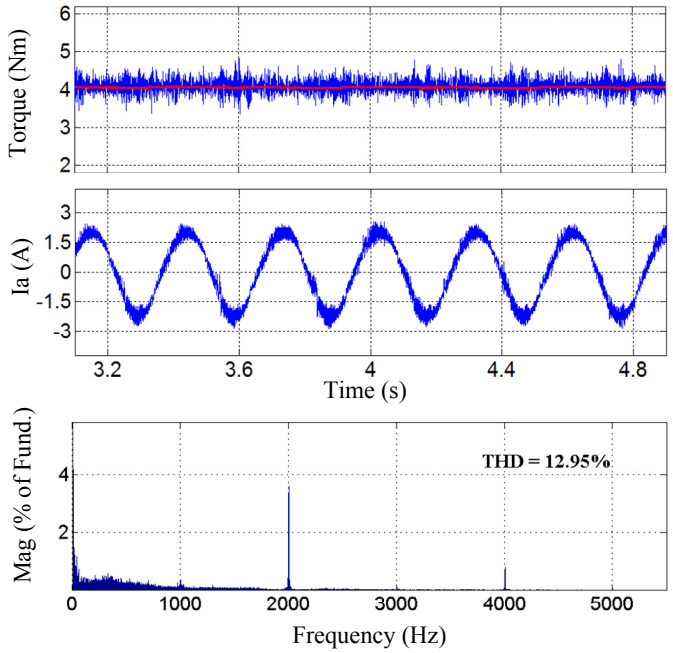

Figure 6.10: Steady state responses of the proposed MLI-DTC at 100 rpm, 4 Nm with torque response (top), stator current (middle) and harmonic spectrum of the stator current (bottom).

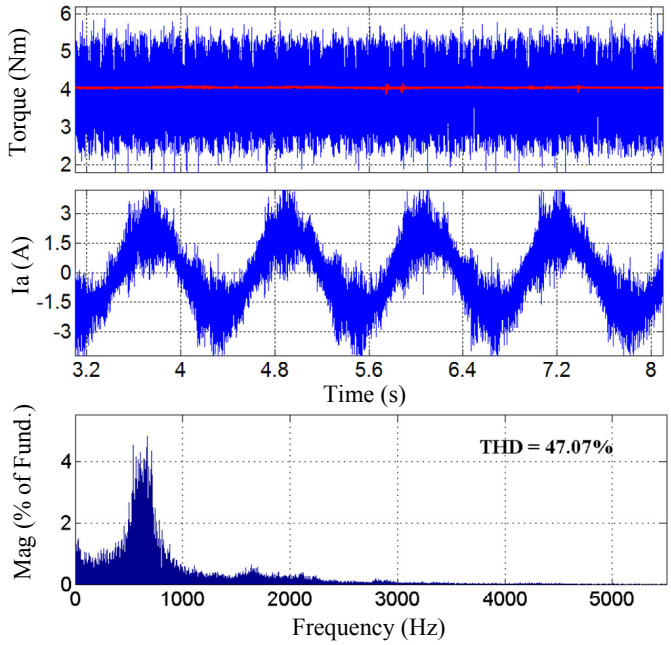

Figure 6.11: Steady state responses of the CMLI-DTC at 25 rpm, 4 Nm with torque response (top), stator current (middle) and harmonic spectrum of the stator current (bottom).

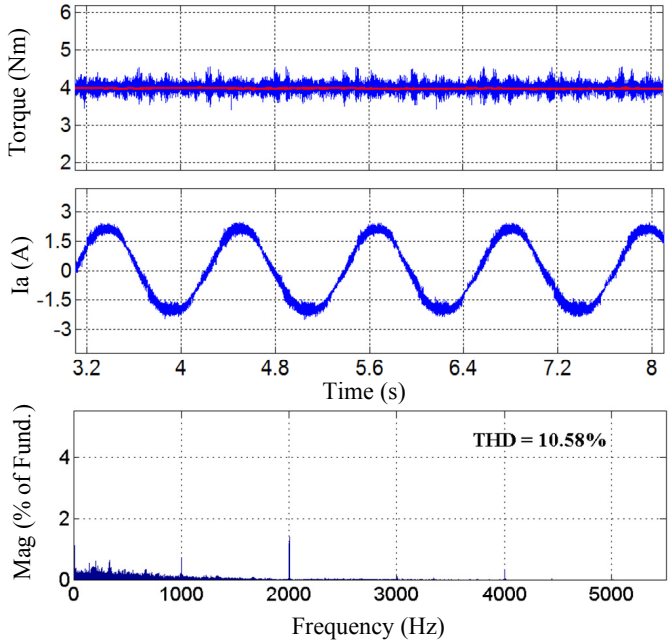

Figure 6.12: Steady state responses of the proposed MLI-DTC at 25 rpm, 4 Nm with torque response (top), stator current (middle) and harmonic spectrum of the stator current (bottom).

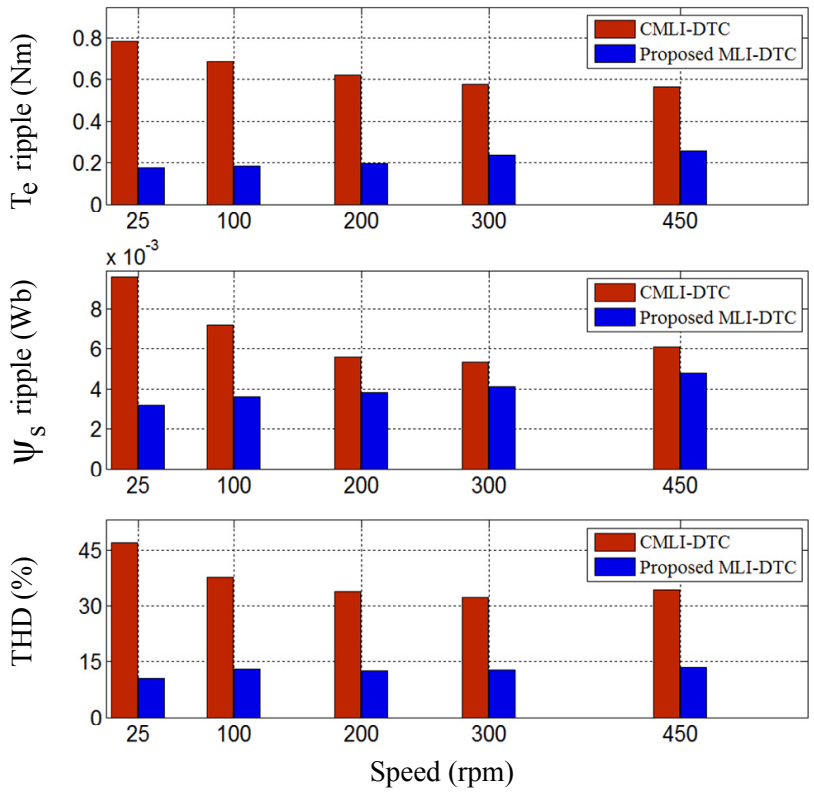

Figure 6.13: Comparison of steady state torque ripple, flux ripple and the stator current THD at different operating speeds with a load torque of 4 Nm.

higher, with the worst conditions occurring during lower speeds. The frequency spectra of the stator currents are also shown in Fig. 6.7-6.12. The switching harmonics observed at the frequency of triangular carrier demonstrate the constant switching frequency operation of the proposed MLI-DTC.

6.5.3 Parametric robustness of the proposed MLI-DTC

As the design guidelines used for the torque regulator in the proposed MLI-DTC and the proposed 3L-DTC in Chapter 5 are identical, the fundamentals discussed for examining the parametric robustness in Section 5.3 is valid for the proposed MLI-DTC. Accordingly, detuned controller gains are introduced in experiments to emulate the possible variations in R_s and L_q.

Fig. 6.14(a) shows the transient torque response during torque reversal experiment when the controller gains are detuned for a 50% increase in R_s. A small

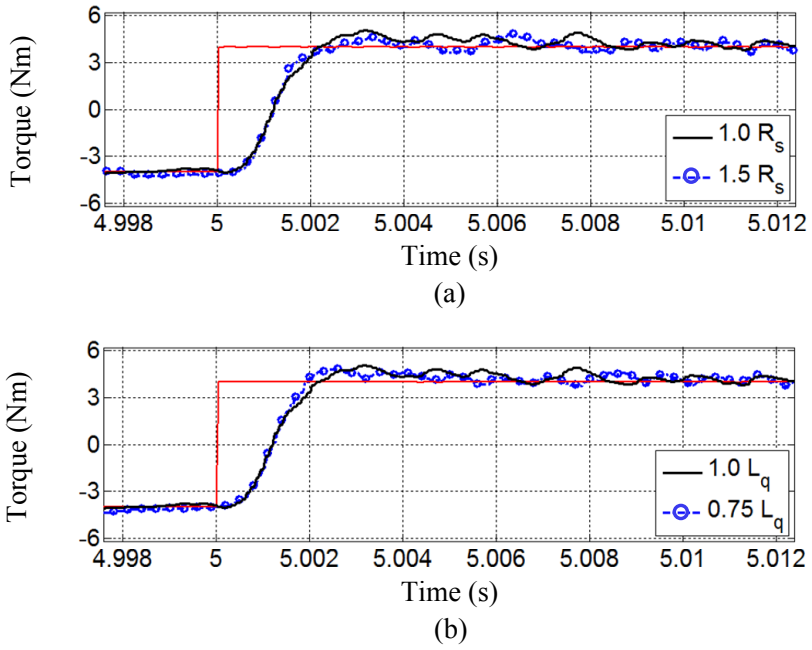

Figure 6.14: Torque dynamics with detuning of machine parameters. (a) Transient response with 50% detuning of stator resistance R_s. b) Transient response with 25% detuning of quadrature axis inductance L_q.

improvement in $\%OS$ and T_{st} is noted in Fig. 6.14(a), which is expected since the natural frequency is usually designed to be large (see (5.22)).

When controller gains are detuned for a negative variation in quadrature inductance L_q, both natural frequency and the damping ratio are increased according to (5.24)-(5.25). Consequently, faster torque dynamics with smaller $OS\%$ and T_{st} can be observed in Fig. 6.14(b) when a 25% detuning of L_q is introduced in the designed controller gains.

Additionally, negligible differences in steady state torque responses are observed in Fig. 6.14 for the variations introduced. The analyses in this subsection prove that substantial variations in machine parameters will have very small impact on the performance of the proposed MLI-DTC drive. Therefore, it can be concluded that the proposed algorithm is parametrically robust.

6.6 Conclusion

A new generalized constant switching DTC strategy for multilevel inverter fed IPMSMs drives is presented in this chapter. The proposed algorithm is simple and it is readily applicable to MLI-DTC drives incorporating generic n-level inverters. Vector decomposition technique is adopted in the proposed method so that the voltage vectors can be selected based on the principles of standard two-level inverter fed DTC drive.

The main reason for variable switching frequency in DTC drives is the use of fixed hysteresis band torque control and therefore, torque hysteresis controller is not used in the proposed method. Instead, a torque regulator that varies the duty ratio of the voltage vectors according to the torque demand is used. Consequently, as two voltage vectors are applied within each switching cycle, a constant inverter switching frequency is imposed. Furthermore, ripples of torque and flux are reduced as the stator voltage vector is tightly regulated.

A comparative experimental study against an existing generic MLI-DTC algorithm in the literature is carried out to scrutinize the transient and steady state performances of the proposed method. Results confirm the superiority of the proposed method in reducing torque and flux ripples and the THD in the output current. The other main advantage of the proposed method over prior arts is its parametric robustness and this is verified by experimental analysis.

Chapter 7

Conclusions and Future Work

7.1 Conclusions

When compared to 2L-DTC drives, MLI-DTC drives, with its increased degree of freedom, have the potential to significantly improve the torque and flux dynamics in AC motor drives. Nonetheless, the need of low inverter switching frequencies while maintaining the use of DTC in its classical form means that many of the inherent drawbacks observed in conventional 2L-DTC drives are often transferred to MLI-DTC drives.

Numerous advanced DTC algorithms have been reported in the literature to improve the performance of MLI-DTC drives. Nevertheless, performance improvements are often achieved through the use of complicated and machine parameter dependent MLI-DTC solutions that erode the intrinsic simplicity and robustness of the conventional DTC.

In order to resolve these difficulties in MLI-DTC drives, a number of MLI-DTC algorithms are developed for IPMSM in this thesis. Three of the proposed MLI-DTC algorithms focus on the performance improvements in the DTC of an IPMSM powered by a 3L-NPC inverter, which is the most commonly used MLI in high performance AC drives.

In Chapter 3, a novel DDTC that applies up to two voltage vectors in each sampling cycle is presented for a 3L-NPC inverter fed IPMSM drive. The proposed 3L-DTC algorithm uses conventional hysteresis control based switching lookup table

for both torque and flux regulation, considering the inherent switching constraints of a three-level inverter. Nonetheless, all voltage vectors in a 3L-NPC inverter are used to exploit the degree of freedom afforded by the three-level inverter.

Subsequently, a new duty ratio calculation method is developed based on the instantaneous torque error and the nature of varying torque slope in the IPMSM. Unlike the existing DDTC solutions for 3L-DTC drives in the literature, the proposed duty ratio calculation method does not rely on the accuracy of machine parameters for the optimal application of voltage vectors.

Experimental comparative studies are carried out against classical 3L-DTC and an existing duty cycle based 3L-DTC method [90] (termed as DDTC-1 in this thesis) that also uses two vectors in one switching cycle. Results presented in Chapter 3 verify that the proposed 3L-DTC method attains significantly superior performance compared to classical 3L-DTC, albeit at the cost of a marginal increment in implementation difficulty and switching frequency. When compared to DDTC-1, which is parameter dependent, the proposed method attains a similar degree of reduction in torque ripples with slightly improved low speed performances due to the use of mostly SVVs in the proposed 3L-DTC drive. At the same time, the overall regulation of flux and the THD seen in the output current are noticeably superior in the proposed 3L-DTC method.

To maximize the torque ripple reduction through DDTC algorithms, zero voltage vectors which have negative torque slopes even at very low speeds, should be used as passive vectors. However, the use of ZVVs in two-vector based DDTC solutions including the proposed 3L-DTC method in Chapter 3, is limited due to inverter inherent switching constraints.

Therefore, an improvement to the two-vector based 3L-DTC method in Chapter 3 is proposed in Chapter 4. The new DDTC method introduced in Chapter 4 presents the possibility of using ZVVs at all operating speeds by using up to three voltage vectors within each switching period. Clearly, the application of more than two voltage vectors in one switching cycle complicates the voltage vector selection

and the calculation of duty cycle. As evidenced in the literature, even the use of analytical, machine parameter dependent methods to determine appropriate duty ratios in three vector based DDTC algorithms for 3L-DTC has been proved to be tedious and complicated [88].

To overcome this problem, a simplified method that regulates the duty ratio of the non-zero passive vector according to the operating speed of the motor is developed. Subsequently, the simple TR-RMSM method used commonly for DDTC methods in 2L-DTC drives can be applied to the proposed three-vector based 3L-DTC algorithm. Comparative analysis against an existing DDTC method [91] (termed as DDTC-2 in this thesis) which also applies more than two voltage vectors in one switching cycle, show that the proposed method achieves marginal improvement in torque ripple reduction during normal to high speeds. Nonetheless, the THD of output current in the proposed 3L-DTC drive is significantly lower than DDTC-2 at all operating speeds. At low speeds, the proposed method exhibits the noticeably improved torque and flux regulation than DDTC-2.

Flux drooping problem, which commonly occurs in 3L-DTC drives during low speeds, is also mitigated by the proposed 3L-DTC method in Chapter 4. The droop in flux occurs near the sector transition regions in 3L-DTC drives mainly because of the use of six SVVs during low speeds. In the proposed DDTC method six additional voltage vectors are synthesized on the inner hexagon of the inverters voltage vector space from the existing SVVs to minimize the droop in flux. Experimental results at 3% of the rated speed verify the effectiveness of the proposed method in reducing the droop in flux.

Understandably, the implementation difficulty and the average switching frequencies in the proposed three vector based DDTC method are higher than the proposed two-vector based DDTC method. Nevertheless, it is easily implementable in a DSP controller as discussed in Chapter 4 and operates at an average switching frequency that is much lower than 2 kHz.

Although the regulation of torque and flux in 3L-DTC drives are improved through the use of DDTC methods, the inverter switching frequencies remains variable. For some applications, a constant inverter switching frequency is highly desirable and therefore, a constant switching frequency based 3L-DTC algorithm is proposed in Chapter 5. Variable switching frequencies in conventional DTC is caused mainly by the regulation of torque using hysteresis control. Accordingly, the conventional hysteresis controller is replaced by a torque regulator in the proposed method. The proposed torque regulator consists of a PI controller and a number of comparators, while its output is analogous to that of a conventional hysteresis controller, except that it changes the output state once within each switching cycle. Subsequently, two voltage vectors are applied periodically in each sampling cycle, imposing constant inverter switching to regulate the stator voltage, which in turn contributes to reduce ripples in torque and flux.

Small-signal analysis is adopted to linearize the torque control loop to establish design guidelines for the proposed torque regulator. The design guidelines provided are clearly machine parameter dependent. Therefore, detailed parametric robustness analysis is carried out experimentally to examine the sensitivity of proposed torque regulator to the possible variations in machine parameters. Experimental results illustrate that the differences noted in torque responses are insignificant, confirming the excellent parametric robustness of the proposed method.

Also, the steady state and transient responses of the proposed constant switching frequency based 3L-DTC method are presented and compared against that of classical DTC and the duty cycle based method, DDTC-1. Results prove the effectiveness of the proposed method in improving the torque and flux regulation while operating within inverter switching constraints at low and constant switching frequency.

The general performances of the three 3L-DTC algorithms proposed in this thesis are summarized in Table 7.1. The basic features of DTC are used as evaluation criteria and a grade or description is given to each of these criteria on the

Table 7.1: Comparison of the proposed 3L-DTC algorithms

	Classical 3L-DTC	2-Vector based 3L-DTC	3-Vector based 3L-DTC	CSF based 3L-DTC
Torque ripple	high	low	very low	low
Flux ripple	high	low	very low	low
Stator current THD	high	low	very low	low
Sampling frequency	high	low	low	high
Constant switching frequency	no	no	no	yes
Implementation complexity	low	moderate	high	moderate

CSF – constant switching frequency

basis of the experimental results presented in this thesis. At the same time, it is important to note that this evaluation does not convey an absolute meaning, but a relative one.

Very few of the MLI-DTC algorithms proposed in the literature are generic in nature, i.e., readily applicable to DTC drives powered by inverters with any number of output voltage levels. By using conventional torque and flux hysteresis controllers and vector decomposition techniques to enable vector selection as in 2L-DTC drives, variable inverter switching frequencies and large ripples in torque and flux are inevitable in generic MLI-DTC. Consequently, some studies have resorted to the use of parameter dependent analytical solutions to improve the performance of generic MLI-DTC drives.

The generalized MLI-DTC method proposed in Chapter 6 seeks to address this research gap. The proposed MLI-DTC algorithm has the same fundamental principles as the constant switching frequency based 3L-DTC proposed in Chapter 5. At the same time, as vector decomposition technique is adopted in the proposed MLI-DTC, the torque regulator has a much simpler structure. Two voltage vectors, selected using the same principles as in 2L-DTC, are applied in one switching cycle.

This imposes a constant inverter switching and a noticeable reduction in ripples of torque and flux as proved by the experimental results and comparative analysis against an existing generalized MLI-DTC algorithm.

In summary, this thesis has presented a number of algorithms for improving the performance of MLI fed DTC drives. Important common features among the proposed solutions are simple structure and parametric robustness which means that the proposed methods attain performance improvements without sacrificing the merit of classical DTC. Experimental results and comparative analysis against prior arts are presented to verify the effectiveness of the proposed MLI-DTC solutions.

7.2 Future Work

A number of recommendations that are suitable for future research are made in this section to improve on the work presented in this thesis.

- The constant switching frequency based MLI-DTC proposed in Chapter 6 uses a vector decomposition technique to simplify the vector selection process. Subsequently, one sub-hexagon is active during each sampling period and voltage vectors are selected according to 2L-DTC principles; i.e., a sector division of 60° and two-level torque ($\epsilon_T = \pm 1$) and flux ($\epsilon_\psi = \pm 1$) hysteresis control based switching logic are used (see Fig 6.1). The disadvantage of this vector decomposition technique is that only one sub-hexagon is active at any one time and switching transitions are limited to be between the adjacent six vectors using the switching principles of 2L-DTC.

  Conversely, if a vector decomposition technique based on four-level torque ($\epsilon_T = \pm 2, \pm 1$) control, similar to the switching logic in Table 3.1 is used, then the six sub-hexagons that are adjacent to the active sub-hexagons become active as well. In other words, seven sub-hexagons will be active at one time and the active space will resemble the voltage vector space of a three-level

inverter. Consequently, as more voltage vectors are available for selection, a sector division of 30° can be used. At the same time, the torque regulator proposed in Chapter 4 should be used to accommodate the increased degree of freedom. Subsequently, better control of torque and flux with faster transient response than the proposed MLI-DTC in Chapter 6 can be expected. The significance of using four-level torque control would increase noticeably with the number of voltage levels in a MLI.

- Using similar vector decomposition techniques discussed in this thesis for constant switching frequency based 3L-DTC methods, the DDTC algorithms proposed in Chapters 3 and 4 can also be adapted for application in MLI-DTC drives. At the same time, attention should be paid to ensure that inverter inherent switching constraints are adhered to.

- When compared to a two-level inverter, the obvious drawback of using the 3L-NPC inverter for motor drives is the usage of more semiconductor switches and the need for additional gate drive circuitry. This is especially true for low voltage motor drives, where overall system complexity and cost are often important factors. In order to improve the torque and flux responses of a low voltage 3L-DTC drive using the minimum amount of semiconductor switches, a sparse three-level inverter (S3LI) [106] can be used with the MLI-DTC algorithms proposed in this thesis. Although the number of semiconductor switches is reduced with S3LI, all voltage vectors of a conventional three-level neutral point clamped inverter can be made available for selection using the methodology discussed in [106]. Subsequently, the proposed MLI-DTC solutions can be implemented with marginal increment in implementation difficulty, owing to the synthesization of MVVs in the S3LI.

- All the work presented in thesis has focused on the constant torque region of the IPMSM. Therefore, the proposed MLI-DTC algorithms should be extended to field weakening operations. In particular, the proposed constant

switching frequency based algorithms are interesting prospects for the control of IPMSMs in the full operating range.

- The efficiency of the proposed 3L-DTC methods has been verified by comparative analysis against various state-of-the-art DDTC algorithms using the same experimental setup and conditions. Nonetheless, the veracity of the proposed 3L-DTC algorithms should be further investigated using other IPMSMs for the following reasons: 1) the rated power of the laboratory prototype IPMSM drive used for experiments in this thesis is low, with a dc-link voltage of 150V; 2) The inductances of the IPMSM used experiments are rather high. High motor inductances, when combined with low dc-link voltage, will lead to low $\frac{di}{dt}$ and less ripple content in the motor drive. Therefore, it is recommended that proposed algorithms should be tested using higher rated IPMSMs to verify the efficacy of the proposed algorithms under much harsher conditions; for instance, with high $\frac{di}{dt}$ in the IPMSM drive.

- Though the proposed MLI-DTC algorithms have been developed based on theoretical background of PMSM model and characteristics, these algorithms can be easily adapted to other AC machines such as induction motors and synchronous reluctance motors.

Appendix A

Parameters of the Test IPMSM

Table A.1: Parameters of the test IPMSM

Rated power	P_n	0.8 kW
Rated speed	ω_{rated}	1500 rpm
Number of pole pairs	P	2
Stator resistance	R_s	4.7 Ω
d-axis inductance	L_d	23.5 mH
q-axis Inductance	L_q	32.5 mH
Permanent magnet flux	ψ_f	0.667 Wb
Nominal dc-link voltage	V_{dc}	150 V
Rated speed (nom. voltage)	ω_n	500 rpm
Rated torque	$T_{e,n}$	5 Nm

Appendix B

List of Publications

Journals:

1. D. Mohan, X. Zhang, and G. H. B. Foo, "Three-level inverter-fed direct torque control of IPMSM with torque and capacitor voltage ripple reduction," *IEEE Trans. Energy Conv.*, vol. 31, no. 4, pp. 1559-1569, Dec. 2016.

2. D. Mohan, X. Zhang, and G. H. B. Foo, "A simple duty cycle control strategy to reduce torque ripples and improve low speed performance of a three level inverter fed DTC IPMSM drive," *IEEE Trans. Ind. Electron.*, vol. 64, no. 4, pp. 2709-2721, April 2017.

3. D. Mohan, X. Zhang, and G. H. B. Foo, "Three-level inverter-fed direct torque control of IPMSM with constant switching frequency and torque ripple reduction," *IEEE Trans. Ind. Electron.*, vol. 63, no. 12, pp. 7908-7918, Dec. 2016.

4. D. Mohan, X. Zhang, and G. H. B. Foo, "Generalized DTC strategy for multilevel inverter fed IPMSMs with constant inverter switching frequency and reduced torque ripples," *IEEE Trans. Energy Conv.*, vol. 32, no. 3, pp. 1031-1041, Sep. 2017.

Conferences:

1. D. Mohan, X. Zhang, and G. Foo, "Direct torque control of IPMSM driven by a three level NPC inverter with torque and capacitor voltage ripple reduction," in *Proc. IEEE Applied Power Electronics Conference and Exposition, APEC 2015*, pp. 557-564.

Bibliography

[1] M. P. Kazmierkowski, L. G. Franquelo, J. Rodriguez, M. A. Perez, and J. I. Leon, "High-performance motor drives," *IEEE Ind. Electron. Magazine*, vol. 5, no. 3, pp. 6–26, Sep. 2011.

[2] B. K. Bose, *Power Electronics and Motor Drives: Advances and Trends*. Amsterdam: Elsevier/Academic Press, 2006.

[3] N. Mohan, *Advanced electric drives analysis, control, and modeling using MATLAB/Simulink*. Hoboken, New Jersey: Wiley, 2014.

[4] J. L. Kirtley, A. Banerjee, and S. Englebretson, "Motors for ship propulsion," *Proceedings of the IEEE*, vol. 103, no. 12, pp. 2320–2332, Dec. 2015.

[5] IEE, *IEE Eighth Residential Course on Electric Traction Systems*, ser. IEE power and energy series. The Manchester conference centre, UK: Institution of Electrical Engineers, Oct. 2004.

[6] M. H. Rashid, *Power electronics handbook*, ser. Academic Press series in engineering. San Diego: Academic Press, 2001.

[7] J. Puranen, "Induction motor versus permanent magnet synchronous motor in motion control applications a comparative study," Thesis for the degree of Doctor of Science, Lappeenranta teknillinen yliopisto / Lappeenranta University of Technology, 2006.

[8] D. G. Dorrell, A. M. Knight, L. Evans, and M. Popescu, "Analysis and design techniques applied to hybrid vehicle drive machines - assessment of

alternative IPM and induction motor topologies," *IEEE Trans. Ind. Electron.*, vol. 59, no. 10, pp. 3690–3699, Oct. 2012.

[9] D. G. Dorrell, "Are wound-rotor synchronous motors suitable for use in high efficiency torque-dense automotive drives?" in *Proc. Ind. Electron. Conference, IECON 2012*, pp. 4880–4885.

[10] M. Meyer, T. Grote, and J. Bocker, "Direct torque control for interior permanent magnet synchronous motors with respect to optimal efficiency," in *Proc. European Conference on Power Electronics and Applications 2007*, Sept. 2007, pp. 1–9.

[11] T. M. Jahns, G. B. Kliman, and T. W. Neumann, "Interior permanent-magnet synchronous motors for adjustable-speed drives," *IEEE Trans. Ind. Appl.*, vol. IA-22, no. 4, pp. 738–747, Jul. 1986.

[12] R. Krishnan, *Permanent Magnet Synchronous and Brushless DC Motor Drives*. Amsterdam: CRC Press, 2009.

[13] B. Stumberger, A. Hamler, M. Trlep, and M. Jesenik, "Analysis of interior permanent magnet synchronous motor designed for flux weakening operation," *IEEE Trans. Magnetics.*, vol. 37, no. 5, pp. 3644–3647, Sep. 2001.

[14] T. M. Jahns, "Flux-weakening regime operation of an interior permanent-magnet synchronous motor drive," *IEEE Trans. Ind. Appl.*, vol. IA-23, no. 4, pp. 681–689, Jul. 1987.

[15] S. R. Macminn and T. M. Jahns, "Control techniques for improved high-speed performance of interior PM synchronous motor drives," *IEEE Transactions on Industry Applications*, vol. 27, no. 5, pp. 997–1004, Sep/Oct. 1991.

[16] D. Casadei, F. Profumo, G. Serra, and A. Tani, "FOC and DTC: two viable schemes for induction motors torque control," *IEEE Trans. Power Electron.*, vol. 17, no. 5, pp. 779–787, Sep. 2002.

[17] L. Zhong, "High performance torque and field weakening controllers for interior permenant magnet synchronous motors," Ph.D Thesis, University of New South Wales, Australia, 1999.

[18] M. Depenbrock, "Direct self-control (DSC) of inverter-fed induction machine," *IEEE Trans. Power Electron.*, vol. 3, no. 4, pp. 420–429, Oct. 1988.

[19] I. Takahashi and T. Noguchi, "A new quick-response and high-efficiency control strategy of an induction motor," *IEEE Trans. Ind. Appl.*, vol. IA-22, no. 5, pp. 820–827, Sep. 1986.

[20] I. Takahashi and Y. Ohmori, "High-performance direct torque control of an induction motor," *IEEE Trans. Ind. Appl.*, vol. 25, no. 2, pp. 257–264, Mar/Apr. 1989.

[21] E. Jaaskelainen and P. Pohjalainen, "DTC - A motor control technique for all seasons," White Paper, Apr. 2015. [Online]. Available: http://info.drivesapplications.fi/dtc-white-paper.html

[22] L. Zhong, M. F. Rahman, W. Y. Hu, K. W. Lim, and M. A. Rahman, "A direct torque controller for permanent magnet synchronous motor drives," *IEEE Trans. Energy Conv.*, vol. 14, no. 3, pp. 637–642, Sep. 1999.

[23] M. F. Rahman, L. Zhong, and K. W. Lim, "A direct torque-controlled interior permanent magnet synchronous motor drive incorporating field weakening," *IEEE Trans. Ind. Appl.*, vol. 34, no. 6, pp. 1246–1253, Nov. 1998.

[24] S. Kouro, M. Malinowski, K. Gopakumar, J. Pou, L. G. Franquelo, B. Wu, J. Rodriguez, M. A. Perez, and J. I. Leon, "Recent advances and industrial applications of multilevel converters," *IEEE Trans. Ind. Electron.*, vol. 57, no. 8, pp. 2553–2580, Aug. 2010.

[25] L. Jih-Sheng and P. Fang Zheng, "Multilevel converters-a new breed of power converters," *IEEE Trans. Ind. Appl.*, vol. 32, no. 3, pp. 509–517, May/Jun. 1996.

[26] L. M. Tolbert, P. Fang Zheng, and T. G. Habetler, "Multilevel converters for large electric drives," *IEEE Trans. Ind. Appl.*, vol. 35, no. 1, pp. 36–44, Jan/Feb. 1999.

[27] J. Rodriguez, L. Jih-Sheng, and P. Fang Zheng, "Multilevel inverters: a survey of topologies, controls, and applications," *IEEE Trans. Ind. Electron.*, vol. 49, no. 4, pp. 724–738, Aug. 2002.

[28] J. Rodriguez, S. Bernet, B. Wu, J. O. Pontt, and S. Kouro, "Multilevel voltage-source-converter topologies for industrial medium-voltage drives," *IEEE Trans. Ind. Electron.*, vol. 54, no. 6, pp. 2930–2945, Dec. 2007.

[29] L. G. Franquelo, J. Rodriguez, J. I. Leon, S. Kouro, R. Portillo, and M. A. M. Prats, "The age of multilevel converters arrives," *IEEE Ind. Electron. Magazine*, vol. 2, no. 2, pp. 28–39, Jun. 2008.

[30] F. Z. Peng, W. Qian, and D. Cao, "Recent advances in multilevel converter/inverter topologies and applications," in *Proc. Power Electronics Conference, IPEC 2010*, pp. 492–501.

[31] A. Nabae, I. Takahashi, and H. Akagi, "A new neutral-point-clamped PWM inverter," *IEEE Trans. Ind. Appl.*, vol. IA-17, no. 5, pp. 518–523, Sep. 1981.

[32] T. A. Meynard and H. Foch, "Multi-level choppers for high voltage applications," *EPE Journal*, vol. 2, no. 1, pp. 45–50, 1992.

[33] P. W. Hammond, "A new approach to enhance power quality for medium voltage AC drives," *IEEE Trans. Ind. Appl.*, vol. 33, no. 1, pp. 202–208, Jan/Feb. 1997.

[34] M. F. Rahman, L. Zhong, M. E. Haque, and M. A. Rahman, "A direct torque-controlled interior permanent-magnet synchronous motor drive without a speed sensor," *IEEE Trans. Energy Conv.*, vol. 18, no. 1, pp. 17–22, Mar. 2003.

[35] Y. Inoue, S. Morimoto, and M. Sanada, "Control method suitable for direct-torque-control-based motor drive system satisfying voltage and current limitations," *IEEE Trans. Ind. Appl.*, vol. 48, no. 3, pp. 970–976, May/Jun. 2012.

[36] J. W. Kang and S. K. Sul, "Analysis and prediction of inverter switching frequency in direct torque control of induction machine based on hysteresis bands and machine parameters," *IEEE Trans. Ind. Electron.*, vol. 48, no. 3, pp. 545–553, Jun. 2001.

[37] D. Casadei, G. Grandi, G. Serra, and A. Tani, "Effects of flux and torque hysteresis band amplitude in direct torque control of induction machines," in *Proc. Ind. Electron., Control and Instrumentation Conference, IECON 1994*, vol. 1, pp. 299–304.

[38] L. Tang, L. Zhong, M. F. Rahman, and Y. Hu, "A novel direct torque control for interior permanent-magnet synchronous machine drive with low ripple in torque and flux-a speed-sensorless approach," *IEEE Trans. Ind. Appl.*, vol. 39, no. 6, pp. 1748–1756, Nov/Dec. 2003.

[39] L. Zhong, M. F. Rahman, W. Y. Hu, and K. W. Lim, "Analysis of direct torque control in permanent magnet synchronous motor drives," *IEEE Trans. Power Electron.*, vol. 12, no. 3, pp. 528–536, May. 1997.

[40] Y. Zhang and J. Zhu, "A novel duty cycle control strategy to reduce both torque and flux ripples for dtc of permanent magnet synchronous motor drives with switching frequency reduction," *IEEE Trans. Power Electron.*, vol. 26, no. 10, pp. 3055–3067, Oct. 2011.

[41] M. P. Kazmierkowski and A. B. Kasprowicz, "Improved direct torque and flux vector control of PWM inverter-fed induction motor drives," *IEEE Trans. Ind. Electron.*, vol. 42, no. 4, pp. 344–350, Aug. 1995.

[42] V. Ambrozic, G. S. Buja, and R. Menis, "Band-constrained technique for direct torque control of induction motor," *IEEE Trans. Ind. Electron.*, vol. 51, no. 4, pp. 776–784, Aug. 2004.

[43] M. P. Kazmierkowski, R. Krishnan, and F. Blaabjerg, *Control in Power Electronics: Selected Problems.* San Diego, California, USA: Elsevier/Academic Press, 2002.

[44] L. Yen-Shin and C. Jian-Ho, "A new approach to direct torque control of induction motor drives for constant inverter switching frequency and torque ripple reduction," *IEEE Trans. Energy Conv.*, vol. 16, no. 3, pp. 220–227, Sep. 2001.

[45] I. Boldea, M. C. Paicu, G. D. Andreescu, and F. Blaabjerg, "Active flux DTFC-SVM sensorless control of IPMSM," *IEEE Trans. Energy Conv.*, vol. 24, no. 2, pp. 314–322, Jun. 2009.

[46] M. C. Paicu, I. Boldea, G. D. Andreescu, and F. Blaabjerg, "Very low speed performance of active flux based sensorless control: interior permanent magnet synchronous motor vector control versus direct torque and flux control," *IET Electric Power Appl.*, vol. 3, no. 6, pp. 551–561, Nov. 2009.

[47] G. Foo and M. F. Rahman, "Sensorless direct torque and flux-controlled IPM synchronous motor drive at very low speed without signal injection," *IEEE Trans. Ind. Electron.*, vol. 57, no. 1, pp. 395–403, Jan. 2010.

[48] C. Lascu and A. M. Trzynadlowski, "Combining the principles of sliding mode, direct torque control, and space-vector modulation in a high-

performance sensorless AC drive," *IEEE Trans. Ind. Appl.*, vol. 40, no. 1, pp. 170–177, Jan/Feb. 2004.

[49] K. Jezernik, J. Korelic, and R. Horvat, "PMSM sliding mode FPGA-based control for torque ripple reduction," *IEEE Trans. Power Electron.*, vol. 28, no. 7, pp. 3549–3556, Jul. 2013.

[50] T. Lixin, Z. Limin, M. F. Rahman, and Y. Hu, "A novel direct torque controlled interior permanent magnet synchronous machine drive with low ripple in flux and torque and fixed switching frequency," *IEEE Trans. Power Electron.*, vol. 19, no. 2, pp. 346–354, Mar. 2004.

[51] T. G. Habetler, F. Profumo, M. Pastorelli, and L. M. Tolbert, "Direct torque control of induction machines using space vector modulation," *IEEE Trans. Ind. Appl.*, vol. 28, no. 5, pp. 1045–1053, Sep/Oct. 1992.

[52] B. H. Kenny and R. D. Lorenz, "Stator- and rotor-flux-based deadbeat direct torque control of induction machines," *IEEE Trans. Ind. Appl.*, vol. 39, no. 4, pp. 1093–1101, Jul/Aug. 2003.

[53] J. S. Lee, C. H. Choi, J. K. Seok, and R. D. Lorenz, "Deadbeat-direct torque and flux control of interior permanent magnet synchronous machines with discrete time stator current and stator flux linkage observer," *IEEE Trans. Ind. Appl.*, vol. 47, no. 4, pp. 1749–1758, Jul/Aug. 2011.

[54] D. Casadei, G. Serra, and K. Tani, "Implementation of a direct control algorithm for induction motors based on discrete space vector modulation," *IEEE Trans. Power Electron.*, vol. 15, no. 4, pp. 769–777, Jul. 2000.

[55] D. Casadei, G. Serra, A. Tani, and L. Zarri, "Direct torque control for induction machines: A technology status review," in *Proc. Electrical Machines Design Control and Diagnosis Workshop, WEMDCD 2013*, Mar. 2013, pp. 117–129.

[56] P. Cortes, M. P. Kazmierkowski, R. M. Kennel, D. E. Quevedo, and J. Rodriguez, "Predictive control in power electronics and drives," *IEEE Trans. Ind. Electron.*, vol. 55, no. 12, pp. 4312–4324, Dec. 2008.

[57] M. Pacas and J. Weber, "Predictive direct torque control for the PM synchronous machine," *IEEE Trans. Ind. Electron.*, vol. 52, no. 5, pp. 1350–1356, Oct. 2005.

[58] P. Karamanakos, T. Geyer, N. Oikonomou, F. D. Kieferndorf, and S. Manias, "Direct model predictive control: A review of strategies that achieve long prediction intervals for power electronics," *IEEE Ind. Electron. Magazine*, vol. 8, no. 1, pp. 32–43, Mar. 2014.

[59] S. Vazquez, J. Rodriguez, M. Rivera, L. G. Franquelo, and M. Norambuena, "Model predictive control for power converters and drives: Advances and trends," *IEEE Trans. Ind. Electron.*, Early access article, 2016.

[60] P. Correa, M. Pacas, and J. Rodriguez, "Predictive torque control for inverter-fed induction machines," *IEEE Trans. Ind. Electron.*, vol. 54, no. 2, pp. 1073–1079, Apr. 2007.

[61] R. Morales-Caporal and M. Pacas, "Encoderless predictive direct torque control for synchronous reluctance machines at very low and zero speed," *IEEE Trans. Ind. Electron.*, vol. 55, no. 12, pp. 4408–4416, Dec. 2008.

[62] H. Miranda, P. Cortes, J. I. Yuz, and J. Rodriguez, "Predictive torque control of induction machines based on state-space models," *IEEE Trans. Ind. Electron.*, vol. 56, no. 6, pp. 1916–1924, Jun. 2009.

[63] T. Geyer, G. Papafotiou, and M. Morari, "Model predictive direct torque control, part I: Concept, algorithm, and analysis," *IEEE Trans. Ind. Electron.*, vol. 56, no. 6, pp. 1894–1905, Jun. 2009.

[64] G. Papafotiou, J. Kley, K. G. Papadopoulos, P. Bohren, and M. Morari, "Model predictive direct torque control, part II: Implementation and experimental evaluation," *IEEE Trans. Ind. Electron.*, vol. 56, no. 6, pp. 1906–1915, Jun. 2009.

[65] J. Beerten, J. Verveckken, and J. Driesen, "Predictive direct torque control for flux and torque ripple reduction," *IEEE Trans. Ind. Electron.*, vol. 57, no. 1, pp. 404–412, Jan. 2010.

[66] Y. Zhang and H. Yang, "Model predictive torque control of induction motor drives with optimal duty cycle control," *IEEE Trans. Power Electron.*, vol. 29, no. 12, pp. 6593–6603, Dec. 2014.

[67] ——, "Generalized two-vector-based model-predictive torque control of induction motor drives," *IEEE Trans. Power Electron.*, vol. 30, no. 7, pp. 3818–3829, Jul. 2015.

[68] M. H. Vafaie, B. M. Dehkordi, P. Moallem, and A. Kiyoumarsi, "A new predictive direct torque control method for improving both steady-state and transient-state operations of the PMSM," *IEEE Trans. Power Electron.*, vol. 31, no. 5, pp. 3738–3753, May. 2016.

[69] ——, "Minimizing torque and flux ripples and improving dynamic response of PMSM using a voltage vector with optimal parameters," *IEEE Trans. Ind. Electron.*, vol. 63, no. 6, pp. 3876–3888, Jun. 2016.

[70] J. Rodriguez, M. P. Kazmierkowski, J. R. Espinoza, P. Zanchetta, H. Abu-Rub, H. A. Young, and C. A. Rojas, "State of the art of finite control set model predictive control in power electronics," *IEEE Trans. Ind. Infor.*, vol. 9, no. 2, pp. 1003–1016, May. 2013.

[71] A. Mora, A. Orellana, J. Juliet, and C. R, "Model predictive torque control for torque ripple compensation in variable-speed PMSMs," *IEEE Trans. Ind. Electron.*, vol. 63, no. 7, pp. 4584–4592, Jul. 2016.

[72] M. Habibullah, D. D. C. Lu, D. Xiao, and M. F. Rahman, "A simplified finite-state predictive direct torque control for induction motor drive," *IEEE Trans. Ind. Electron.*, vol. 63, no. 6, pp. 3964–3975, Jun. 2016.

[73] P. Cortes, S. Kouro, B. L. Rocca, R. Vargas, J. Rodriguez, J. I. Leon, S. Vazquez, and L. G. Franquelo, "Guidelines for weighting factors design in model predictive control of power converters and drives," in *Proc. Industrial Technology Conference, ICIT 2009.*, pp. 1–7.

[74] S. A. Davari, D. A. Khaburi, and R. Kennel, "An improved FCS-MPC algorithm for an induction motor with an imposed optimized weighting factor," *IEEE Trans. Power Electron.*, vol. 27, no. 3, pp. 1540–1551, Mar. 2012.

[75] R. Vargas, U. Ammann, B. Hudoffsky, J. Rodriguez, and P. Wheeler, "Predictive torque control of an induction machine fed by a matrix converter with reactive input power control," *IEEE Trans. Power Electron.*, vol. 25, no. 6, pp. 1426–1438, Jun. 2010.

[76] L. Romeral, A. Arias, E. Aldabas, and M. G. Jayne, "Novel direct torque control (DTC) scheme with fuzzy adaptive torque-ripple reduction," *IEEE Trans. Ind. Electron.*, vol. 50, no. 3, pp. 487–492, Jun. 2003.

[77] E. Flach, R. Hoffmann, and P. Mutschler, "Direct mean torque control of an induction motor," in *Proc. EPE 1997*, vol. vol. 7, no. 3, pp. 672–677.

[78] K. Jun-Koo and S. Seung-Ki, "New direct torque control of induction motor for minimum torque ripple and constant switching frequency," *IEEE Trans. Ind. Appl.*, vol. 35, no. 5, pp. 1076–1082, Sep/Oct. 1999.

[79] Y. Zhang and J. Zhu, "Direct torque control of permanent magnet synchronous motor with reduced torque ripple and commutation frequency," *IEEE Trans. Power Electron.*, vol. 26, no. 1, pp. 235–248, Jan. 2011.

[80] Y. Ren, Z. Q. Zhu, and J. Liu, "Direct torque control of permanent-magnet synchronous machine drives with a simple duty ratio regulator," *IEEE Transactions on Industrial Electronics*, vol. 61, no. 10, pp. 5249–5258, 2014.

[81] F. Niu, K. Li, and Y. Wang, "Direct torque control for permanent-magnet synchronous machines based on duty ratio modulation," *IEEE Trans. Ind. Electron.*, vol. 62, no. 10, pp. 6160–6170, Oct. 2015.

[82] G. Abad, M. A. Rodriguez, and J. Poza, "Two-level VSC based predictive direct torque control of the doubly fed induction machine with reduced torque and flux ripples at low constant switching frequency," *IEEE Trans. Power Electron.*, vol. 23, no. 3, pp. 1050–1061, May. 2008.

[83] G. S. Buja and M. P. Kazmierkowski, "Direct torque control of PWM inverter-fed AC motors - a survey," *IEEE Trans. Ind. Electron.*, vol. 51, no. 4, pp. 744–757, Aug. 2004.

[84] J. Rodriguez, S. Bernet, P. K. Steimer, and I. E. Lizama, "A survey on neutral-point-clamped inverters," *IEEE Trans. Ind. Electron.*, vol. 57, no. 7, pp. 2219–2230, Jul. 2010.

[85] N. Celanovic and D. Boroyevich, "A comprehensive study of neutral-point voltage balancing problem in three-level neutral-point-clamped voltage source PWM inverters," *IEEE Trans. Power Electron.*, vol. 15, no. 2, pp. 242–249, Mar. 2000.

[86] S. Busquets-Monge, J. Bordonau, D. Boroyevich, and S. Somavilla, "The nearest three virtual space vector PWM - a modulation for the comprehen-

sive neutral-point balancing in the three-level NPC inverter," *IEEE Power Electron. Letters*, vol. 2, no. 1, pp. 11–15, Mar. 2004.

[87] Y. Zhang, J. Zhu, Z. Zhao, W. Xu, and D. G. Dorrell, "An improved direct torque control for three-level inverter-fed induction motor sensorless drive," *IEEE Trans. Power Electron.*, vol. 27, no. 3, pp. 1502–1513, Mar. 2012.

[88] M. Habibullah, D. D. C. Lu, D. Xiao, and M. F. Rahman, "Finite-state predictive torque control of induction motor supplied from a three-level NPC voltage source inverter," *IEEE Trans. Power Electron.*, vol. 32, no. 1, pp. 479–489, Jan. 2017.

[89] X. del Toro Garcia, A. Arias, M. G. Jayne, and P. A. Witting, "Direct torque control of induction motors utilizing three-level voltage source inverters," *IEEE Trans. Ind. Electron.*, vol. 55, no. 2, pp. 956–958, Feb. 2008.

[90] G. Brando, A. Dannier, A. D. Pizzo, R. Rizzo, and I. Spina, "Generalised look-up table concept for direct torque control in induction drives with multilevel inverters," *IET Elect. Power Appl.*, vol. 9, no. 8, pp. 556–567, Sep. 2015.

[91] L. Kyo-Beum, S. Joong-Ho, C. Ick, and Y. Ji-Yoon, "Torque ripple reduction in DTC of induction motor driven by three-level inverter with low switching frequency," *IEEE Trans. Power Electron.*, vol. 17, no. 2, pp. 255–264, Mar. 2002.

[92] L. Kyo-Beum, H. Sung-Hoe, Y. Ji-Yoon, and F. Blaabjerg, "Performance improvement of DTC for induction motor-fed by three-level inverter with an uncertainty observer using RBFN," *IEEE Trans. Energy Conv.*, vol. 20, no. 2, pp. 276–283, Jun. 2005.

[93] L. Kyo-Beum, S. Joong-Ho, I. Choy, and Y. Ji-Yoon, "Improvement of low-speed operation performance of DTC for three-level inverter-fed induction

motors," *IEEE Trans. Ind. Electron.*, vol. 48, no. 5, pp. 1006–1014, Oct. 2001.

[94] M. F. Escalante, J. C. Vannier, and A. Arzande, "Flying capacitor multilevel inverters and DTC motor drive applications," *IEEE Trans. Ind. Electron.*, vol. 49, no. 4, pp. 809–815, Aug. 2002.

[95] F. Khoucha, S. M. Lagoun, K. Marouani, A. Kheloui, and M. E. H. Benbouzid, "Hybrid cascaded H-bridge multilevel-inverter induction-motor-drive direct torque control for automotive applications," *IEEE Trans. Ind. Electron.*, vol. 57, no. 3, pp. 892–899, Mar. 2010.

[96] F. Khoucha, M. S. Lagoun, A. Kheloui, and M. E. H. Benbouzid, "A comparison of symmetrical and asymmetrical three-phase H-bridge multilevel inverter for DTC induction motor drives," *IEEE Trans. Energy Conv.*, vol. 26, no. 1, pp. 64–72, Mar. 2011.

[97] C. A. Martins, X. Roboam, T. A. Meynard, and A. S. Carvalho, "Switching frequency imposition and ripple reduction in DTC drives by using a multilevel converter," *IEEE Trans. Power Electron.*, vol. 17, no. 2, pp. 286–297, Mar. 2002.

[98] A. BenAbdelghani, C. A. Martins, X. Roboam, and T. A. Meynard, "Use of extra degrees of freedom in multilevel drives," *IEEE Trans. Ind. Electron.*, vol. 49, no. 5, pp. 965–977, Oct. 2002.

[99] J. Rodriguez, J. Pontt, S. Kouro, and P. Correa, "Direct torque control with imposed switching frequency in an 11-level cascaded inverter," *IEEE Trans. Ind. Electron.*, vol. 51, no. 4, pp. 827–833, Aug. 2004.

[100] S. Morimoto, K. Hatanaka, Y. Tong, Y. Takeda, and T. Hirasa, "Servo drive system and control characteristics of salient pole permanent magnet

synchronous motor," *IEEE Trans. Ind. Appl.*, vol. 29, no. 2, pp. 338–343, Mar/Apr. 1993.

[101] C. G. Mei, S. K. Panda, J. X. Xu, and K. W. Lim, "Direct torque control of induction motor-variable switching sectors," in *Proc. Power Electronics and Drive Systems Conference, PEDS 1999*, vol. 1, Jul. 1999, pp. 80–85 vol.1.

[102] I. M. Alsofyani and N. R. N. Idris, "Simple flux regulation for improving state estimation at very low and zero speed of a speed sensorless direct torque control of an induction motor," *IEEE Trans. Power Electron.*, vol. 31, no. 4, pp. 3027–3035, Apr.2016.

[103] ——, "Lookup-table-based DTC of induction machines with improved flux regulation and extended kalman filter state estimator at low-speed operation," *IEEE Trans. Ind. Infor.*, vol. 12, no. 4, pp. 1412–1425, Aug. 2016.

[104] S. Mathapati and J. Bocker, "Analytical and offline approach to select optimal hysteresis bands of DTC for PMSM," *IEEE Trans. Ind. Electron.*, vol. 60, no. 3, pp. 885–895, Mar. 2013.

[105] J.-K. Kang, D.-W. Chung, and S.-K. Sul, "Direct torque control of induction machine with variable amplitude control of flux and torque hysteresis bands," in *Proc. International conference on Electric Machines and Drives, IEMD 1999*, May. 1999, pp. 640–642.

[106] D. Mohan, X. Zhang, and G. H. B. Foo, "Direct torque control of sparse three level inverter fed low voltage IPMSM drive," in *Proc. IEEE International Electric Machines Drives Conference, IEMDC*, May. 2015, pp. 929–935.